DOT/FAA/AR-xx/xx

Federal Aviation Administration

William J. Hughes Technical Center

Aviation Research Division

Atlantic City International Airport

New Jersey 08405

The FAA's Center of Excellence for UAS Research

ASSURE

Alliance for System Safety of UAS through Research Excellence

Annex D: Task A14 UAS Ground Collision Severity Evaluation, Mississippi State University Final Report

Dr. Raj Prabhu, MSU Principal Investigator – rprabhu@abe.msstate.edu, Assistant Professor, Department of Agricultural and Biological Engineering, Mississippi State University

Date 24 May 2019

Final Report

U.S. Department of Transportation

Federal Aviation Administration

NOTICE

Legal Disclaimer: The information provided herein may include content supplied by third parties. Although the data and information contained herein has been produced or processed from sources believed to be reliable, the Federal Aviation Administration makes no warranty, expressed or implied, regarding the accuracy, adequacy, completeness, legality, reliability or usefulness of any information, conclusions or recommendations provided herein. Distribution of the information contained herein does not constitute an endorsement or warranty of the data or information provided herein by the Federal Aviation Administration or the U.S. Department of Transportation. Neither the Federal Aviation Administration nor the U.S. Department of Transportation shall be held liable for any improper or incorrect use of the information contained herein and assumes no responsibility for anyone's use of the information. The Federal Aviation Administration and U.S. Department of Transportation shall not be liable for any claim for any loss, harm, or other damages arising from access to or use of data or information, including without limitation any direct, indirect, incidental, exemplary, special or consequential damages, even if advised of the possibility of such damages. The Federal Aviation Administration shall not be liable to anyone for any decision made or action taken, or not taken, in reliance on the information contained herein.

ACKNOWLEDGEMENTS

The MSU research team would like to thank the Department of Agricultural and Biological Engineering and the Bagley College of Engineering for their support towards this project. The MSU research team would also like to thank Mr. Alex Smith, Mr. Phong Phan, Mr. Jared Hopper, Mr. Daniel Thomas, Ms. Ashma Sharma, Ms. Anna Marie Dulaney, Ms. Sonja Jensen, Mr. Parker Berthelson, Mr. Hamed Bakhtiary, Ms. Sammira Rais-Rohani, Ms. Jasmine Farrell, Mr. Martin McCandless, and Ms. Jade Cooper for carrying out various tasks associated with this project. Further, the research team is grateful to Dr. Jonathan Pote, Dr. Lakiesha Williams, Dr. Wilburn Whittington, Dr. Haitham El Kadiri, and Dr. Yucheng Liu for their contribution in this research effort. The team would also like to recognize the support and synergistic collaboration from research teams in UAH, NIAR and OSU. Lastly, we would also like to recognize Mr. Stephen Luxion and Dr. Kari Babski-Reeves for their support and guidance.

TABLE OF CONTENTS

LIST OF FIGURES

LIST OF TABLES

LIST OF ACRONYMS

3D	3-Dimensional
BrIC	Brain Injury Criterion
CT	Computer Tomography
FAA	Federal Aviation Administration
FE	Finite Element
FEM	Finite Element Method
FEA	Finite Element Analysis
HIC	Head Injury Criterion
JAA	Joint Aviation Authority
KPa	Kilo Pascals
MPa	Mega Pascals
MSU	Mississippi State University
sUAS	small Unmanned Aircraft System
UAS	Unmanned Aircraft System

EXECUTIVE SUMMARY

High biofidelic human head and neck FE models were developed by MSU to investigate sUAS impacts to the human head as part of the ASSURE Task A14 2017 Ground Collision Severity Study. CT scans of a PMHS from OSU was obtained and meshed using a FE meshing software. Initially, verification and comparison procedures were carried for the MSU human head and neck model. The simulation results for the verification and comparison process gave good correlation to experimental data. The FE meshes of the human head and neck models, along with UAS FE model, were then imported into LS-DYNA FE software to conduct sUAS-human head and neck impact simulations. Fifteen high biofidelic sUAS-human head and neck FE simulations were conducted to replicate OSU's sUAS-PMHS impact tests. Overall, the FE results had good agreement with PMHS impact test results, with the average difference in peak accelerations between MSU and OSU's values being 14%. The FE simulations showed that an increase in sUAS's velocity, and thereby, kinetic energy, resulted in an increased risk of brain injury. The experiments and FE simulations were investigating the worst case scenarios, and the FE simulations for these cases predicted different levels of brain injury when AIS3 risk of injury scale were assessed using HIC and BrIC. A few of those FE simulations also predicted a high percentage risk of brain injury on a AIS3 percentage risk of injury scale. Due to the inconsistencies in results of HIC-based AIS3 and BrIC-based AIS3 brain injury risks, further investigation is warranted to develop new brain injury criteria. Additionally, minor variations in sUAS's location of impact, orientation, and angle of impact produced considerable variations in the risk of brain injury. Hence, additional investigations are needed to understand the sensitivity and uncertainties of the sUAS impact input variables.

1 INTRODUCTION

High Biofidelic FE simulations of sUAS impacts on human head and neck models were conducted for fifteen different scenarios as part of MSU's Task C of this current project. The FE models for the human head and neck were developed from CT scans of PMHS procured from OSU as part of Task D of the current project. The human head and neck model used for FE simulations was verified and compared using experimental data from PMHS impact tests from published literature and using OSU PMHS impact tests. The FE results were then used to calculate the brain injury metrics using subroutines provided by NIAR as part of Task B. MSU's FE simulations were then compared to OSU's PMHS tests (Task D) using injury metrics that are currently accepted for quantifying brain injury in automotive industry.

2 MATERIALS AND METHODS

Multiple human head and neck models were developed from CT scans from multiple sources. The human head and neck models were iteratively assessed for anatomically accuracy and mesh stability. The final version of the human head and neck model, meshed using OSU's PMHS, was then used for conducting fifteen FE simulations that replicated impact scenarios from OSU's PMHS impact tests. The following detail the development of the human head and neck models, implementation of the human head and neck model, and sUAS model in LS-DYNA FE software, and the simulation and data post-processing methodology.

2.1 Design of Model

The overall design of the head and neck human models revolved around the process of obtaining a Computed Tomography or CT scan of a 50th percentile US male from Mississippi State University and one PMHS from Ohio State University, respectively, and then developing a realistic and accurate mesh in the Simpleware^{TM} ScanIP (Version M-2017.06, Synopsys, Inc., Mountain View, USA). This mesh was then analyzed and converted into a command script that could be administered to and executed in the finite element modeling software LS-DYNA^{TM} (LSTC, Livermore, CA). Material Properties, Surface Properties, Interaction Properties, and Surface Properties of boundary conditions were then implemented to the various aspects of the human head and neck FE mesh in LS-DYNA to generate the most accurate and anatomically realistic properties for each meshed body part or organ is the models.

FE simulations were run for the models to obtain accurate data and troubleshoot any issues that potentially arose. The key differences in the old and current model are the improvements in the quality of CT scans used to generate the meshes used in the models, and the improved pixel dimensions of the CT scans. These two improvements allowed for a more accurate an anatomically correct human head and neck model to be developed.

Coarse-grained and fine-grained meshes were developed for the human head and neck model in attempts to show convergence FE results for the said meshes. The first couple of meshes generated from the CT scans were much coarser than the current meshes due to the lack anatomical details in the older CT scans. The meshes were then compared to one another to provide the overall best quality of mesh obtainable all while providing accurate results in terms of the mechanical properties of the head model during and post impact from the sUAS collision simulation.

2.2 Human Development Summary

The human head and neck model complied with the process previously stated in that a CT scan at Mississippi State University was obtained to develop high biofidelic FE mesh using these CT scans. This mesh was then analyzed and a command script for LS-DYNA was developed to incorporate the mesh into the head and neck model and execute the simulation in LS-DYNA. After FE simulation results were analyzed it was evident that many anatomic insufficiencies were discovered in the original CT scan that was received. The CT scan's voxel dimensions had spacing in the X, Y, and Z orientation of 2 mm, which was not nearly refined enough to develop anatomically accurate FE mesh. The image dimensions were far too large as well, which furthered inaccuracies in the meshing of the CT scan. The resolution of the old CT scan and the parameters given were also inaccurate in some aspects for the thickness of the skull was far too large, for a 50th percentile US male, to accurately represent an average human head. Two 3-dimensional renditions of the old CT scans of the 50th percentile US male are shown below in Figures 1 and 2, which represent an optical standpoint of the CT scan in both the X (front view) and Y (side view) axes, respectively.

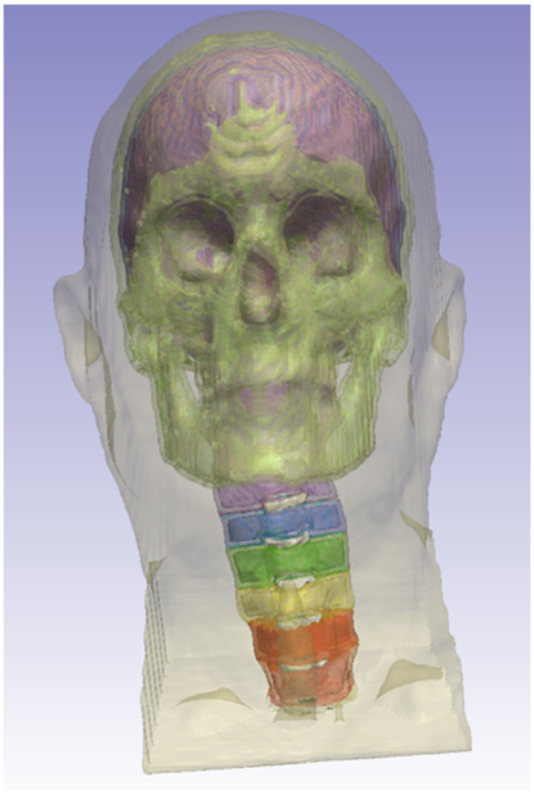

Figure 1. Front view of the 3D rendition of old CT scans from MSU

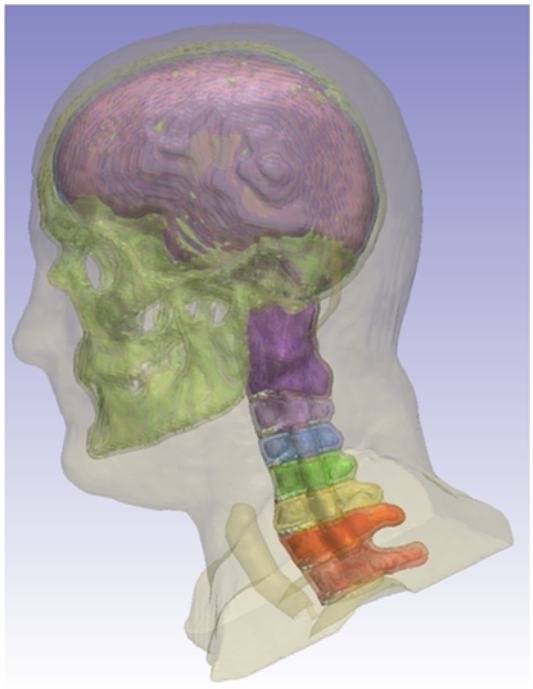

Figure 2. Side view of the 3D rendition of the old CT scan from MSU

Once the old model had been re-meshed iteratively in order to smooth the mesh and obtain stable meshes, material properties were implemented into each individual part of the mesh akin to the THUMS human head and neck model. The individual meshes were then tied to their respected corresponding meshes to assure no separation occurred as a result of the impact during the simulation process.

In order to verify the human head and neck model, Nahum et al's[1] blunt impact cadaveric Experimental No.37 was simulated with an cylinder impacting the human head and neck model. The material properties of the cylinder where given a standard elastic material for steel, and a cushion was then developed to simulate the cadaveric impact test.

Soon after simulation were conducted, it was revealed that the vertebrae anatomy of the CT scan that was used for this model were inaccurate. However, even though the model was inaccurate, the overall process for meshing and simulating the impacts for the corrected CT scan would be the same as for the old CT scan. Therefore, the old model was utilized to act as a practice method to ensure that time could be recovered once the new CT scan was received. The old model was employed and utilized to assure that knowledge of how to run the simulations and troubleshooting in LS-DYNA would be obtained beforehand in terms of once the improved CT scan was obtained.

[1] A.M. Nahum, R. Smith, C.C. Ward, Intracranial Pressure Dynamics During Head Impact, 1977 http://dx.doi.org/10.4271/770922.

2.2.1 Model Human Head and Neck Mesh

The meshing of the human head and neck model revolved around the process of taking the acquired CT scan and utilizing Simpleware™ ScanIP to develop high biofidelic meshes. The meshes were re-meshed numerous times to assure that the smoothest and most accurate meshes possible were developed to represent each individual organ and body part of the human head and neck. The individual meshes were then tied to their corresponding meshes to ensure that unrealistic disassociation did not occur. Each individual organ that was separately meshed is stated in Table 1 with their respective number of elements and number of nodes.

Table 1. A table of the mesh element and node numbers for each component of the old human head and neck FE model

Meshed Part	Number of Elements	Number of Nodes
Falx	42,517	170,068
Grey Matter	312,333	1,249,332
White Matter	514,576	2,058,304
C7 Vertebrae	52,453	209,812
C6 Vertebrae	47,453	190,856
C5 Vertebrae	41,714	190,172
C4 Vertebrae	40,846	163,384
C3 Vertebrae	40,543	162,172
C2 Vertebrae	47,472	189,888
C1 Vertebrae	47,014	188,056
Skull Spongy	718,992	2,875,968
Skull Cortical 1	1,044,068	4,176,272
Spinal Cord	25,017	100,068
CSF	346,908	147,632
Skin	1,505,782	6,023,128
Vertebral Disk	32,352	129,408
C1 Vertebrae Spongy	17,967	71,868
C2 Vertebrae Spongy	22,509	90,036
C3 Vertebrae Spongy	17,589	70356
C4 Vertebrae Spongy	16,209	64,836
C5 Vertebrae Spongy	16,095	64,380
C6 Vertebrae Spongy	13,098	52392
C7 Vertebrae Spongy	14,211	56,844

The differences in the element and node number in the two models arise from the two models originating from two different CT scans. In the first CT scan the overall quality and clarity of the scan had to be improved and this resulted in a coarser mesh that had to be smoothed and eroded a number of times in attempts generate a stable mesh. The insufficiencies in the CT scan quality would also cause various meshing problems to occur, such as various nodes protruding from the mesh that refused to be smoothed and eroded without regenerating the protruding node once the model simulation began. Images of the old coarse mesh of the human head and neck model can be seen below in Figure 3.

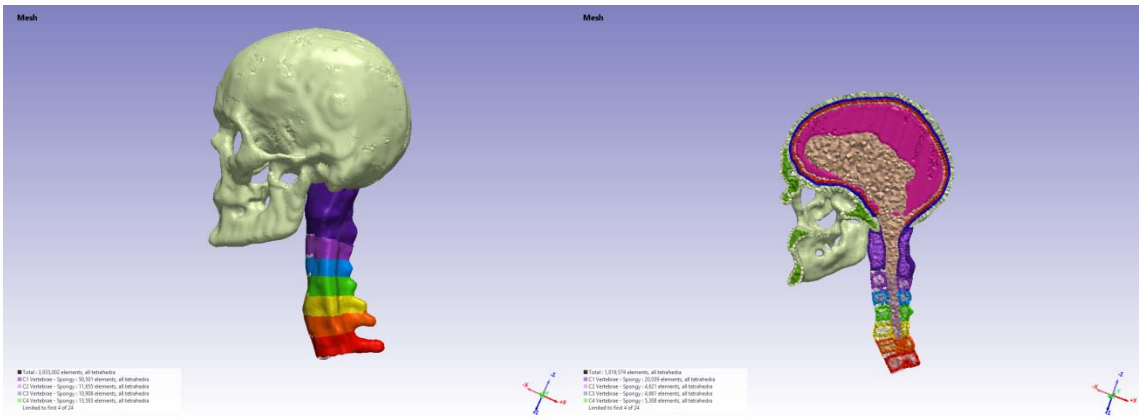

Figure 3. (a) Coarse mesh, and (b) a sagittal cut of the MSU old human and neck model

2.2.2 Human Head and Neck Model Material, Surface, and Interaction Properties

Once the meshes had been developed and smoothed to acceptable stability, material properties were given to the individual meshed component. The material properties were chosen by using criteria that strove to represent best how each individual component of the head and neck human model is composed of. The material properties were comparably based on the Total Human Model for Safety or THUMS[2] model developed by Toyota Motor Corporation, of which Mississippi State University has an active license. Essentially, the material properties for THUM model's head and neck were in the high-fidelity human head and neck model. Three main types of materials were used in the material properties that were assigned to the individual meshes. Those materials being: elastic material, plastic material, and viscoelastic material. Furthermore, two subtypes of plastic materials were also used; the Fu Chang foam material[3,4] and the damage type 2 material. Elastic material properties were given to the meshes that represented head and neck components that could deform under certain stresses and forces and re-establish to some extent their original properties. The cerebral spinal fluid was given the material property of an elastic fluid. Plastic material properties were given to meshes that needed to represent the components that gave plastic deformation due to impacts. The plastic material properties solely applied to the cortical aspect of the C1 – C7 vertebrae[3,4]. Even though bone is a known viscoelastic material, the cortical properties of the vertebrae were best represented by plastic materials, as prescribed in the THUMS human head and neck model. The subtype plastic material, Fu Chang foam, was utilized to represent the material composition of the intervertebral disk and represent the joint failure of the disk and the vertebrae. It should also be noted that the Fu Chang foam's material property of yield stress is not a yield stress but a cut off stress as

[2] Yuko Nakahira and Hideyuki Kimpara, "Development and Validation of the Total HUman Model for Safety (THUMS) Toward Further Understanding of Occupant Injury Mechanisms in Precrash and During Crash AU - Iwamoto, Masami," *Traffic Injury Prevention* 16, no. sup1 (June 1, 2015): S36–48, https://doi.org/10.1080/15389588.2015.1015000.

[3] Chang, F., Hallquist, J., Lu, D., Shahidi, B. et al., "Finite Element Analysis of Low-Density High-Hysteresis Foam Materials and the Application in the Automotive Industry," SAE Technical Paper 940908, 1994

[4] F. Chang, *The Development of a finite element human thorax model for impact injury studies*, Proceedings of the 2001 ASME International Mechanical Engineering Congress and Exposition, New York, NY, 2001, pp. 103–111.

to when the foam will fail due to negative volume issues. This element is set is place to help parameterize the intrinsic effects of the foam's material placement within the human head and neck model, as well as models of its other uses. The damage type 2 material properties were assigned to the spongy bone aspect of the vertebrae. Lastly, the viscoelastic material properties represented many of the materials that has high content of fluids such as white and grey matters of the brain and the spinal cord.

The elastic materials were defined by their density, Young's modulus, and Poisson's ratio; whereas viscoelastic materials were defined by their density, bulk modulus, shear moduli, and decay constants. The varying values set for these parameters helped define the way each mesh would react mechanically to the various forces and stresses they would be exposed to. These values were also used in coordination with the Toyota THUMS human head and neck model. Table 2 gives the various human head and neck components with their corresponding material types and parameters can be viewed below. The units of the parameters of the material properties are in ton, mm, s, N, MPa, and N-mm.

Table 2. A table of the material properties of individual components of the human head and neck model

Component /Mesh	Material Type	Density (ton/mm^3)	Young's Modulus (MPa)	Poisson's Ratio	Bulk Modulus (MPa)	Short Term Shear Modulus (MPa)	Long Term Shear Modulus (MPa)	Decay Constant	Yield Stress (MPa)
Falx	Elastic[2]	1.13×10^{-9}	31.5	0.45					
Grey Matter	Viscoelastic[2]	1×10^{-9}			2190	0.01	0.005	0.06	
White Matter	Viscoelastic[2]	1×10^{-9}			2160	0.0125	0.006125	0.06	
C7 Vert.	Plastic[2,3]	2×10^{-9}	$1.3x10^{-4}$	0.3					80
C6 Vert.	Plastic[2,3]	2×10^{-9}	$1.3x10^{-4}$	0.3					80
C5 Vert.	Plastic[2,3]	2×10^{-9}	$1.3x10^{-4}$	0.3					80
C4 Vert.	Plastic[2,3]	2×10^{-9}	$1.3x10^{-4}$	0.3					80
C3 Vert.	Plastic[2,3]	2×10^{-9}	$1.3x10^{-4}$	0.3					80
C2 Vert.	Plastic[2,3]	2×10^{-9}	$1.3x10^{-4}$	0.3					80
C1 Vert.	Plastic[2,3]	2×10^{-9}	$1.3x10^{-4}$	0.3					80
Skull Spongy	Elastic[2]	1×10^{-9}	390	0.19					
Skull Cort.	Elastic[2]	2×10^{-9}	$1x10^{-4}$	0.22					
Spinal Cord	Viscoelastic[2]	1×10^{-9}			2190	1	0.2	0.6	
CSF	Elastic Fluid[2]	1×10^{-9}	0	0					2000
Skin	Viscoelastic[2]	1.32×10^{-9}			2880	7.39	2.36	0.1	
Vert. Disk	Fu Chang Foam[3,4]	1×10^{-9}	35.7						$-9.4x10^{14}$*
C1 Spongy	Damage Type 2[2]	1×10^{-9}	40	0.45					1.8
C2 Spongy	Damage Type 2[2]	1×10^{-9}	40	0.45					1.8
C3 Spongy	Damage Type 2[2]	1×10^{-9}	40	0.45					1.8
C4 Spongy	Damage Type 2[2]	1×10^{-9}	40	0.45					1.8
C5 Spongy	Damage Type 2[2]	1×10^{-9}	40	0.45					1.8
C6 Spongy	Damage Type 2[2]	1×10^{-9}	40	0.45					1.8
C7 Spongy	Damage Type 2[2]	1×10^{-9}	40	0.45					1.8

Along with the various material properties assigned to the differing meshes, surface and interaction properties were also assigned to the meshes via surface-to-surface, or other kinematically constrained interaction properties. Three main tying and contact interfaces were incorporated into the head and neck model to ensure that the FE human head and neck model. The first tying interface was the Automatic Single Surface contact, which tied all corresponding meshes to themselves to assure properties remained constant throughout. An example of this tie constraint with Automatic Single Surface contact would be that the skull mesh would react in a uniform fashion, throughout once impacted on acted upon. This reaction would be in such a fashion that different elements of the skull would react upon and transfer force and other properties to their adjacent elements in the skull mesh and the meshed elements of adjacent components of the head and neck while maintaining the compatability condition across the boundaries of adjacent head and neck components. The second interface was the Automatic Surface-to-Surface contact interface that solely dealt with giving the interfaces compatibility condition during the simulation. During the initial verification and comparison FE simulations, the surface-to-surface impact dealt with the cylindrical rod impacting the human head and neck model. Once the sUAS model was obtained the surface to surface interface dealt with the sUAS impacts to the human head and neck model. The third set of interfaces were the surface to node interfaces. These boundary conditions involved aspects such as there was continuity from the head to neck in propagating the stresses and strains arising from the impact boundary conditions. A free surface boundary condition was applied to the bottom surface of the neck and a pinned constrain was applied to the outer edge of the bottom surface of the neck to best represent an actual human head and neck kinematics observed during PMHS impact tests. This was modeled after the amount of force the neck exerts on the 50th percentile human head to resist and compared in accordance with the THUMS model to assure a biofidelic and biomechanically accurate fashion was being obtained and produced. These conditions allowed the model to react more realistically to impact mechanical loads.

2.2.3 Model Design of Experiments

The human head and neck model was initially developed utilizing the cylindrical rod impact to verify impact conditions similar to sUAS-head model impacts. An equilateral angle of 45 degrees was utilized for all the impacts and three impacts sites were used; the frontal, temporal, and occipital portions of the head. Six impact tests were executed utilizing two velocities as shown in the table below. The tests strove to best represent the impact of the drone while utilizing the use of the cylinder and cushion mechanism.

Table 3. A table of old human head and neck model FE simulation's design of experiment

Impact Site	Angle	Velocity (m/s)
Frontal	45	9.4
Frontal	45	6.3
Occipital	45	9.4
Occipital	45	6.3
Temporal	45	9.4
Temporal	45	6.3

2.3 Updated Human Head and Neck FE Model Development Summary

A significantly more defined and adequate set of CT scans was obtained from Ohio State University, which allowed for a much more detailed and anatomically accurate meshing. The CT scans were analyzed and anatomically correct meshes were developed in ScanIP just as in the previous process using the old CT scans. However, due to the higher resolution and quality of the CT scans much finer meshes of each individual part and organ of the human head and neck model were developed.

Once the individual meshes for each part of the human head and neck model were developed they were then imported into LS-DYNA and arranged to conduct sUAS-human head and neck collision simulations. During initial sUAS impact simulations, the meshes were then analyzed for mesh stability. Localized re-meshing was completed to accommodate any instabilities, such as node and element deletion during LS-DYNA FE model implementation, rugged or stray node/element deletion, negative volume or unrealistic deformation, in the human head and neck. Once these issues were corrected during the iterative re-meshing process was completed.

Once an adequate human head and neck FE model was generated the individual meshes were assigned control parameters, as well as mechanical properties for the simulation of the sUAS and human head and neck impacts. The mechanical properties for the human head and neck model were consistent with the THUMS human head and neck model, and the old human head and neck model.

2.3.1 Updated Model of Human Head and Neck Mesh

The current human head and neck model was developed using a much more refined set of CT scans obtained from the Ohio State University. The improved CT scans had a more detailed imaging with the voxel dimensions in the X, Y, and Z axes being 1.2695 mm, 1.2695 mm, and 0.4 mm, respectively. These advancements resulted in; not only an easier meshing process in terms of smoothing and eroding, but also a more anatomically correct head and neck model in comparison to the old human head and neck model. The current CT scans being utilized can be seen in the Figure 4.

As expected the number of elements and nodes for the updated human head and neck model for each individual component differed from the old human head and neck model. Due to the more precise CT scan being used, in general, the overall number of nodes and elements were increased. The total number of elements and nodes for each individual mesh can be seen in the Table 4.

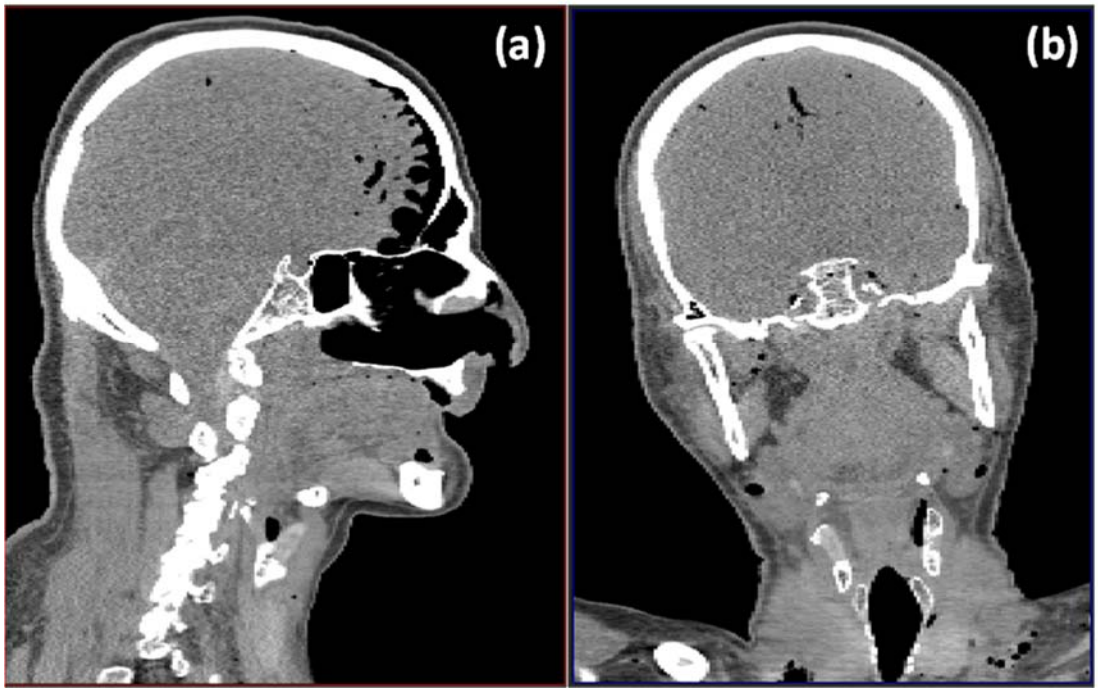

Figure 4. (a) X axis and (b) Y axis orientation of current OSU PHMS CT scans

Table 4. A table of mesh element and node numbers for the updated and current human head and neck model

Meshed Part	Number of Elements	Number of Nodes
Falx	87,278	349,112
Grey Matter	531,656	2,126,624
White Matter	1,062,872	4,251,488
C7 Vertebrae	59,966	239,864
C6 Vertebrae	54,943	219,772
C5 Vertebrae	48,628	194,768
C4 Vertebrae	48,692	193,648
C3 Vertebrae	47,412	189,648
C2 Vertebrae	57,412	229,648
C1 Vertebrae	55,890	223,560
Skull Spongy	1,257,981	5,031,924
Skull Cortical	1,667,761	6,671,044
Spinal Cord	36,285	145,140
CSF	583,805	2.335,220
Skin	2,778,132	11,112,528
Vertebral Disk	21,070	84,280
C7 Vertebrae Spongy	12,856	51,424
C6 Vertebrae Spongy	15,802	63,208
C5 Vertebrae Spongy	16,791	67,164
C4 Vertebrae Spongy	17,572	68,176
C3 Vertebrae Spongy	17,044	68,176
C2 Vertebrae Spongy	21,876	87,504
C1 Vertebrae Spongy	15,724	62,896

The updated mesh of head and neck human model can be seen below in Figures 5 - 8. The smoothness of the meshes in the model has helped alleviate element distortions when exposed to various forces, stresses, and deformations during impact simulations. Each individual component of the human head and neck model is summarized and shown below in Figure 5.

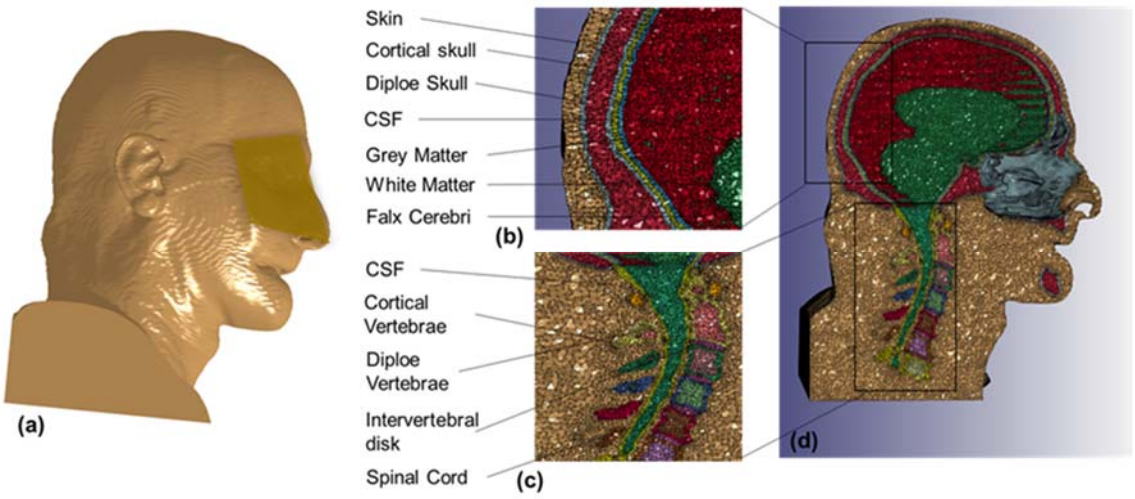

Figure 5. (a) Side view of the human head and neck model along with closeup sagittal view of (b) the interior cranial meshes, and (c) the brain stem and spinal system, and (d) sagittal cut of the human head and neck model

The skin model was composed of 2,778,132 elements and defined by a viscoelastic material property representation. The parameters were set to a density of 1×10^{-9} ton/mm^3, a bulk modulus of 2880.00 MPa, a short-term shear modulus of 7.39 MPa, a long term shear modulus of 2.36 MPa, and a decay constant of 0.1. These parameters were implemented to ensure that the skin behaved in a mechanically appropriate fashion when the sUAS made contact with the skin during the impact simulations. The cortical skull model was composed of 1,667,761 elements and defined by an elastic material property. The parameters were set to a density of 2×10^{-9} ton/mm^3, a young's modulus of 1×10^4 MPa, and a Poisson's ratio of 0.22. The diploe part of the skull model was composed of 1,257,981 elements and defined by an elastic material property representation. The parameters were set to a density of 1×10^{-9} ton/mm^3, a Young's modulus of 390 MPa, and a Poisson's ratio of 0.19. The white matter model was composed of 1,062,872 elements and defined by viscoelastic material properties. The parameters were set to a density of 1×10^{-9} ton/mm^3, a bulk modulus of 2160 MPa, a short term shear modulus of 0.0125 MPa, a long term shear modulus of 0.006125 MPa, and a decay constant of 0.06. The grey matter model was composed of 531,656 elements and was also defined by viscoelastic material properties. The parameters were set to a density of 2×10^{-9} ton/mm^3, a bulk modulus of 2190 MPa, a short term shear modulus of 0.01 MPa, a long term shear modulus of 0.005 MPa, and a decay constant of 0.06. The white matter, along with the grey matter, were of prime importance for the analysis localized brain injury metrics. The falx cerebri model was composed of 87,278 elements and defined by elastic material properties. The parameters were set to a density of 1.13×10^{-9} ton/mm^3, a young's modulus of 31.50 MPa, and a Poisson's ratio of 0.45. The falx was set as a dividing membrane between the two hemispheres, and represented the meningeal layer formed in real life specimens. The spinal cord model was composed of 36,285 elements and defined b viscoelastic material properties. The parameters were set to a density of 1×10^{-9} ton/mm^3, a bulk modulus of 2190 MPa, a short term shear modulus of 1, a long term shear modulus of 0.20 MPa, and a decay constant of 0.6. The cerebral spinal fluid model was composed of 583,805 elements and was defined by the mechanical fluid of elastic fluid. Fluids are difficult to model in LS-DYNA; however, the mechanical properties of the elastic fluid parameter met the criteria rather well in terms of resultant propagation that would be seen in cerebral spinal fluid, as well as the viscoelastic properties of the fluid.

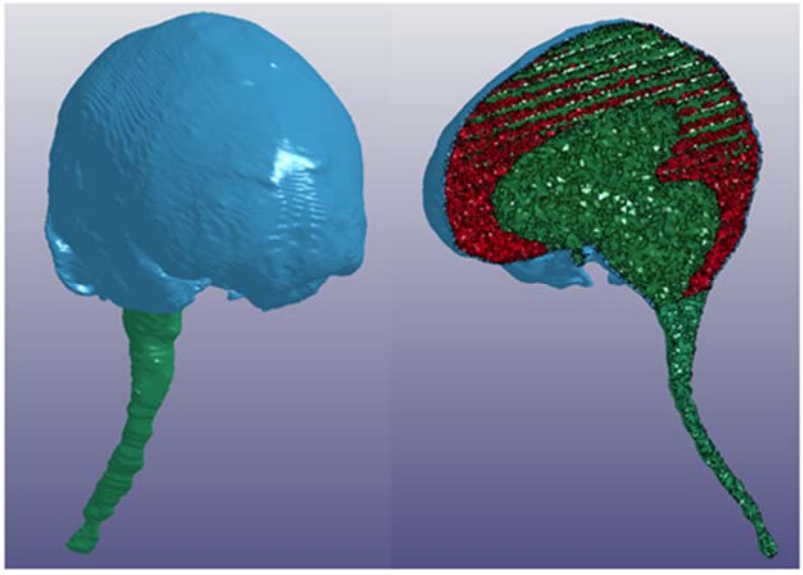

Figure 6. FE mesh of the brain and brain stem for the updated and current human head and neck model

The cortical C1- C7 vertebra models were defined by a plastic material property representation. The parameters were set to a density of 2×10^{9} ton/mm^3, a young's modulus of 1.3e004, a Poisson's ratio of .3, and a yield stress of 80 MPa. The spongy C1 – C7 vertebra models were defined by a Damage Type 2 material property representation. The parameters were set to a density of 1×10^{9}, a young's modulus of 40, a Poisson's ratio of 0.45, and a yield stress of 1.8 MPa. The Damage Type 2 property was given to the spongy aspect of the vertebrae because it helped establish the rigidness yet malleability that the vertebrae can exhibit under normal loading conditions. The intervertebral disc model was composed of 21,070 elements and defined by Fu Chang Foam material properties[3,4]. The parameters were set to a density of 1×10^{-9} ton/mm^3, a Young's modulus of 35.70 ton/mm^3, and a termination stress of -9.5×10^{14} MPa. The Fu Chang Foam was ideal for the intervertebral discs because the material is designed for excessive loading forces. Representations of the skeletal system and the spine of the human head and neck model are given below in Figures 7 and 8, respectively.

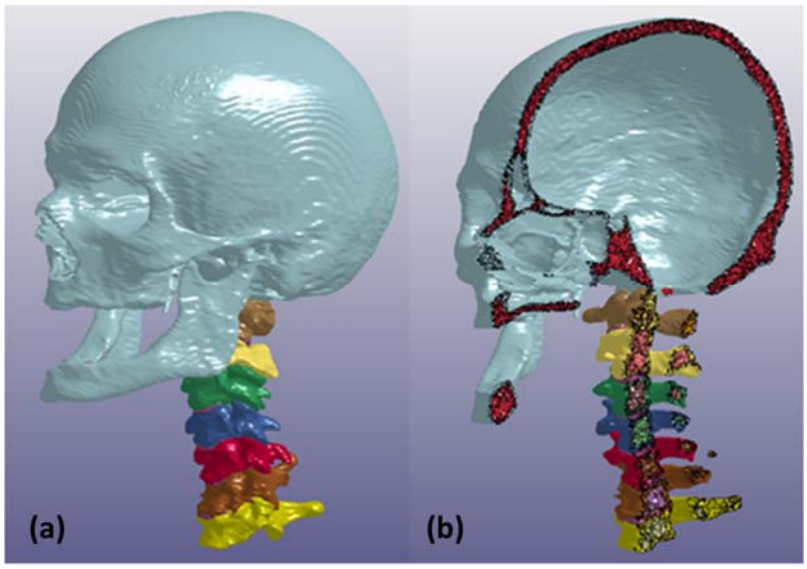

Figure 7. (a) Side view of the skeletal system of the human head and neck model and (b) a sagittal cut of the human head and neck model

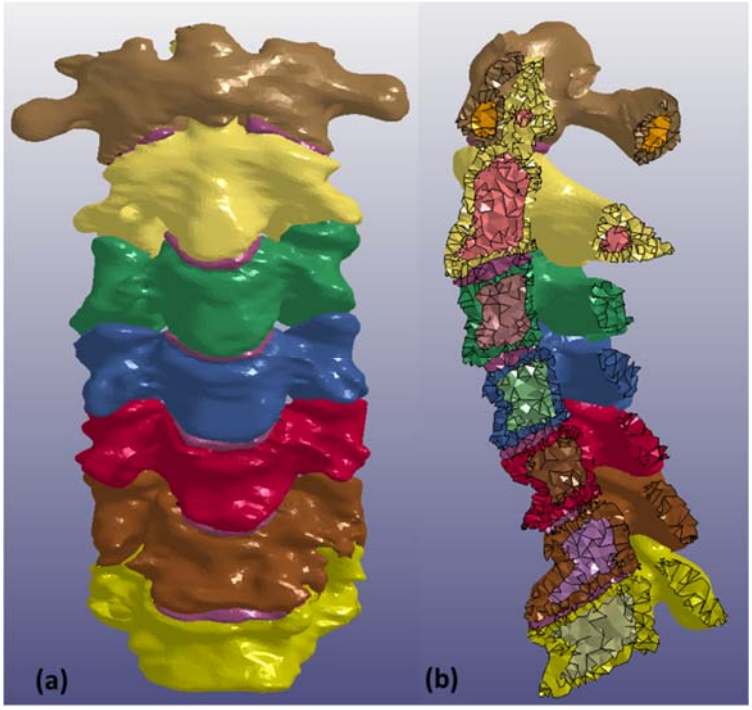

Figure 8. (a) Front view and (b) sagittal cut of the cervical vertebrae of the human head and neck model

2.3.2 Updated Human Head and Neck Model Material, Surface, and Interaction Properties

The same model material properties, surface properties, and interaction properties that were utilized in the old head and neck human model were again used for the current head and neck human model. These material, surface, and interaction properties follow in coordination with the Toyota THUMS model[2]. For a complete listing of the material properties of each individual mesh Table 2 in Section 2.2.2 can be referenced as a whole in terms of verification and comparison for the overall choice in these properties.

2.3.3 Updated Model Design of Experiments

The updated design of experiments revolved around simulating PMHS sUAS impact experiments that were conducted by OSU, and by using the Phantom III sUAS FE model developed by NIAR. 15 individual cases of the experimental OSU PMHS sUAS impact tests were simulated using the Human Head and Neck Model. Five cases each from the first three PMHS experimental tests were utilized as the foundation of the design of experiments. The four unique impact orientations that were used for the simulations were a frontal impact of 58 degrees, a side impact of 0 degrees, a side impact of 58 degrees, and a vertical impact to the top of the head of 90 degrees. VICON data was obtained from OSU from their PMHS impact Tests and this data was then applied to the human head and neck model impact simulations to determine the precise location of impact and sUAS orientation for each individual case. An overview of the impact cases is given below, in Table 5, in terms of the speed, kinetic energy, and angle of impact of the sUAS.

Table 5. A table of OSU sUAS-PMHS impact cases simulated in LS-DYNA

Case Number	sUAS	Impact Orientation	Velocity (fps)	Angle of Impact (degrees)	Impact Kinetic Energy (ft-lbs)
UA19A-43	Phantom III	Frontal	56	58	130
UA19A-44	Phantom III	Frontal	61	58	154
UA19A-84	Phantom III	Right Side	56	0	130
UA19A-85	Phantom III	Right Side	61	0	154
UA19A-86	Phantom III	Right Side	71	0	209
UA19A-29	Phantom III	Top	55	90	125
UA19A-30	Phantom III	Top	71	90	209
UA19A-44	Phantom III	Frontal	61	58	154
UA19A-108	Phantom III	Frontal	71	58	209
UA19A-41	Phantom III	Right Side	61	58	154
UA19A-41	Phantom III	Right Side	61	58	154
UA19A-42	Phantom III	Right Side	71	58	209
UA19A-108	Phantom III	Frontal	71	58	209
UA19A-29	Phantom III	Top	65	90	175
UA19A-30	Phantom III	Top	71	90	209

2.3.4 Updated Human Head and Neck Model Verification

Verification and comparison of the negative and positive pressure responses of the finite element head and brain response aspect of the model was achieved by recreating Nahum et al.[1] cadaveric experiments, in which cadavers were impacted via the frontal lobe of the head and brain and pressure transducers recorded the pressure response of the brain due to blunt impacts. The FE simulation, using Nahun et al.'s PMHS impact test, was conducted to verify and compare the human head and neck FE model impact simulations with experimental data. The pressure over time was recorded in the simulations and the data was then compared to Nahum et al.'s[1] pressure over time experimental data. The pressure versus time data is then graphed and modeling data compared with experimental data. Differing impact loads

will result in differing pressure values; however, the overall aspect of the graphing of the pressure over time curve will be similar for comparison.

The pressure versus time curve for the frontal lobe is represented by fairly linear increase of pressure until the maximum pressure is met, then followed by a fairly linearly decrease in pressure finishing out in an exponential decrease in pressure as the material composition of the brain and head starts to have large deformation. Figure 9 shows the experimental comparison of the human head and neck model.

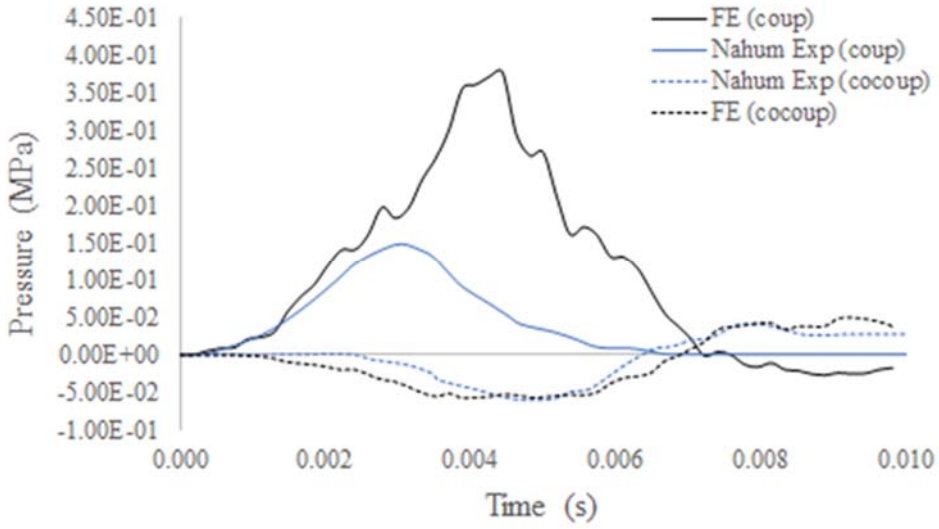

Figure 9. Current human head neck model comparison to Nahum et al.'s PMHS experimental data

2.4 Updated Human Head and Neck Model Correlation

The current model data verification and data analysis process was compared to that of OSU's PMHS sUAS impact experimental tests in which data was obtained and used for the parameters human head and neck impact simulations should have comparable data. The overall results from the impact simulations in terms of peak linear accelerations were overall comparable to those obtained by the OSU impact scenarios. The average peak acceleration difference between MSU's modeling results and OSU's PMHS test data was 14%. The data values of the OSU experimental sUAS PMHS impacts and the data values from the MSU human head and neck model impact simulations are shown in Table 6.

Table 6. A Table of input parameters and brain injury metrics for sUAS-Human head and neck impact cases from OSU and MSU

Case Orientation	Impact Orientation	Velocity (fps)	Angle of Impact (degrees)	OSU Peak Acceleration (g)	MSU Peak Acceleration (g)	OSU HIC	MSU HIC	OSU BrIC	MSU BrIC
UA19A-43	Frontal	56	58	240	240	521.9	1244	0.43	0.2614
UA19A-44	Frontal	61	58	237	245	1303.8	1384	0.5	0.245
UA19A-84	Frontal	56	0	300	360	865.7	1593	0.42	0.405
UA19A-85	Frontal	61	0	340	330	1076.1	1632	0.48	0.5525
UA19A-86	Frontal	71	0	510	500	2892.5	2988	0.55	0.7013
UA19A-29	Top	56	90	410	300	1848.2	1732	0.35	0.1284
UA19A-30	Top	71	90	570	510	4197.1	2321	0.26	0.2881
UA19A-44	Frontal	61	58	210	165	379.6	386	0.51	0.2537
UA19A-108	Frontal	71	58	650	550	538.8	3141	0.56	0.3304
UA19A-41	Right	61	58	253	240	500.3	1434	0.32	0.5386
UA19A-41	Right	61	58	270	340	411.7	1056	0.36	0.4299
UA19A-42	Right	71	58	390	360	2527.1	2048	0.43	0.5732
UA19A-108	Frontal	71	58	670	550	5473.4	3141	0.5	0.3307
UA19A-29	Top	61	90	370	340	1219	2111	0.35	0.1463
UA19A-30	Top	71	90	330	360	1747.9	2980	0.36	0.2017

The data obtained above was calculated using various methods. Peak acceleration values, as well as, rotational velocity values used to determine BrIC were obtained through the Human Head and Neck Model impact simulations by utilizing a system of interpolations that defined a master node set at the models center of gravity within the brain. Once the center of gravity master node had been set, a series of slave nodes were given to it that would interpolate and systematically relay data to which resulted in an overall more accurate mechanical parameter production in terms of simulating data that was obtained from the OSU PMHS experimental impacts. There were 17,000 slave nodes located throughout the brain that were assigned to the master node located at the center of gravity of the model. This interpolation process resulted in a more accurate acceleration pattern and magnitude. These acceleration profile were then compared to the results from OSU PMHS data.

HIC values were calculated within LS-DYNA through a process function within the program. These HIC values were calculated after adequate filtering (low pass filter for a threshold of 1000 Hz). The data was separated into x, y, and z coordinates then filtered individually to assure that the peak magnitudes of the resultant accelerations were not skewed by the filtering taking place on the magnitude of the resultant acceleration.

BrIC values were calculated from the x, y, and z coordinates of the rotational velocities obtained from the interpolation process. These values were then compared in the fashion that was used with the peak acceleration and HIC values from OSU. Differences in the values of the HIC and BrIC numbers can be accredited to the acceleration and angular velocity graphs of the MSU and OSU data not being exactly equivalent. The results of each individual case are further presented in the results sections, in which the case figures and resultant values are given. This data can then further be compared with the presented OSU data presented from previous sections.

3 RESULTS

The following sections contain the results obtained from each individual simulated case. The results give a visual representation of each individual sUAS to Human Head and Neck Model impact simulation, a figure representing the linear acceleration propagation through the brain, graphs of the linear acceleration and angular velocity taken from the interpolation method used on the center of gravity master node of the brain model with correlated HIC and BrIC values, graph representation of the x, y, and z coordinates of angular velocity, and a pressure propagation contour frame set to represent the likelihood of concussion.

The visual sequences of these impact scenarios further illustrate the impact mechanics and provides an insight in to the human head's response of each impact scenario case. Here, each individual case's orientation of impacts for the FE simulation was taken from the VICON data obtained from OSU's PMHS test.

The linear acceleration and angular velocity resultant graphs give an insight into how the Human Head and Neck Model reacted to the various impact orientations and also gave data to represent how these parameters propagated through the model in terms of the center of gravity of the head. The units for the linear acceleration in LS-DYNA simulations were given in the units of mm^2/s and were converted to gravitational acceleration units or g's and a threshold of 350 g's was given to represent the propagation of linear acceleration of or over 350 g's throughput the brain.

Pressure propagation through the brain was quantified with a 230 KPa threshold[5]. The units of the FE simulation data were assessed in MPa and then converted to KPa. The data was used to determine if concussion would occur if the 230 KPa limit was reached or exceeded, and this was represented by the coloring of the contour plots in the sagittal cut of the brain during the impact simulation.

[5] Ward C, Chan M, Nahum A, (1980) Intracranial pressure – a brain injury criterion. SAE Technical Paper 801304, 1980

3.1 PMHS-Frontal-56 fps-58°-Subject 1

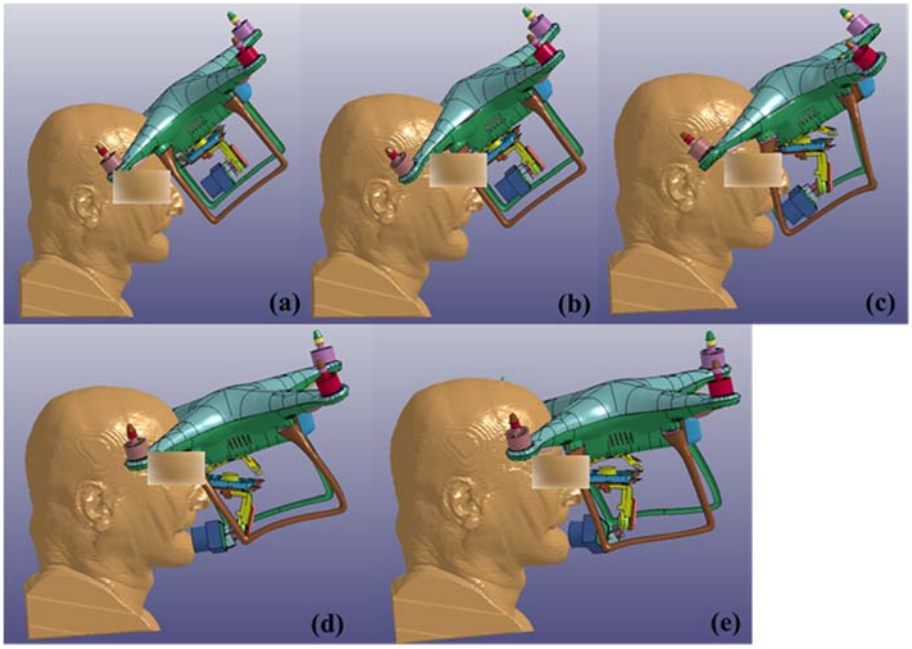

Figure 10. FE simulation snapshots of sUAS impact to human head and neck model at (a) initial contact, (b) after first time step, (c) after second time step, (d) after third time step, and (d) final time step before disassociation between models

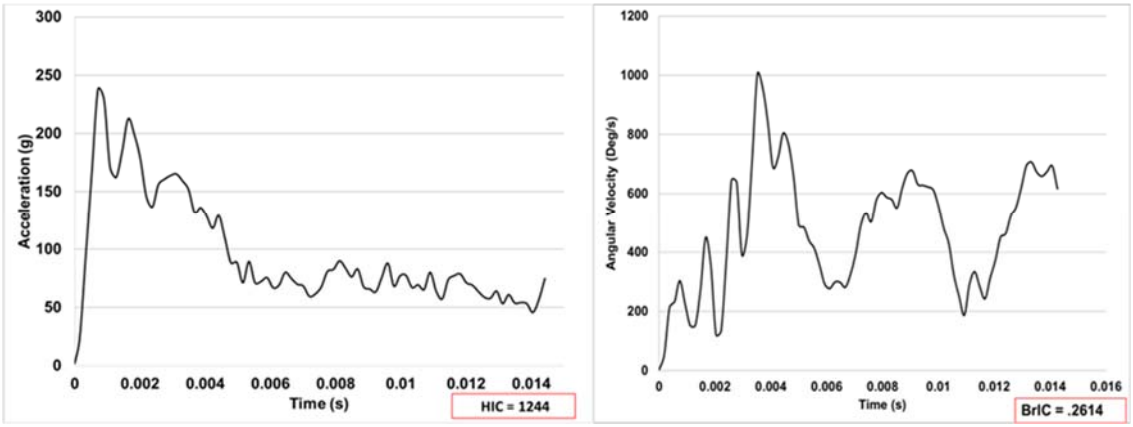

Figure 11. Resultant acceleration and angular velocity plots for sUAS-human head and neck impact simulation with corresponding HIC and BrIC values

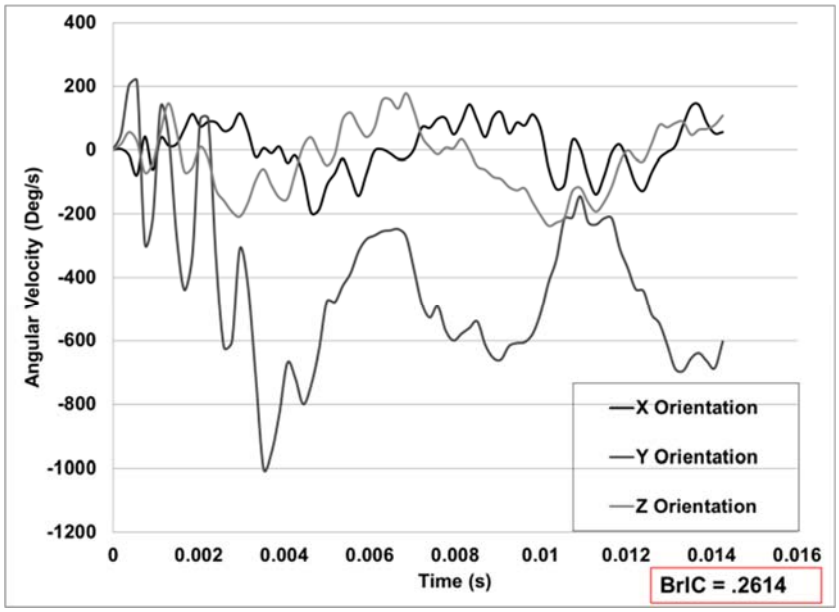

Figure 12. Angular velocity components for sUAS-human head and neck impact simulation with corresponding BrIC value

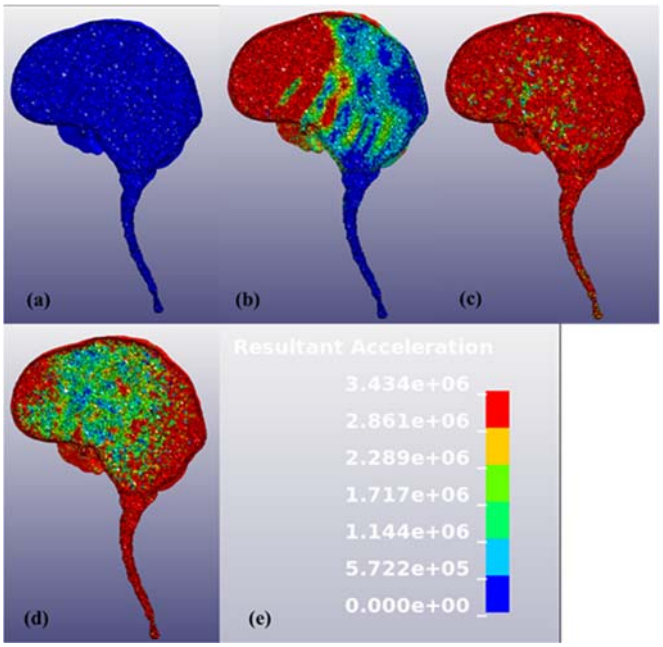

Figure 13. Brain sagittal cut snapshots of FEA acceleration contours at (a) initial impact, (b) after first time step of initial impact, (c) at time step corresponding to peak pressure values, (d) at time step when models start recoiling, and (e) acceleration contour scale (mm/s)

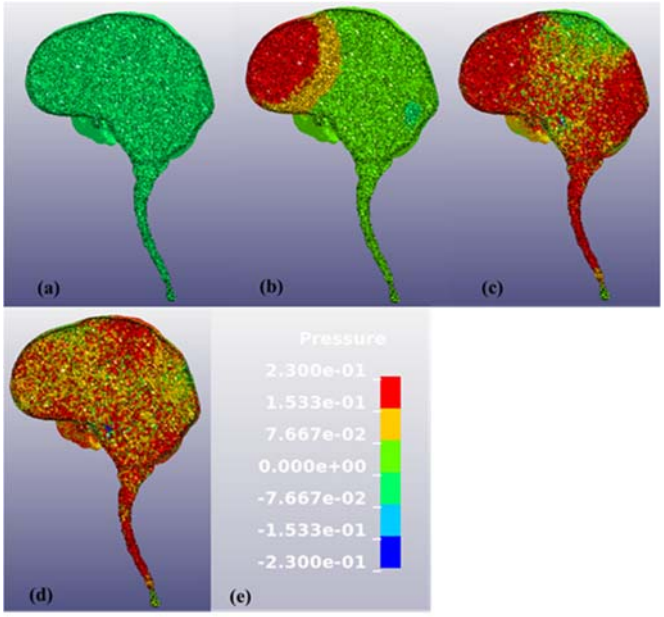

Figure 14. Brain sagittal cut snapshots of FEA pressure contours at (a) initial impact, (b) after first time step of initial impact, (c) at time step corresponding to peak pressure values, (d) at time step when models start recoiling, and (e) pressure contour scale (MPa)

3.2 PMHS-Frontal-61 fps-58°-Subject 1

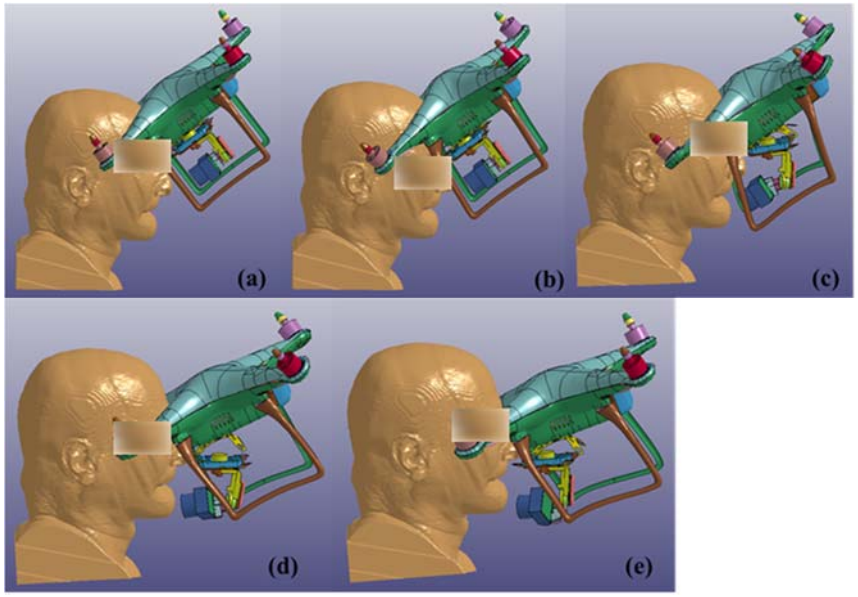

Figure 15. FE simulation snapshots of sUAS impact to human head and neck model at (a) initial contact, (b) after first time step, (c) after second time step, (d) after third time step, and (d) final time step before disassociation between models

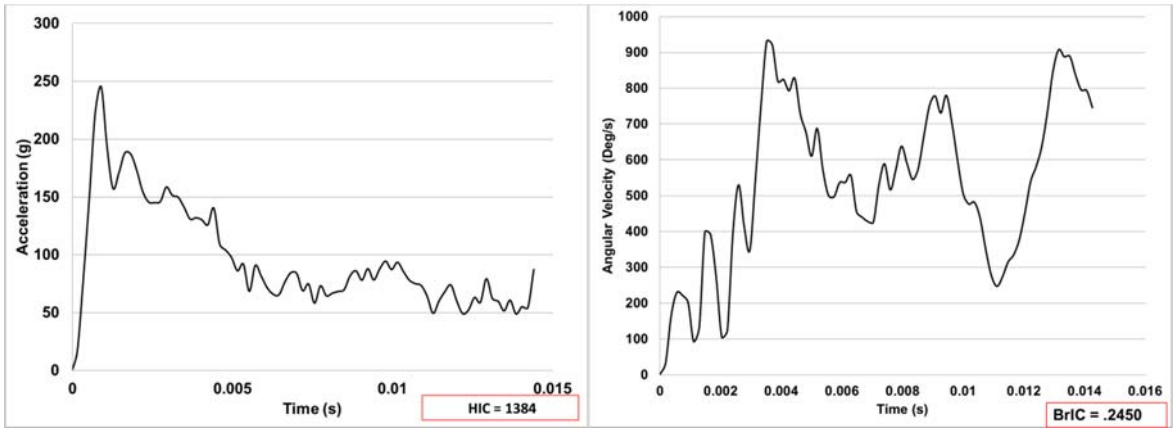

Figure 16. Resultant acceleration and angular velocity graphs for sUAS-human head and neck impact simulation with Corresponding HIC and BrIC values

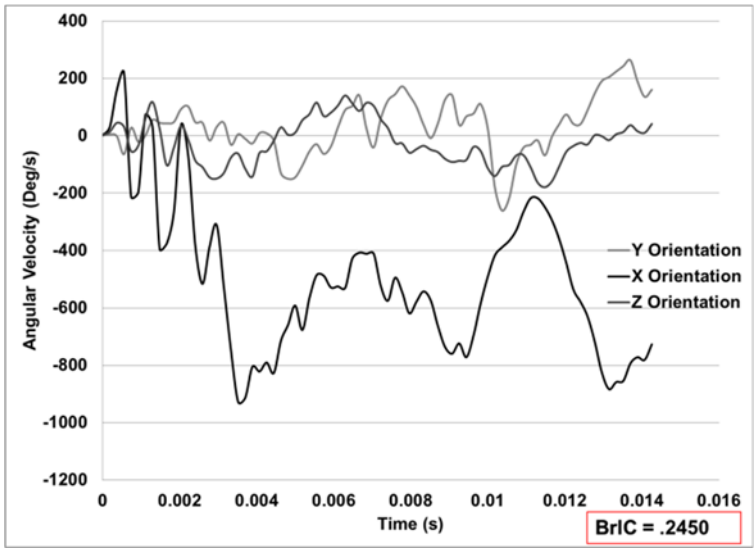

Figure 17. Angular velocity components for sUAS-human head and neck impact simulation with corresponding BrIC value

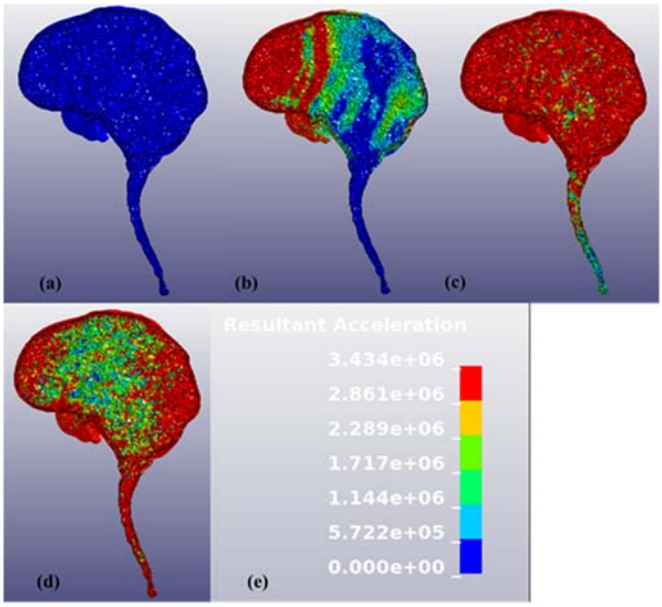

Figure 18. Brain sagittal cut snapshots of FEA acceleration contours at (a) initial impact, (b) after first time step of initial impact, (c) at time step corresponding to peak pressure values, (d) at time step when models start recoiling, and (e) acceleration contour scale (mm/s)

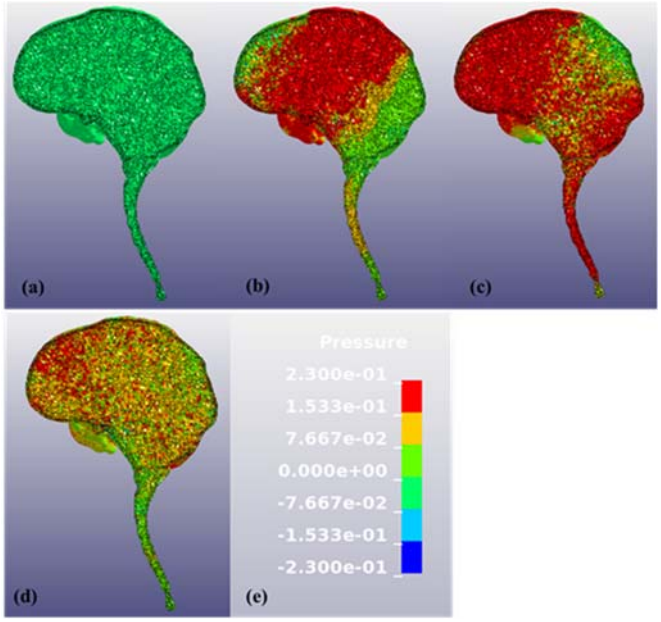

Figure 19. Brain sagittal cut snapshots of FEA pressure contours at (a) initial impact, (b) after first time step of initial impact, (c) at time step corresponding to peak pressure values, (d) at time step when models start recoiling, and (e) pressure contour scale (MPa)

3.3 PMHS-Side-56 fps-0°-Subject 1

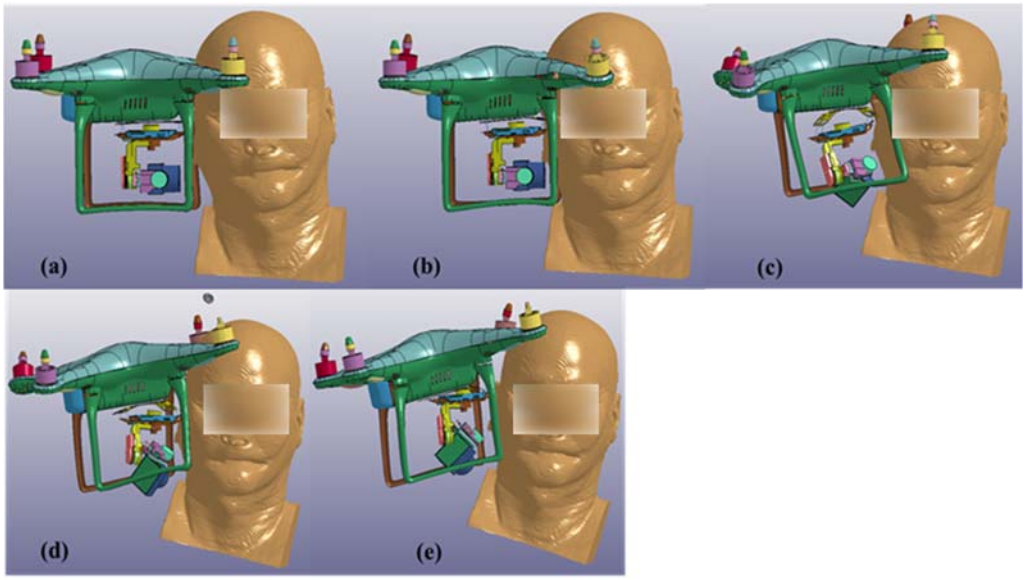

Figure 20. FE simulation snapshots of sUAS impact to human head and neck model at (a) initial contact, (b) after first time step, (c) after second time step, (d) after third time step, and (d) final time step before disassociation between models

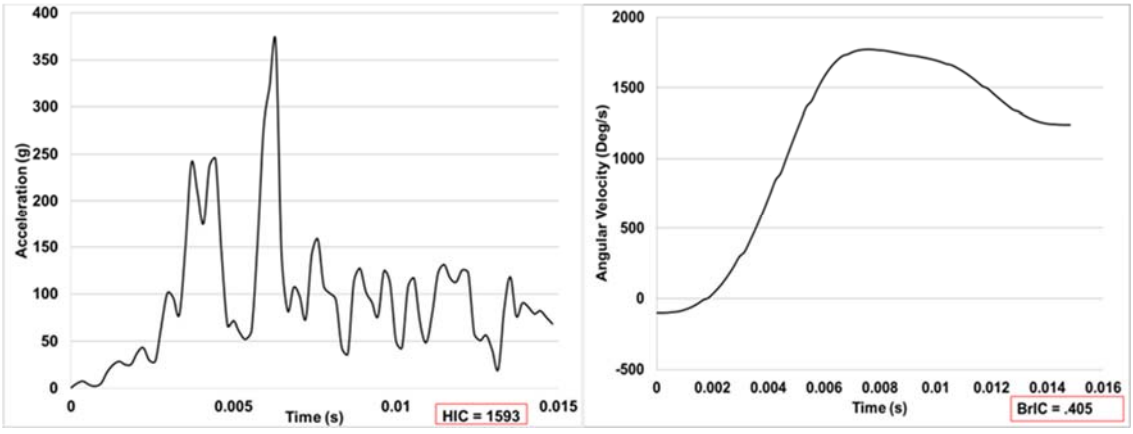

Figure 21. Resultant acceleration and angular velocity graphs for sUAS-human head and neck impact simulation with corresponding HIC and BrIC values

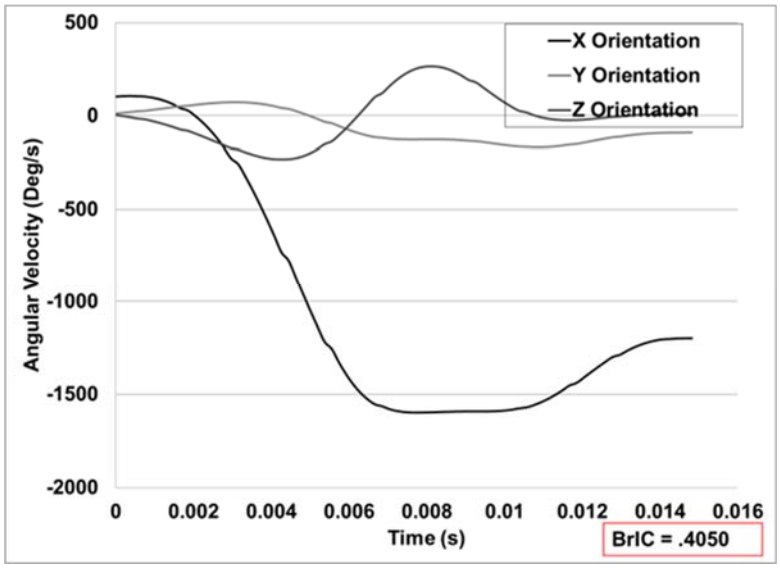

Figure 22. Angular velocity components for sUAS-human head and neck impact simulation with corresponding BrIC value

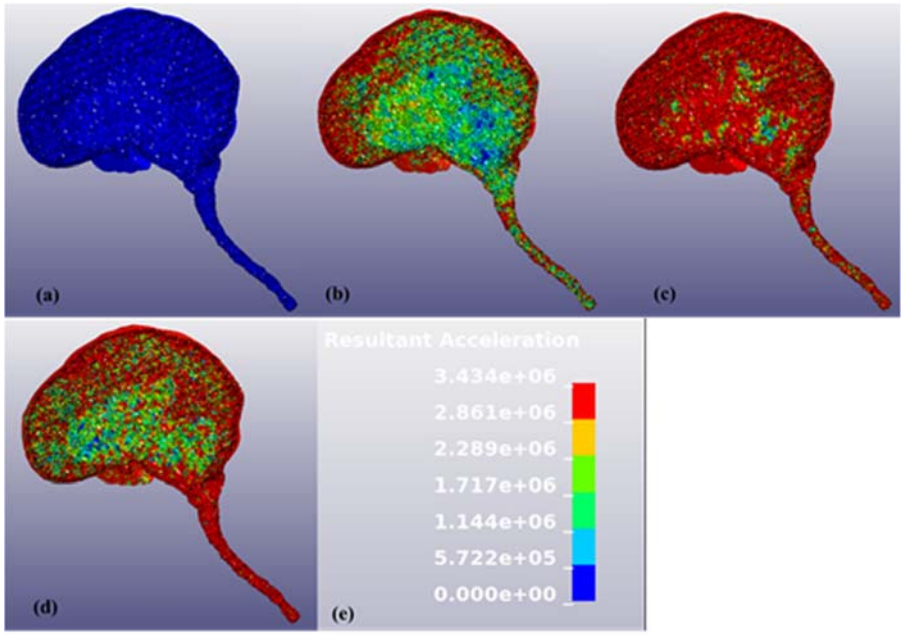

Figure 23. Brain sagittal cut snapshots of FEA acceleration contours at (a) initial impact, (b) after first time step of initial impact, (c) at time step corresponding to peak pressure values, (d) at time step when models start recoiling, and (e) acceleration contour scale (mm/s)

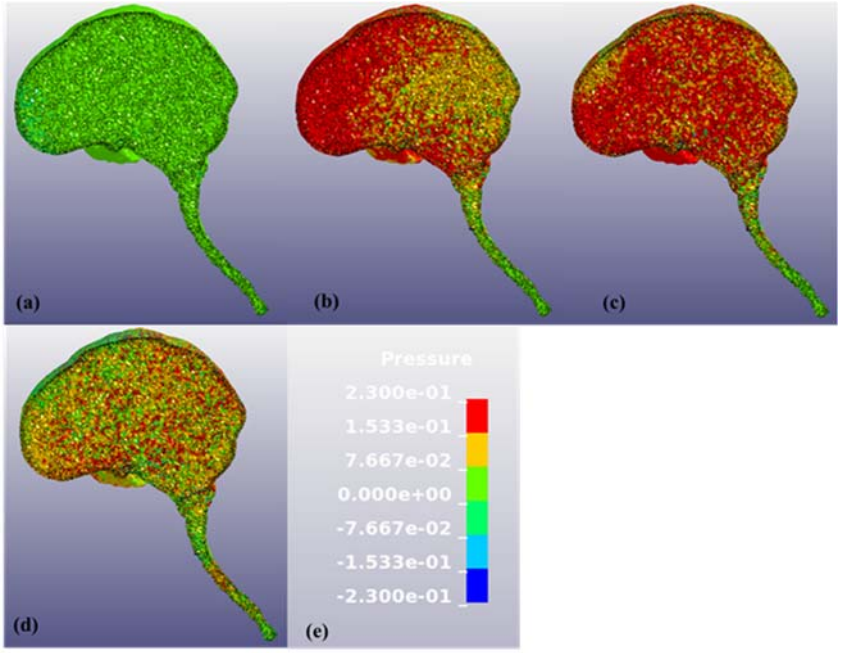

Figure 24. Brain sagittal cut snapshots of FEA pressure contours at (a) initial impact, (b) after first time step of initial impact, (c) at time step corresponding to peak pressure values, (d) at time step when models start recoiling, and (e) pressure contour scale (MPa)

3.4 PMHS-Side-61 fps-0°-Subject 1

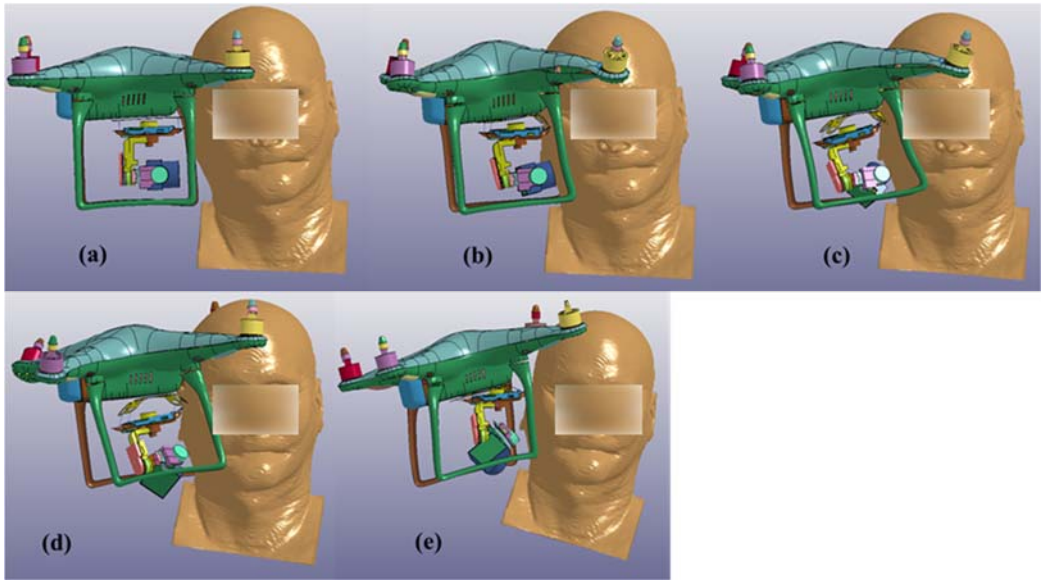

Figure 25. FE simulation snapshots of sUAS impact to human head and neck model at (a) initial contact, (b) after first time step, (c) after second time step, (d) after third time step, and (d) final time step before disassociation between models

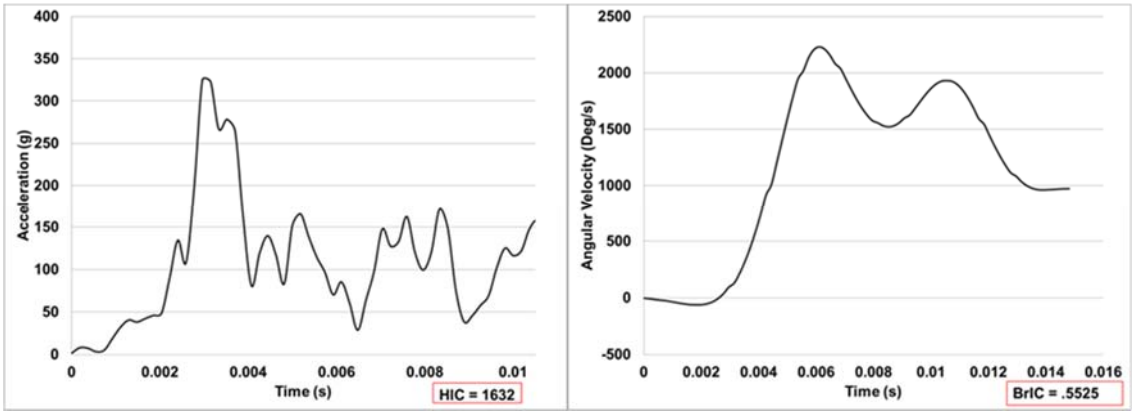

Figure 26. Resultant acceleration and angular velocity graphs for sUAS-human head and neck impact simulation with corresponding HIC and BrIC values

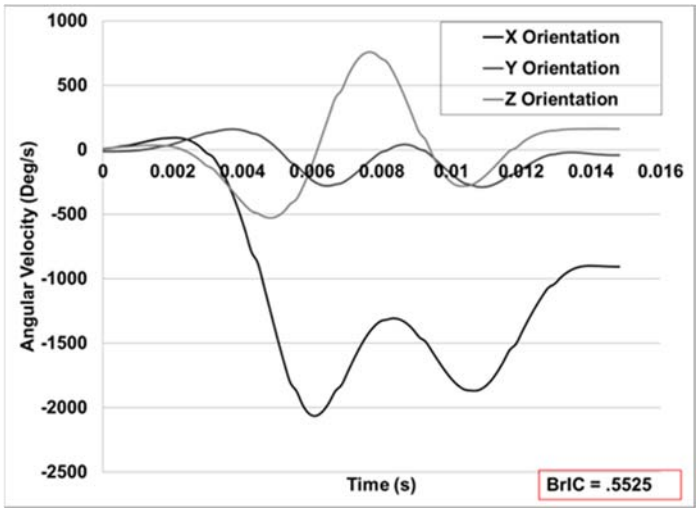

Figure 27. Angular velocity components for sUAS-human head and neck impact simulation with corresponding BrIC value

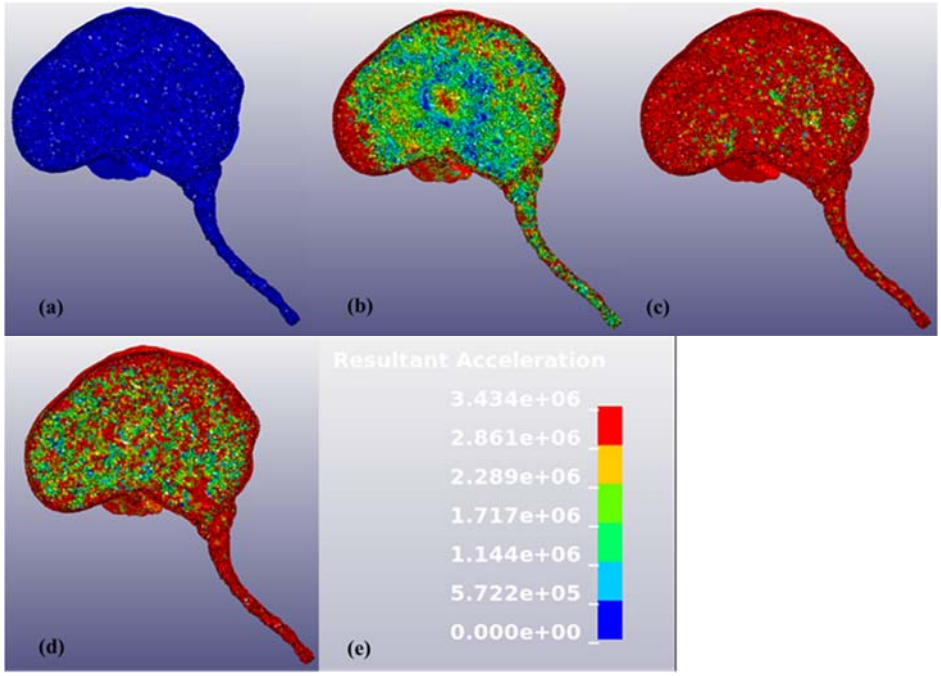

Figure 28. Brain sagittal cut snapshots of FEA acceleration contours at (a) initial impact, (b) after first time step of initial impact, (c) at time step corresponding to peak pressure values, (d) at time step when models start recoiling, and (e) acceleration contour scale (mm/s)

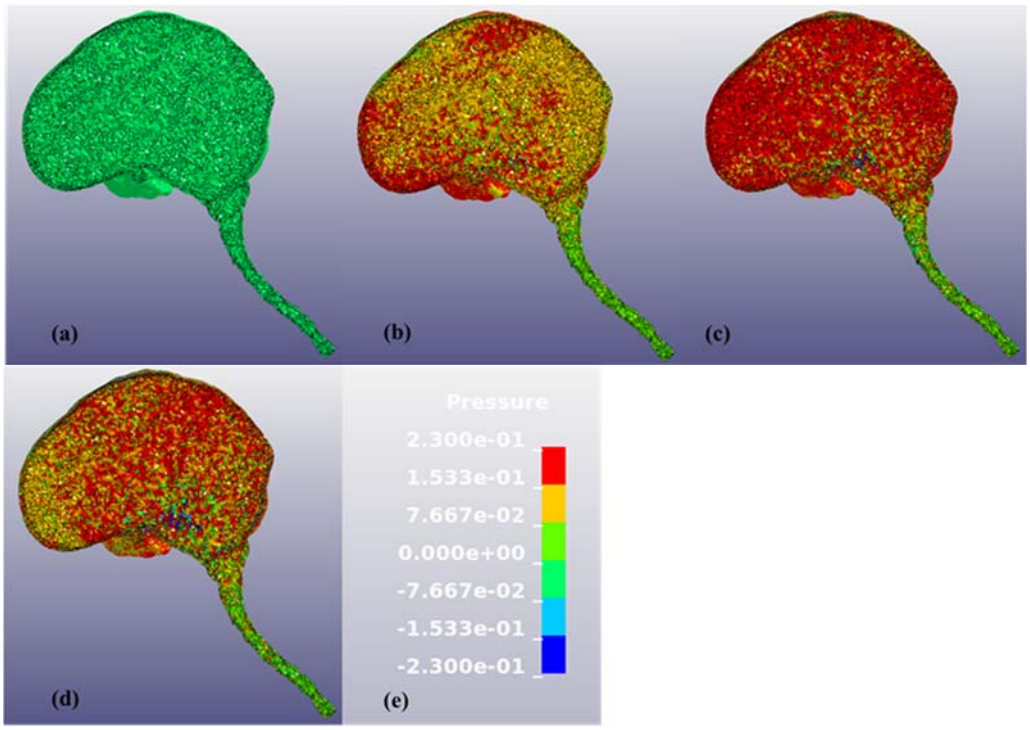

Figure 29. Brain sagittal cut snapshots of FEA pressure contours at (a) initial impact, (b) after first time step of initial impact, (c) at time step corresponding to peak pressure values, (d) at time step when models start recoiling, and (e) pressure contour scale (MPa)

3.5 PMHS-Side-71 fps-0°-Subject 1

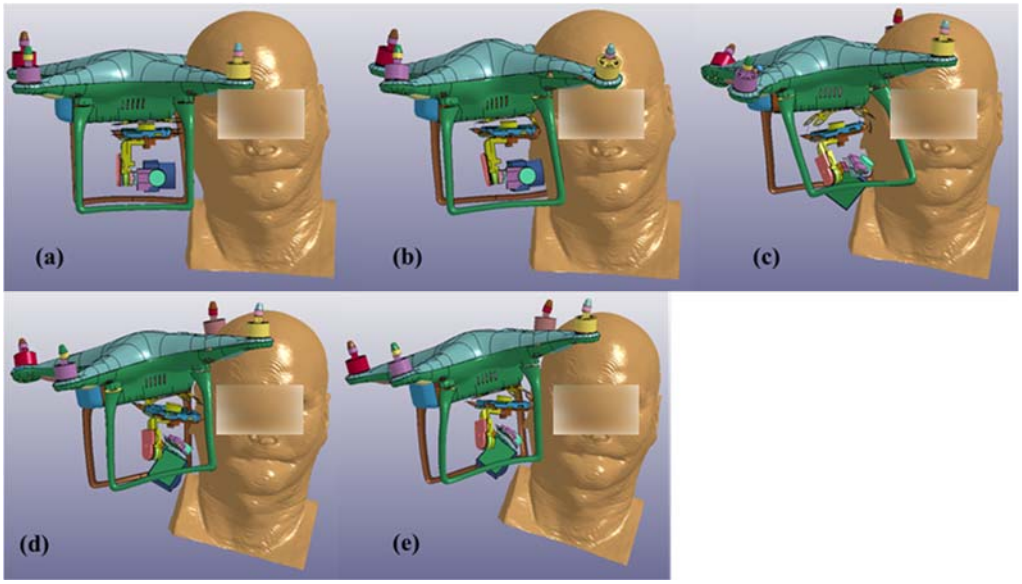

Figure 30. FE simulation snapshots of sUAS impact to human head and neck model at (a) initial contact, (b) after first time step, (c) after second time step, (d) after third time step, and (d) final time step before disassociation between models

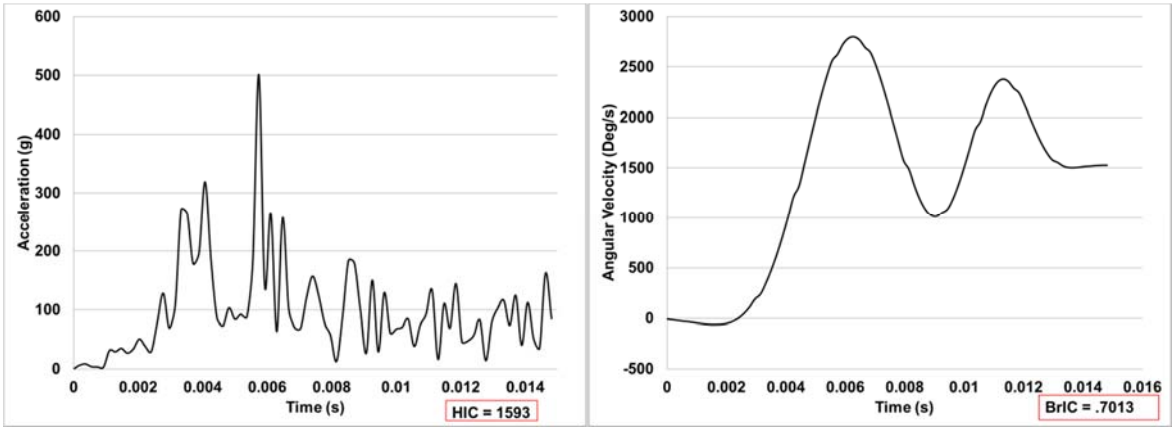

Figure 31. Resultant acceleration and angular velocity graphs for sUAS-human head and neck impact simulation with corresponding HIC and BrIC values

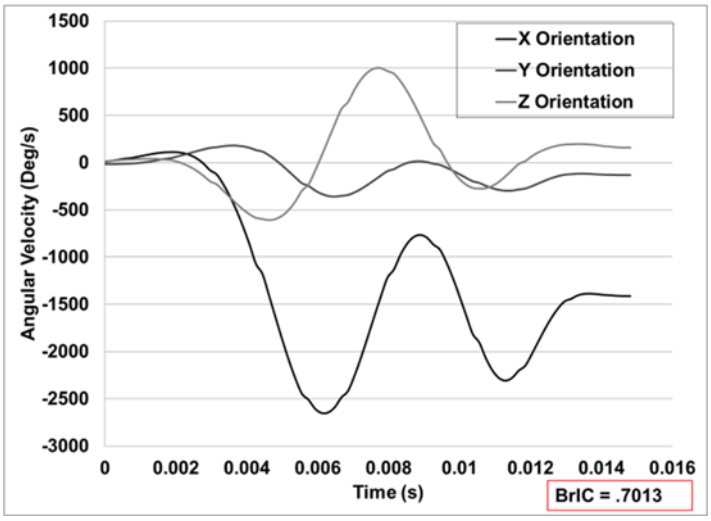

Figure 32. Angular velocity components for sUAS-human head and neck impact simulation with corresponding BrIC value

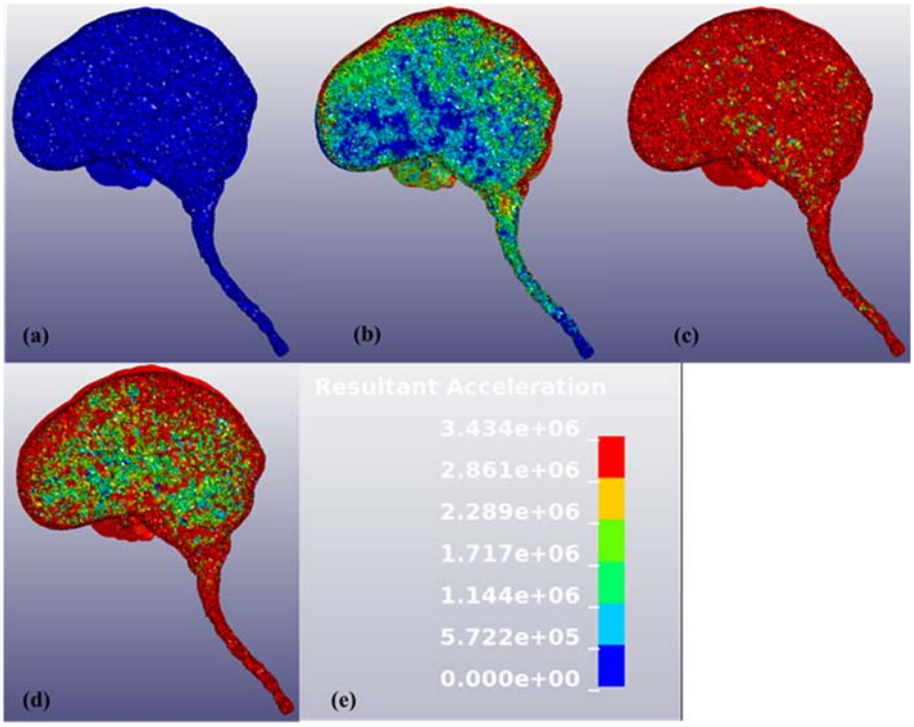

Figure 33. Brain sagittal cut snapshots of FEA acceleration contours at (a) initial impact, (b) after first time step of initial impact, (c) at time step corresponding to peak pressure values, (d) at time step when models start recoiling, and (e) acceleration contour scale (mm/s)

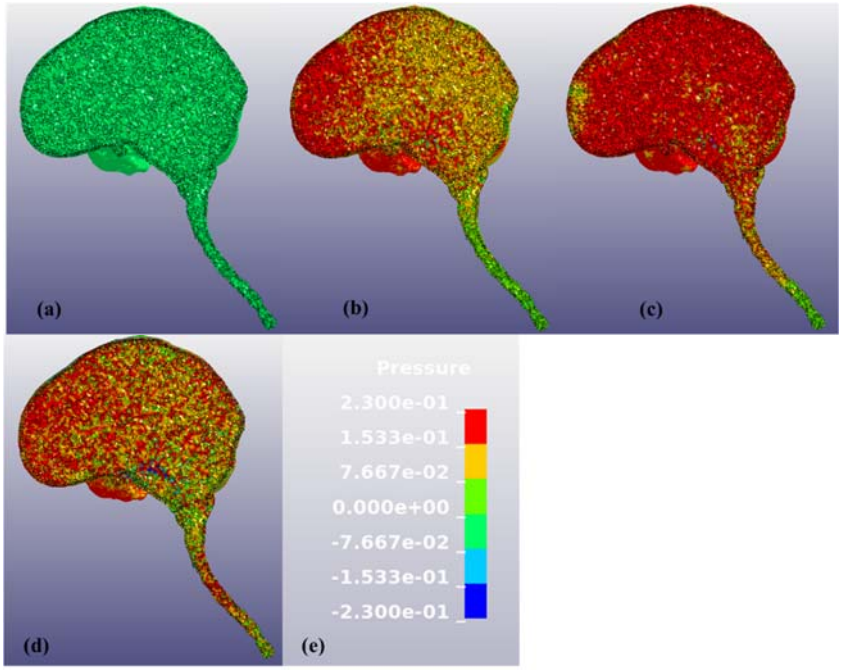

Figure 34. **:** Brain sagittal cut snapshots of FEA pressure contours at (a) initial impact, (b) after first time step of initial impact, (c) at time step corresponding to peak pressure values, (d) at time step when models start recoiling, and (e) pressure contour scale (MPa)

3.6 PMHS-Top-55 fps-90°-Subject 2

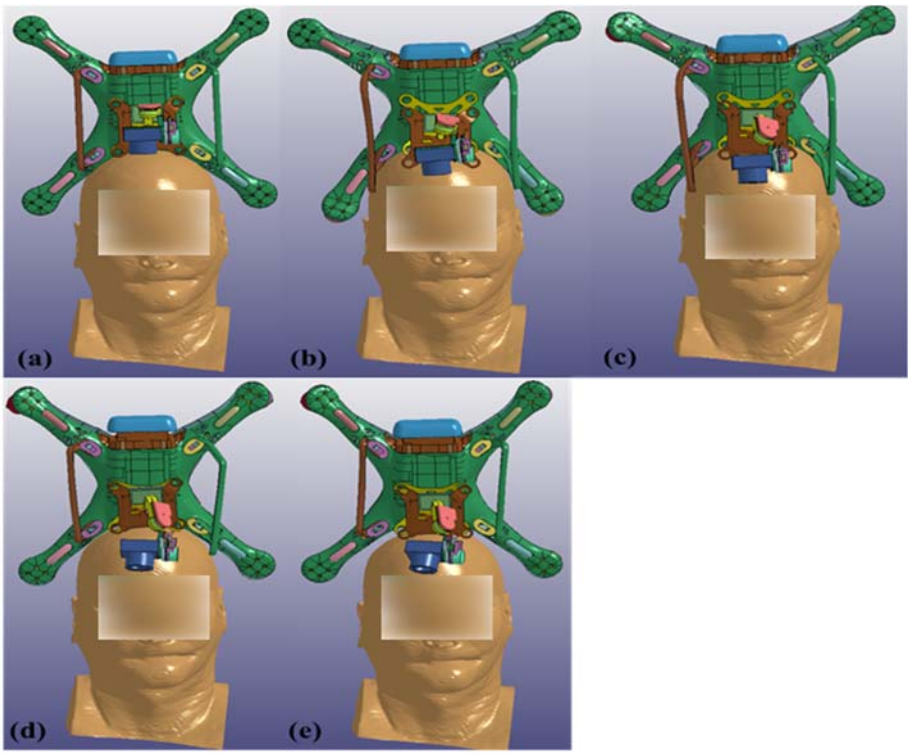

Figure 35. FE simulation snapshots of sUAS impact to human head and neck model at (a) initial contact, (b) after first time step, (c) after second time step, (d) after third time step, and (d) final time step before disassociation between models

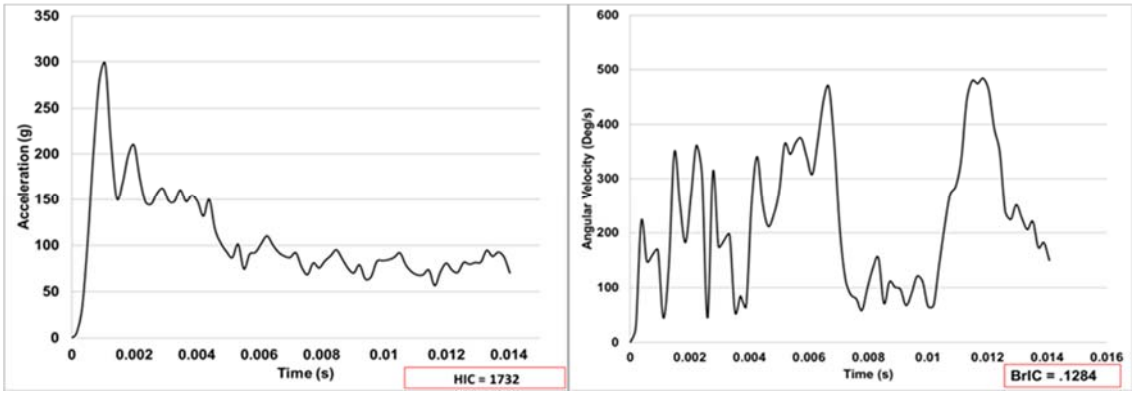

Figure 36. Resultant acceleration and angular velocity graphs for sUAS-human head and neck impact simulation with corresponding HIC and BrIC values

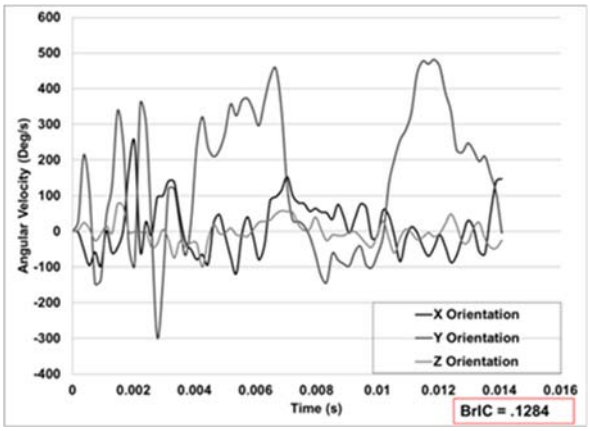

Figure 37. Angular velocity components for sUAS-human head and neck impact simulation with corresponding BrIC value

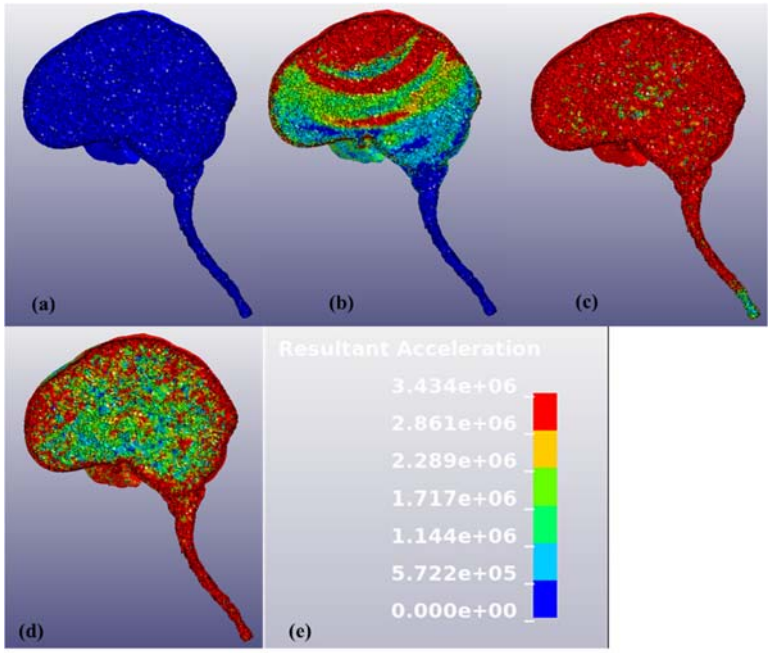

Figure 38. Brain sagittal cut snapshots of FEA acceleration contours at (a) initial impact, (b) after first time step of initial impact, (c) at time step corresponding to peak pressure values, (d) at time step when models start recoiling, and (e) acceleration contour scale (mm/s)

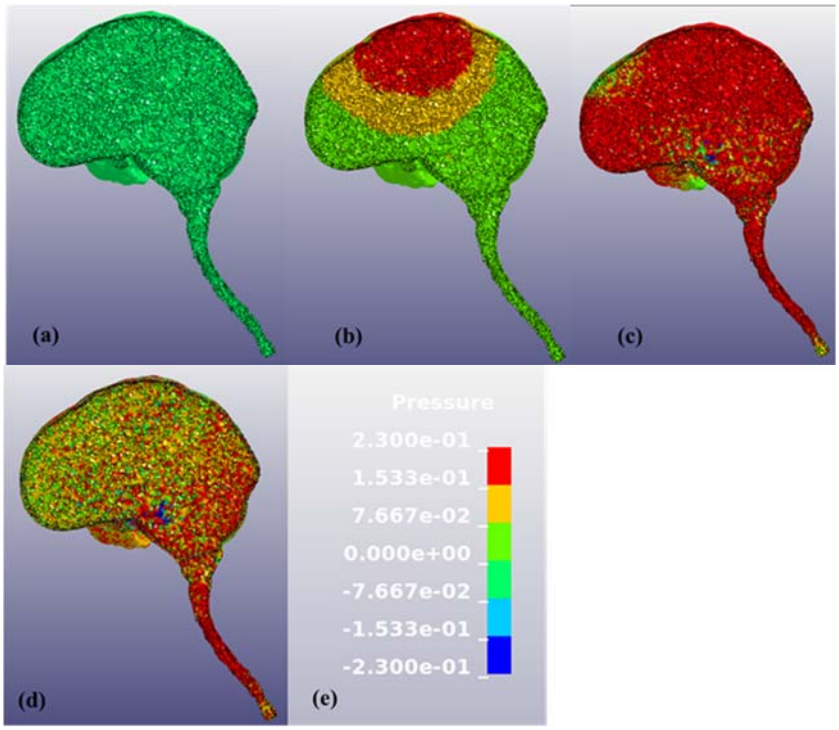

Figure 39. Brain sagittal cut snapshots of FEA pressure contours at (a) initial impact, (b) after first time step of initial impact, (c) at time step corresponding to peak pressure values, (d) at time step when models start recoiling, and (e) pressure contour scale (MPa)

3.7 PMHS-Top-65 fps-90°-Subject 2

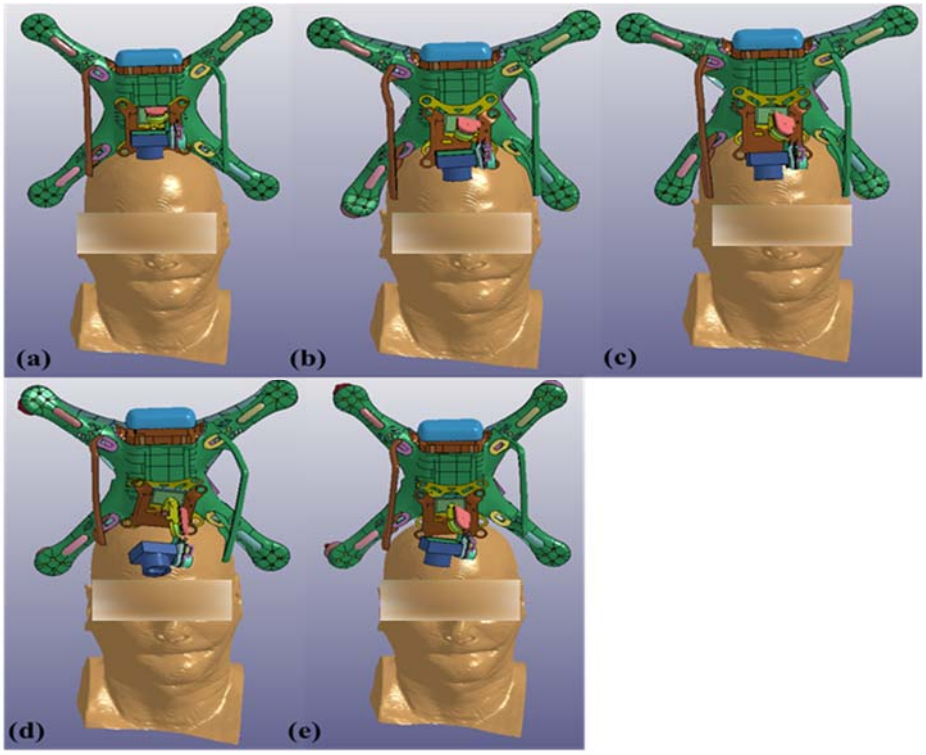

Figure 40. FE simulation snapshots of sUAS impact to human head and neck model at (a) initial contact, (b) after first time step, (c) after second time step, (d) after third time step, and (d) final time step before disassociation between models

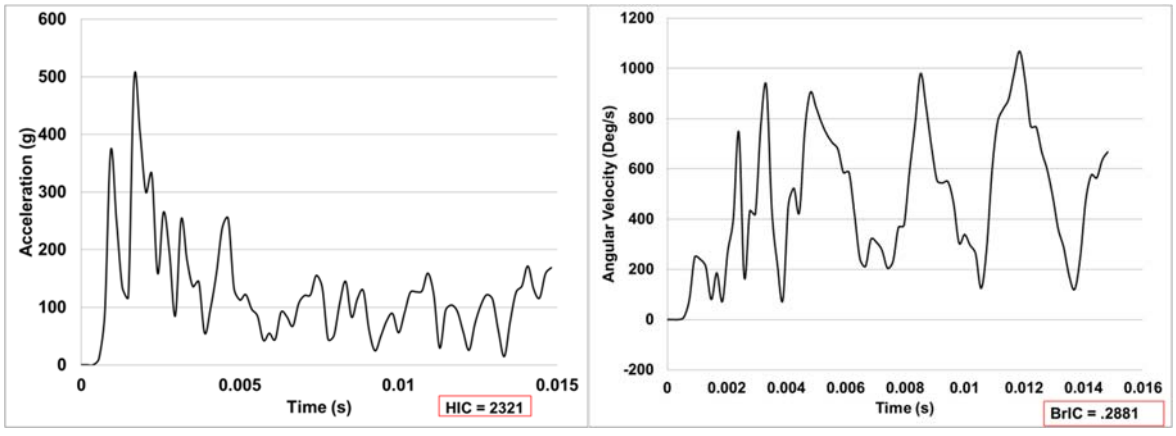

Figure 41. Resultant acceleration and angular velocity graphs for sUAS-human head and neck impact simulation with corresponding HIC and BrIC values

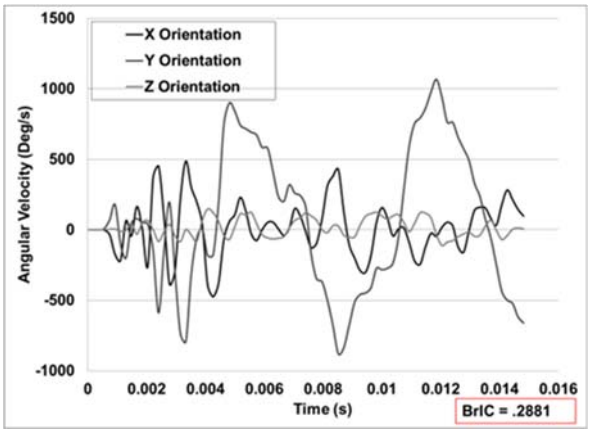

Figure 42. Angular velocity components for sUAS-human head and neck impact simulation with corresponding BrIC value

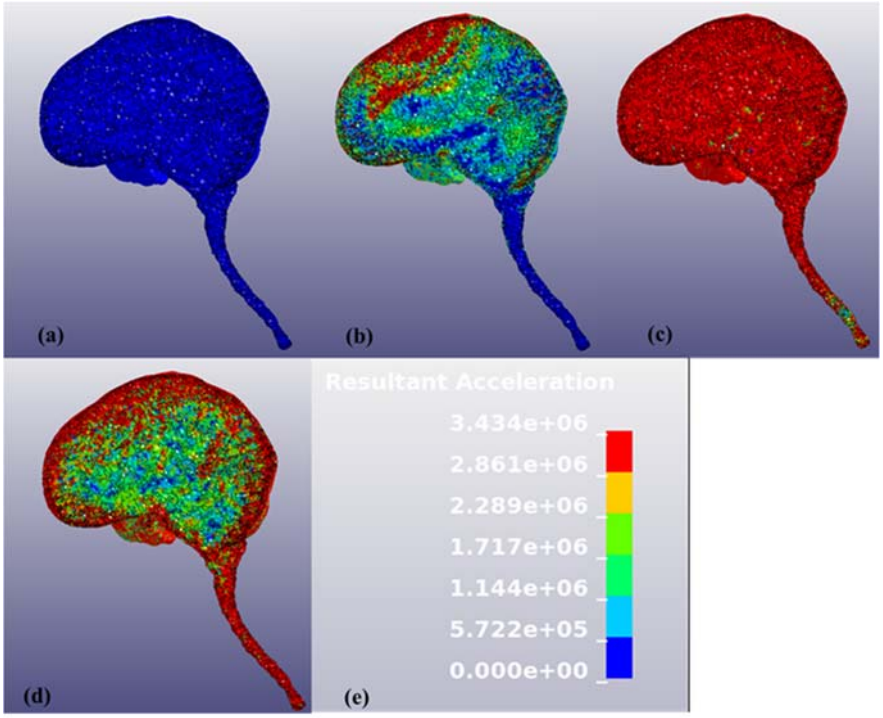

Figure 43. Brain sagittal cut snapshots of FEA acceleration contours at (a) initial impact, (b) after first time step of initial impact, (c) at time step corresponding to peak pressure values, (d) at time step when models start recoiling, and (e) acceleration contour scale (mm/s)

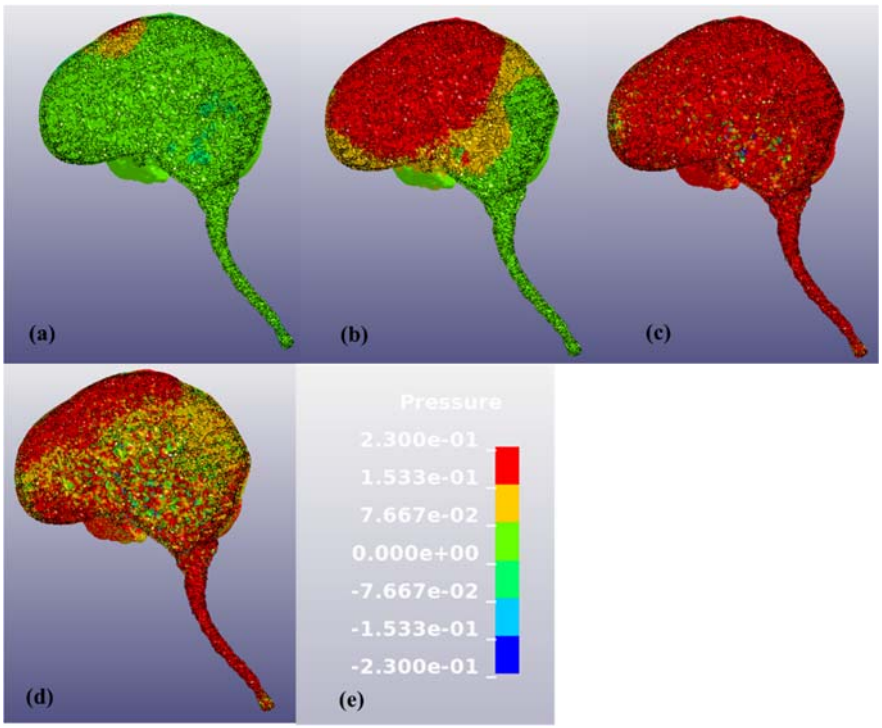

Figure 44. Brain sagittal cut snapshots of FEA pressure contours at (a) initial impact, (b) after first time step of initial impact, (c) at time step corresponding to peak pressure values, (d) at time step when models start recoiling, and (e) pressure contour scale (MPa)

3.8 PMHS-Frontal-61 fps-58°-Subject 2

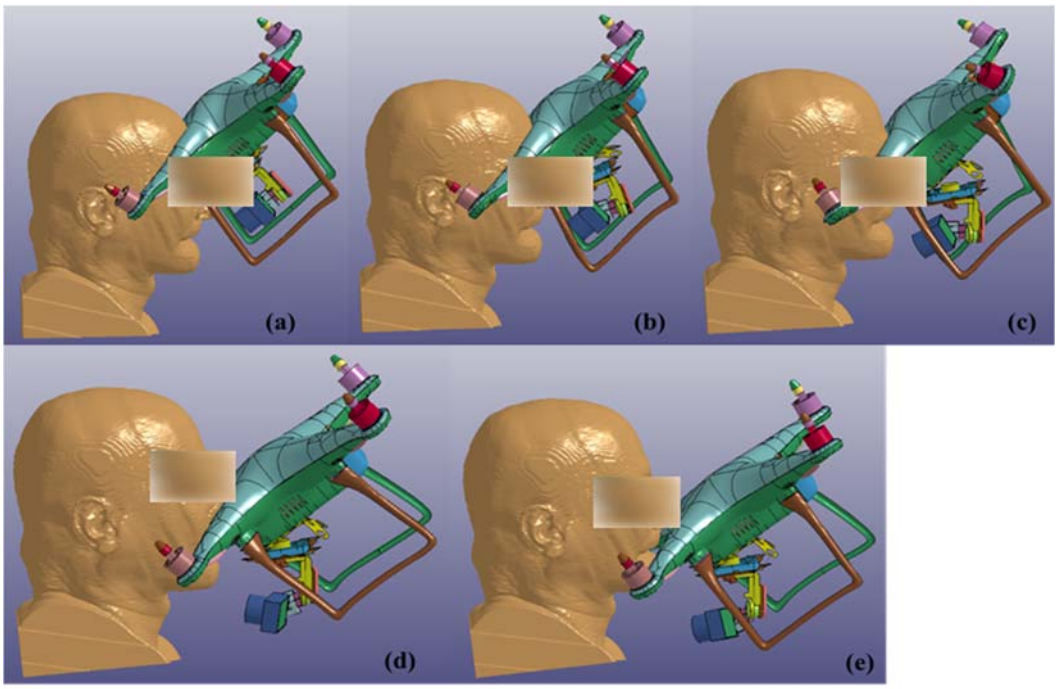

Figure 45. FE simulation snapshots of sUAS impact to human head and neck model at (a) initial contact, (b) after first time step, (c) after second time step, (d) after third time step, and (d) final time step before disassociation between models

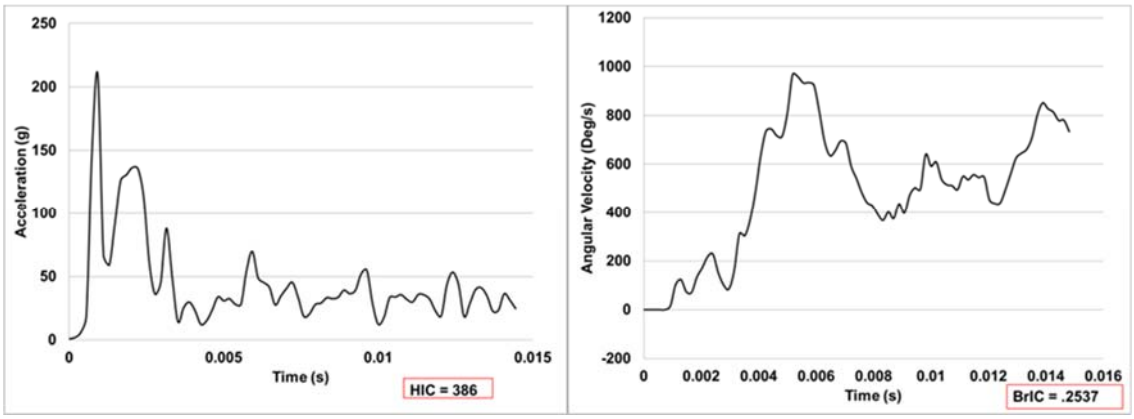

Figure 46. Resultant acceleration and angular velocity graphs for sUAS-human head and neck impact simulation with corresponding HIC and BrIC values

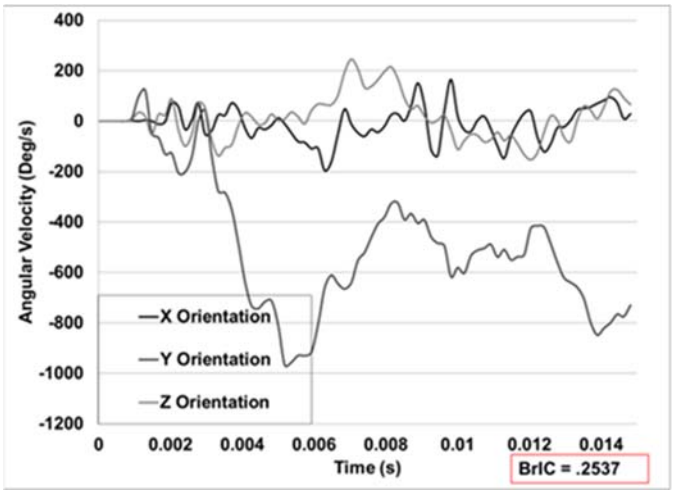

Figure 47. Angular velocity components for sUAS-human head and neck impact simulation with corresponding BrIC value

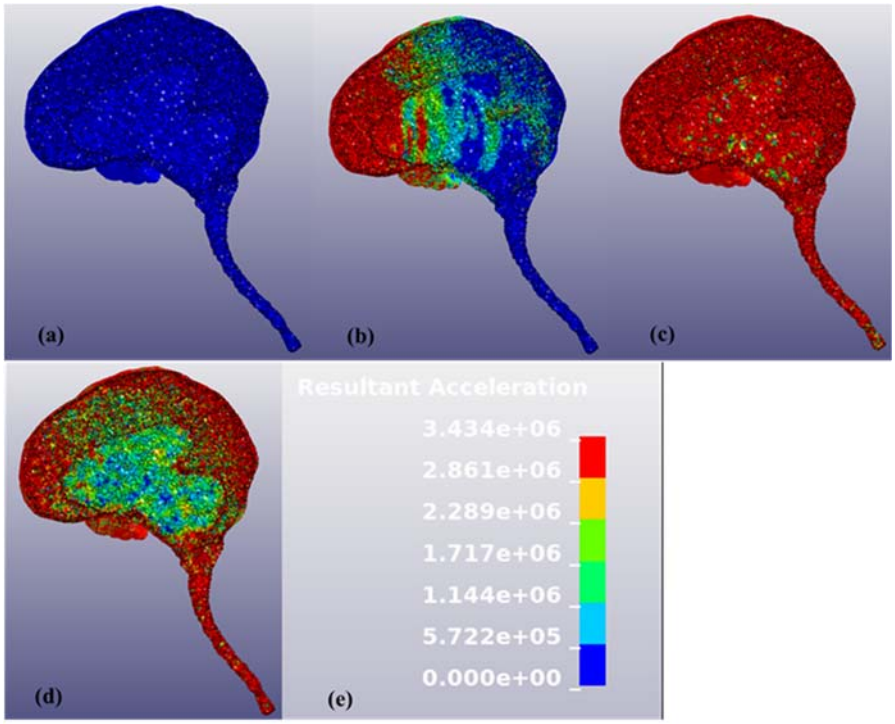

Figure 48. Brain sagittal cut snapshots of FEA acceleration contours at (a) initial impact, (b) after first time step of initial impact, (c) at time step corresponding to peak pressure values, (d) at time step when models start recoiling, and (e) acceleration contour scale (mm/s)

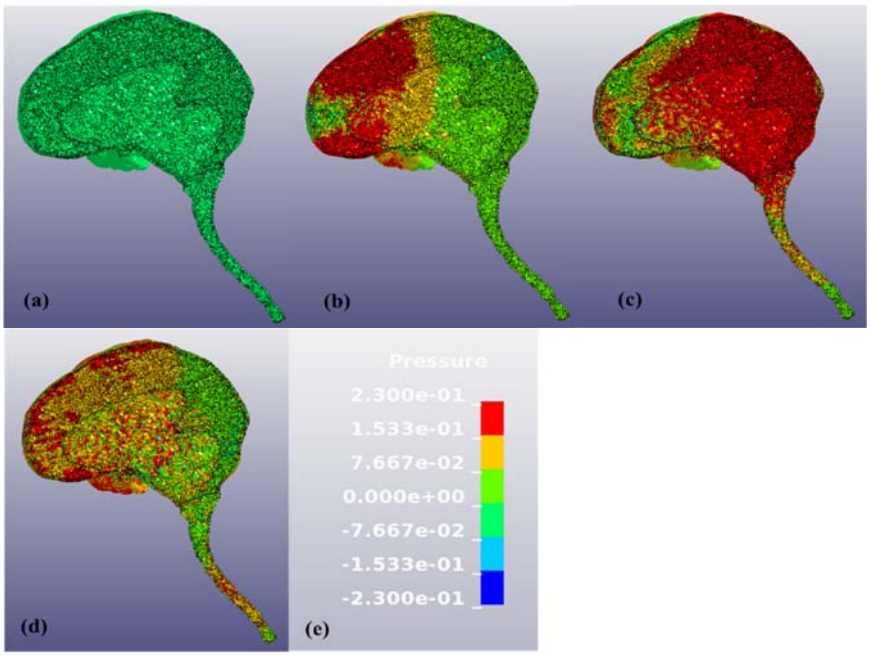

Figure 49. Brain sagittal cut snapshots of FEA pressure contours at (a) initial impact, (b) after first time step of initial impact, (c) at time step corresponding to peak pressure values, (d) at time step when models start recoiling, and (e) pressure contour scale (MPa)

3.9 PMHS-Frontal-71 fps-58°-Subject 2

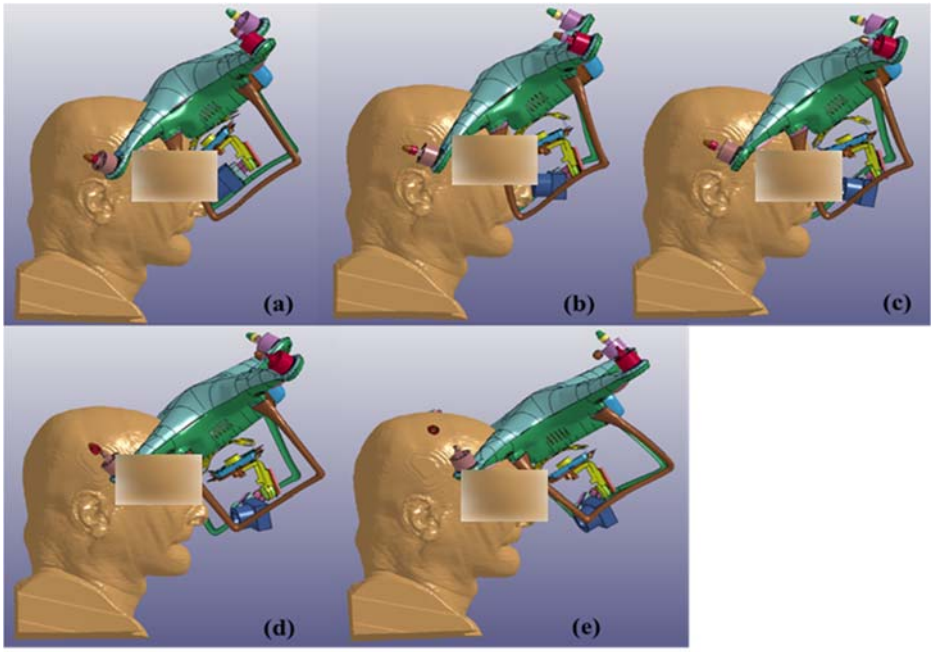

Figure 50. FE simulation snapshots of sUAS impact to human head and neck model at (a) initial contact, (b) after first time step, (c) after second time step, (d) after third time step, and (d) final time step before disassociation between models

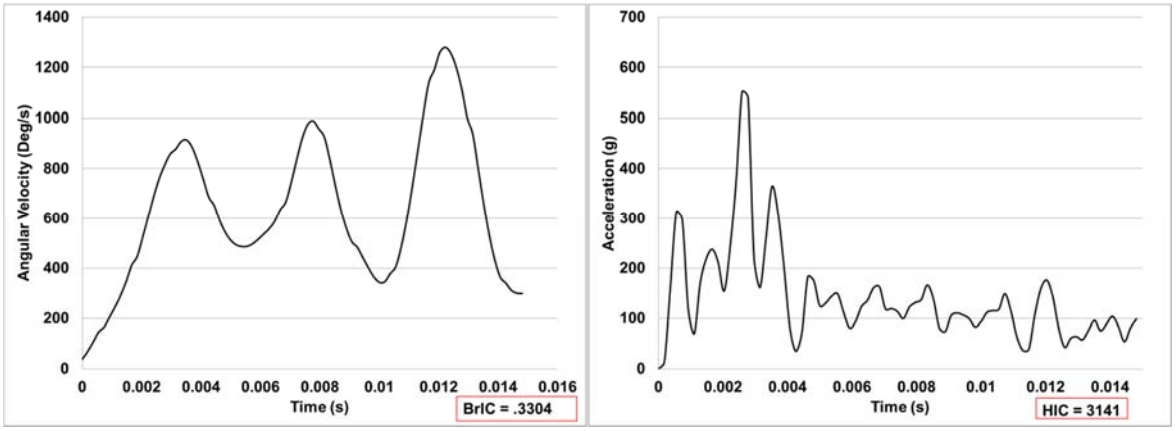

Figure 51. Resultant acceleration and angular velocity graphs for sUAS-human head and neck impact simulation with corresponding HIC and BrIC values

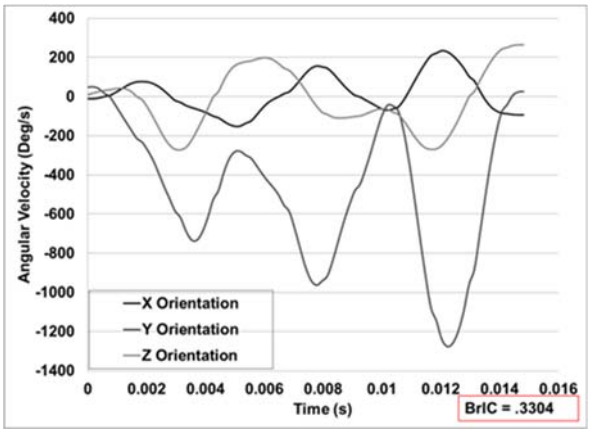

Figure 52. Angular velocity components for sUAS-human head and neck impact simulation with corresponding BrIC value

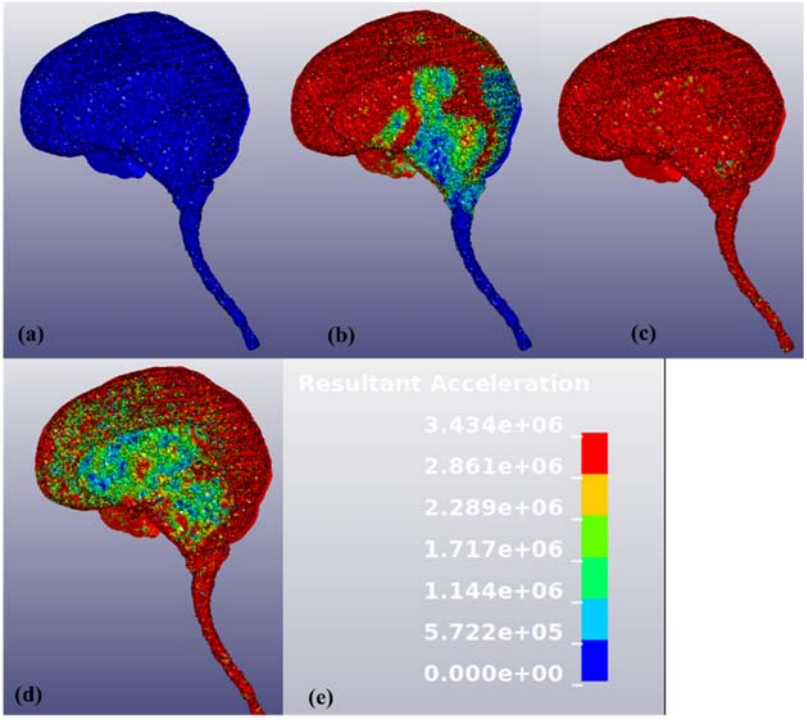

Figure 53. Brain sagittal cut snapshots of FEA acceleration contours at (a) initial impact, (b) after first time step of initial impact, (c) at time step corresponding to peak pressure values, (d) at time step when models start recoiling, and (e) acceleration contour scale (mm/s)

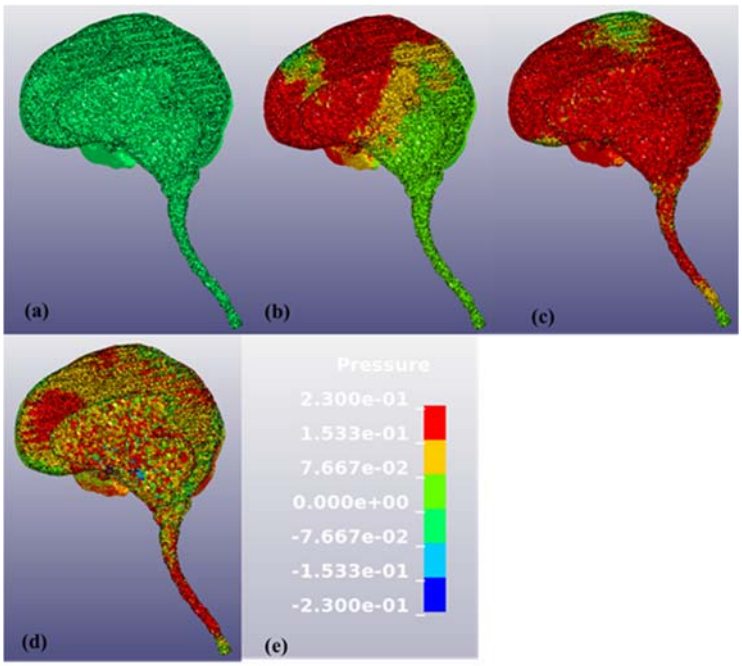

Figure 54. Brain sagittal cut snapshots of FEA pressure contours at (a) initial impact, (b) after first time step of initial impact, (c) at time step corresponding to peak pressure values, (d) at time step when models start recoiling, and (e) pressure contour scale (MPa)

3.10 PMHS-Side-61 fps-58°-Subject 2

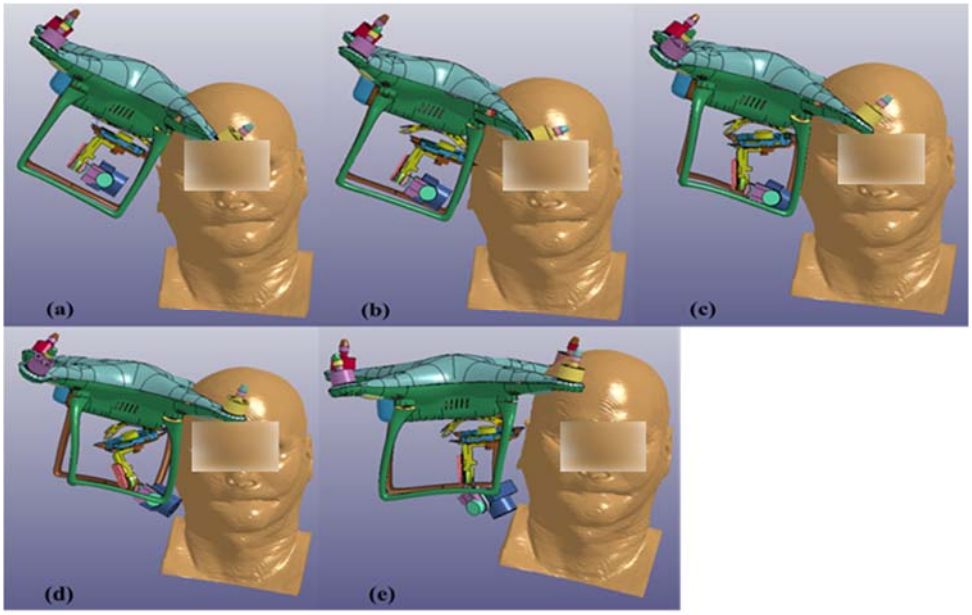

Figure 55. FE simulation snapshots of sUAS impact to human head and neck model at (a) initial contact, (b) after first time step, (c) after second time step, (d) after third time step, and (d) final time step before disassociation between models

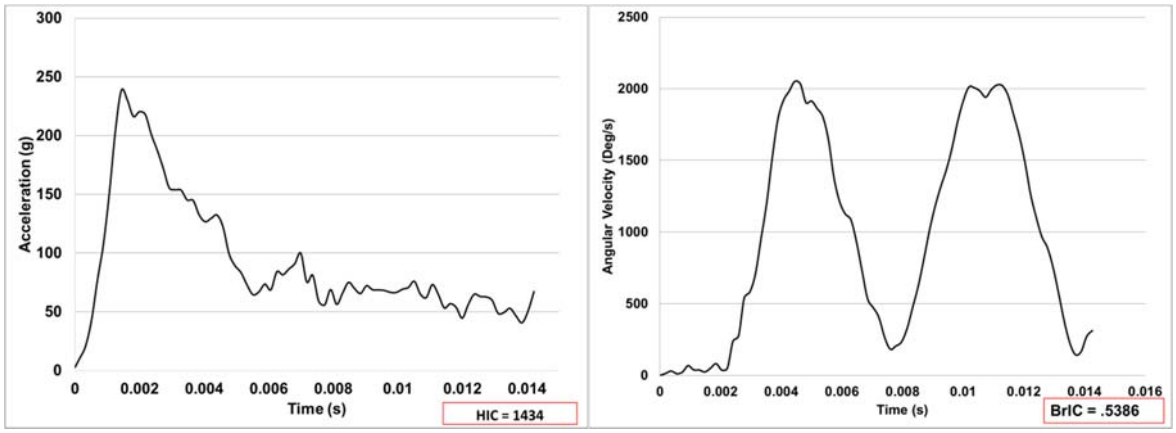

Figure 56. Resultant acceleration and angular velocity graphs for sUAS-human head and neck impact simulation with corresponding HIC and BrIC values

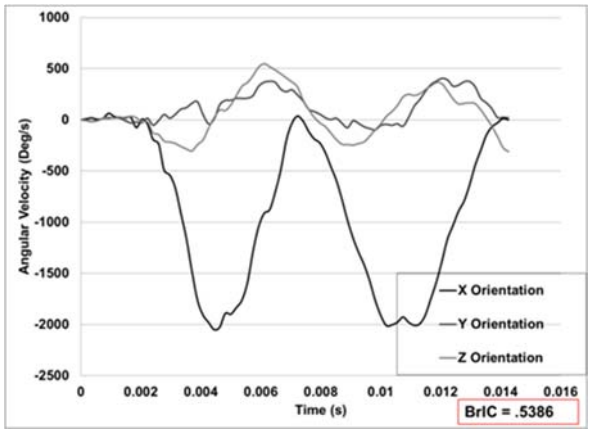

Figure 57. Angular velocity components for sUAS-human head and neck impact simulation with corresponding BrIC value

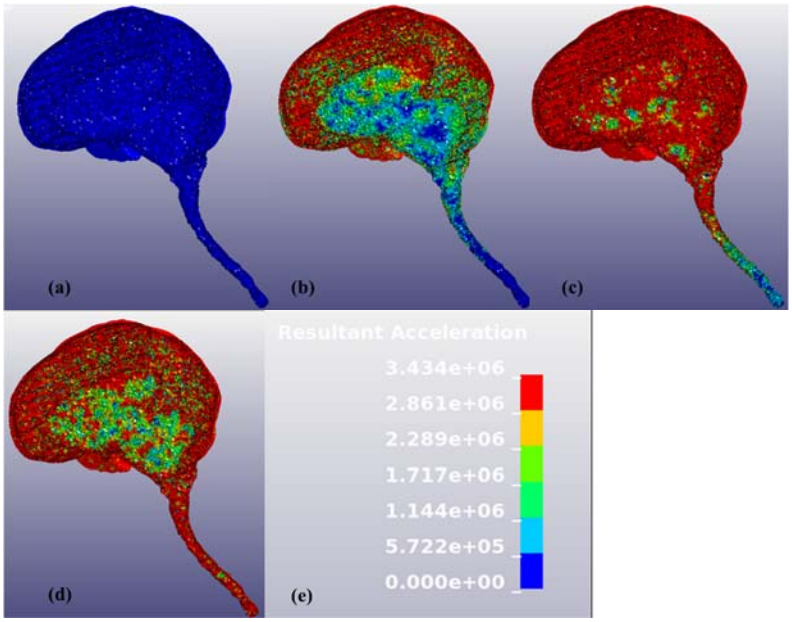

Figure 58. Brain sagittal cut snapshots of FEA acceleration contours at (a) initial impact, (b) after first time step of initial impact, (c) at time step corresponding to peak pressure values, (d) at time step when models start recoiling, and (e) acceleration contour scale (mm/s)

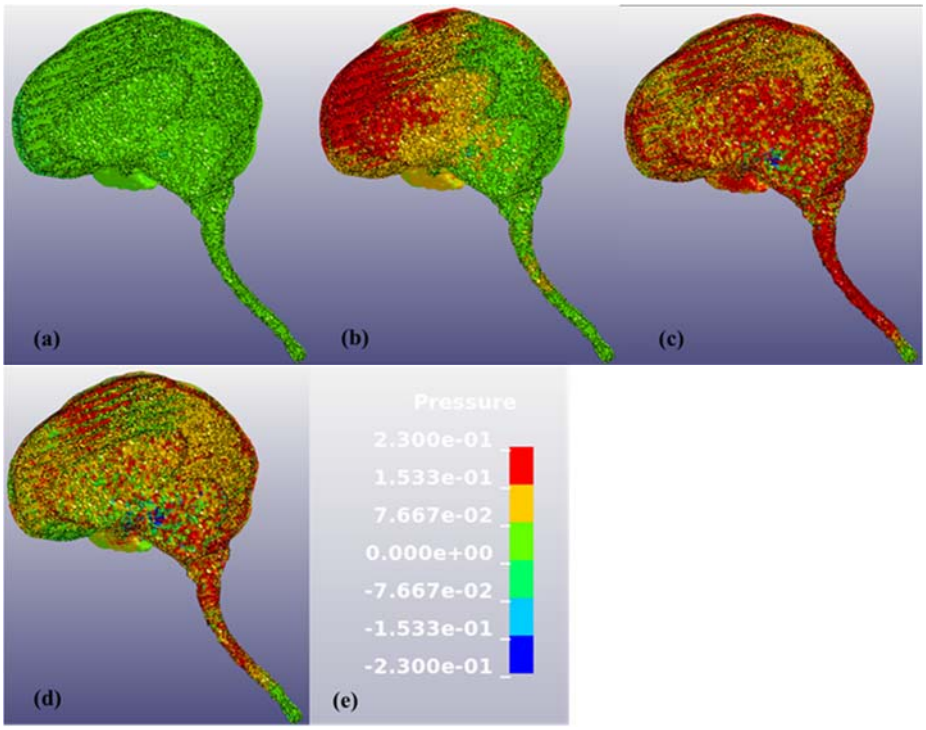

Figure 59. Brain sagittal cut snapshots of FEA pressure contours at (a) initial impact, (b) after first time step of initial impact, (c) at time step corresponding to peak pressure values, (d) at time step when models start recoiling, and (e) pressure contour scale (MPa)

3.11 PMHS-Side-61 fps-58°-Subject 3

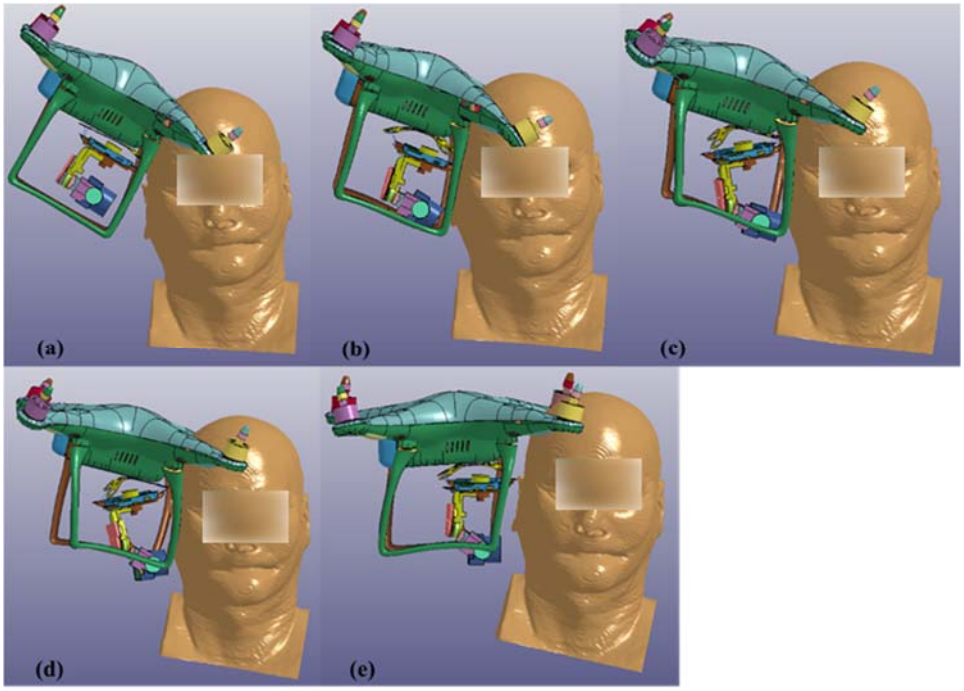

Figure 60. FE simulation snapshots of sUAS impact to human head and neck model at (a) initial contact, (b) after first time step, (c) after second time step, (d) after third time step, and (d) final time step before disassociation between models

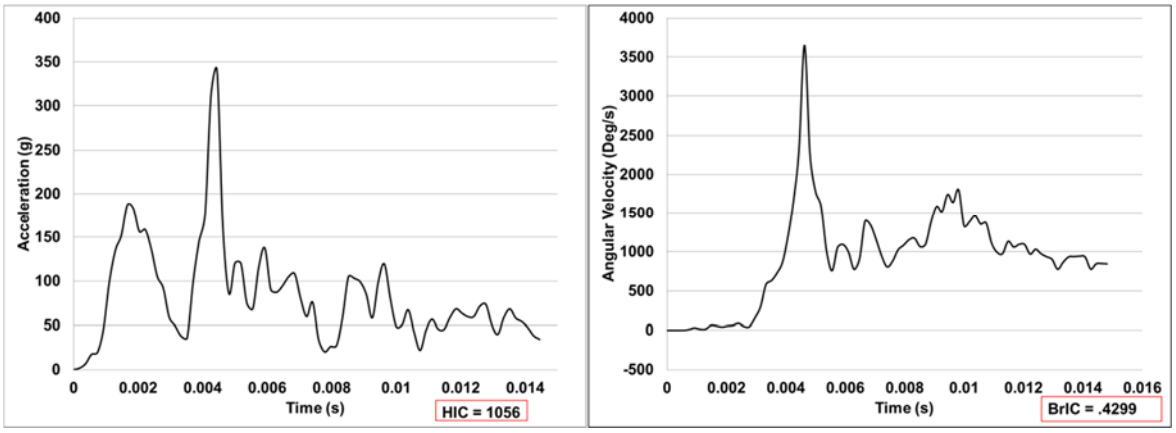

Figure 61. Resultant acceleration and angular velocity graphs for sUAS-human head and neck impact simulation with corresponding HIC and BrIC values

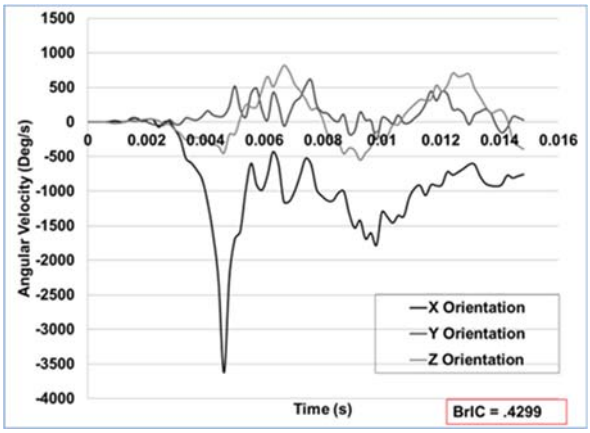

Figure 62. Angular velocity components for sUAS-human head and neck impact simulation with corresponding BrIC value

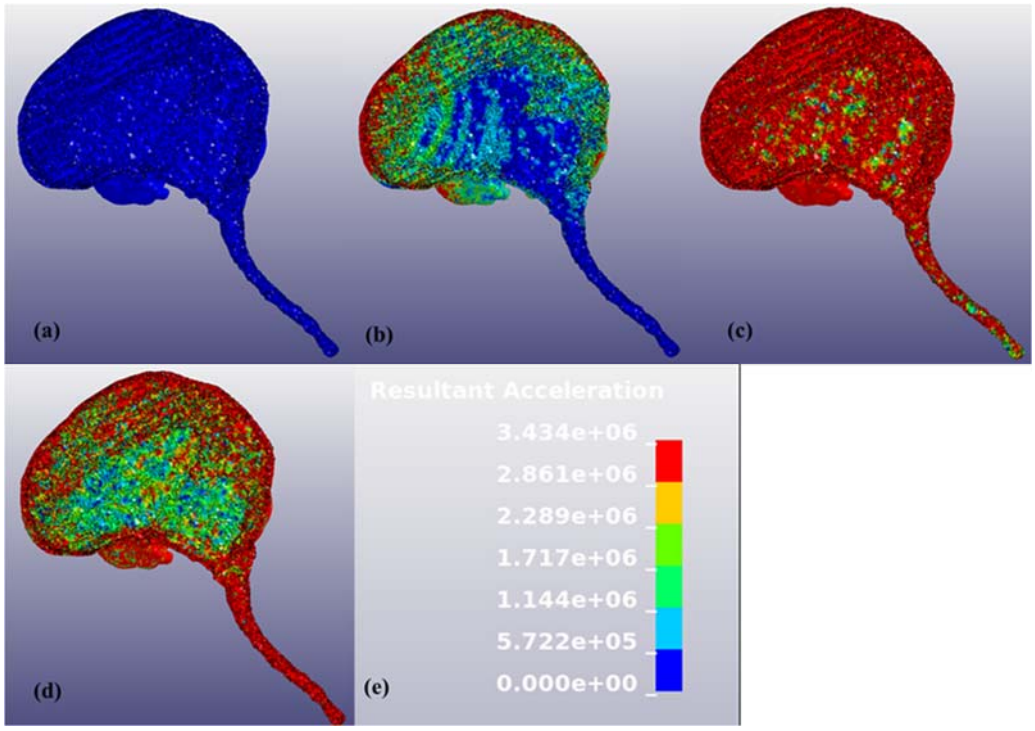

Figure 63. Brain sagittal cut snapshots of FEA acceleration contours at (a) initial impact, (b) after first time step of initial impact, (c) at time step corresponding to peak pressure values, (d) at time step when models start recoiling, and (e) acceleration contour scale (mm/s)

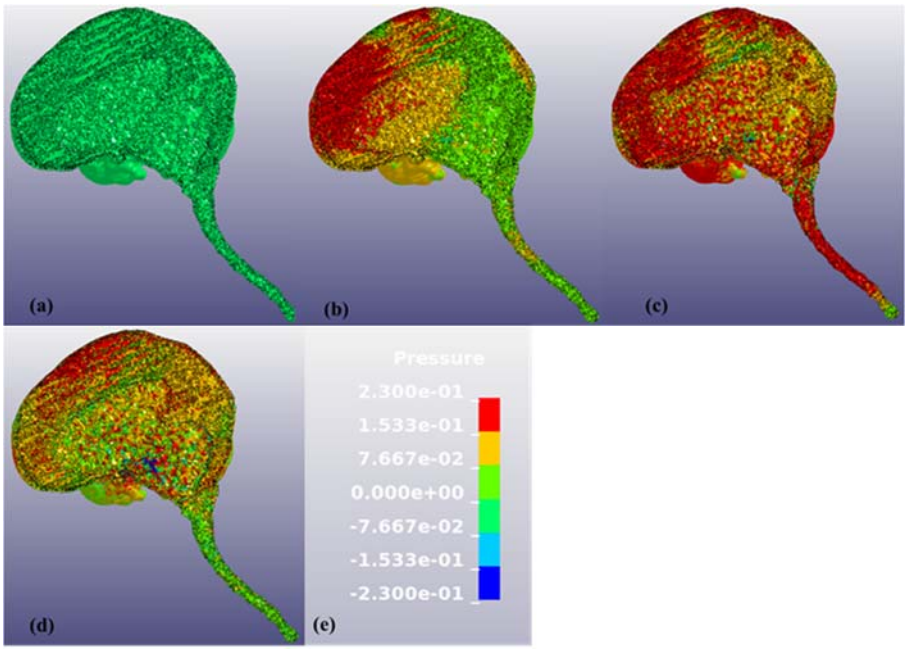

Figure 64. Brain sagittal cut snapshots of FEA pressure contours at (a) initial impact, (b) after first time step of initial impact, (c) at time step corresponding to peak pressure values, (d) at time step when models start recoiling, and (e) pressure contour scale (MPa)

3.12 PMHS-Side-71 fps-58°-Subject 3

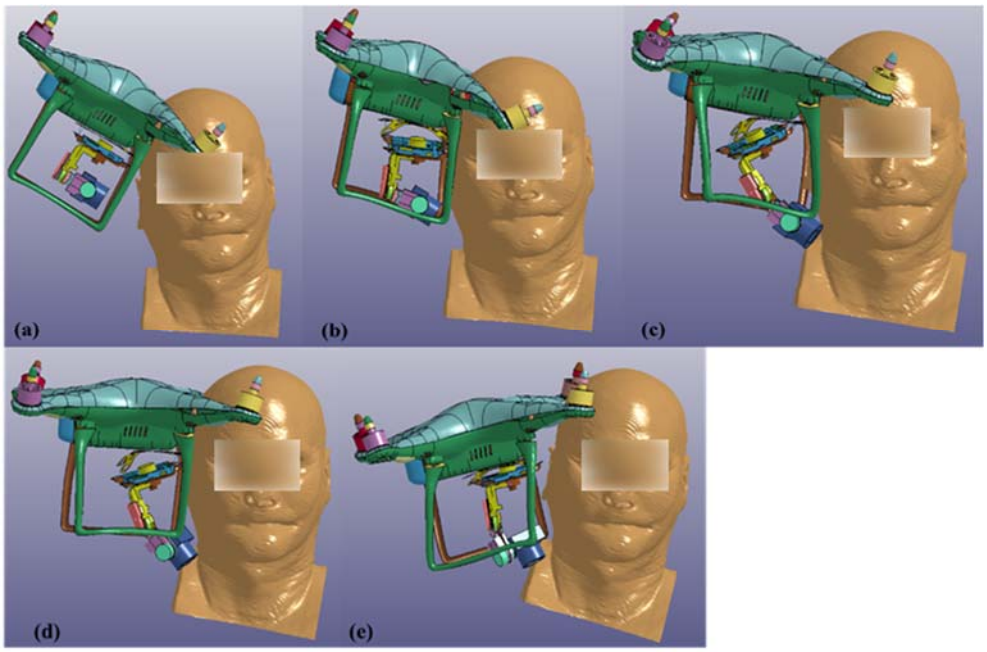

Figure 65. FE simulation snapshots of sUAS impact to human head and neck model at (a) initial contact, (b) after first time step, (c) after second time step, (d) after third time step, and (d) final time step before disassociation between models

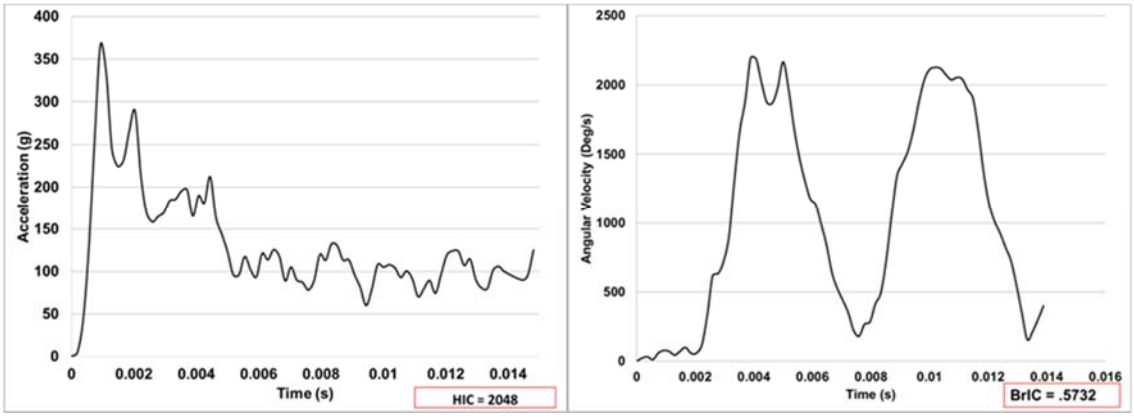

Figure 66. Resultant acceleration and angular velocity graphs for sUAS-human head and neck impact simulation with corresponding HIC and BrIC values

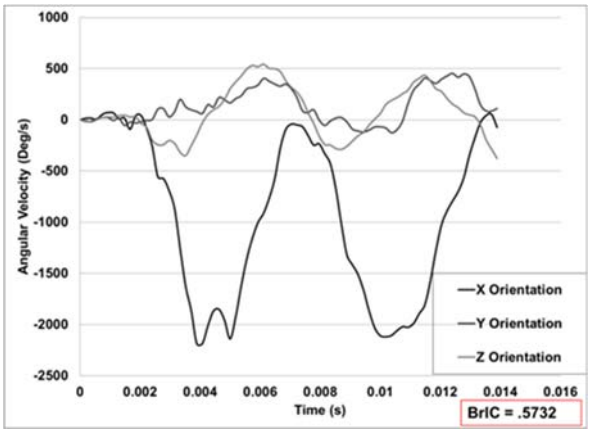

Figure 67. Angular velocity components for sUAS-human head and neck impact simulation with corresponding BrIC value

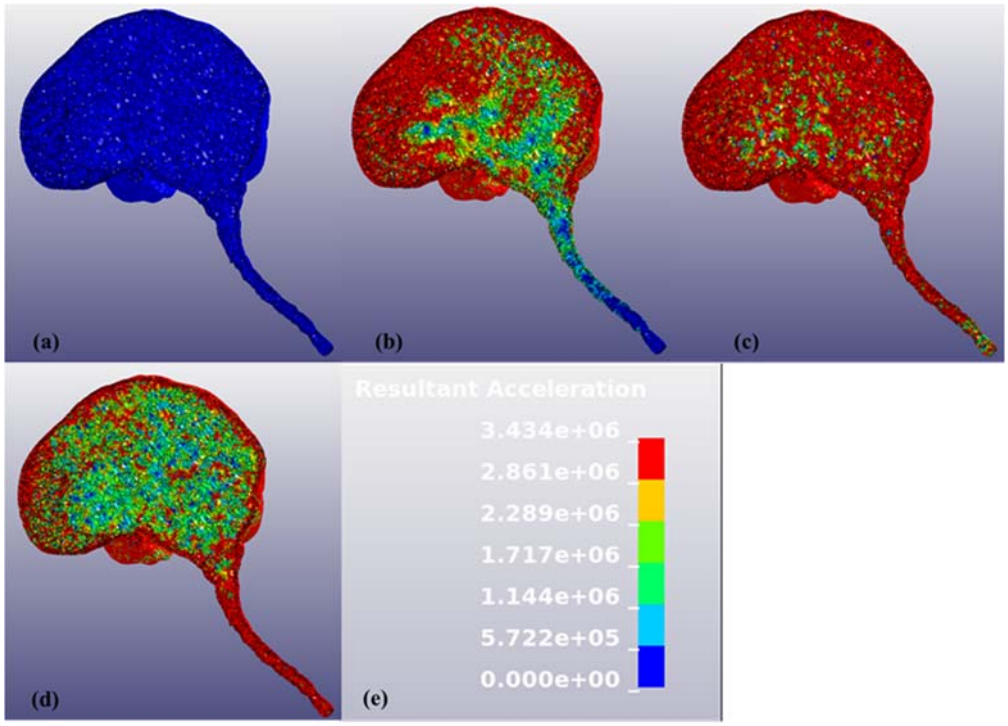

Figure 68. Brain sagittal cut snapshots of FEA acceleration contours at (a) initial impact, (b) after first time step of initial impact, (c) at time step corresponding to peak pressure values, (d) at time step when models start recoiling, and (e) acceleration contour scale (mm/s)

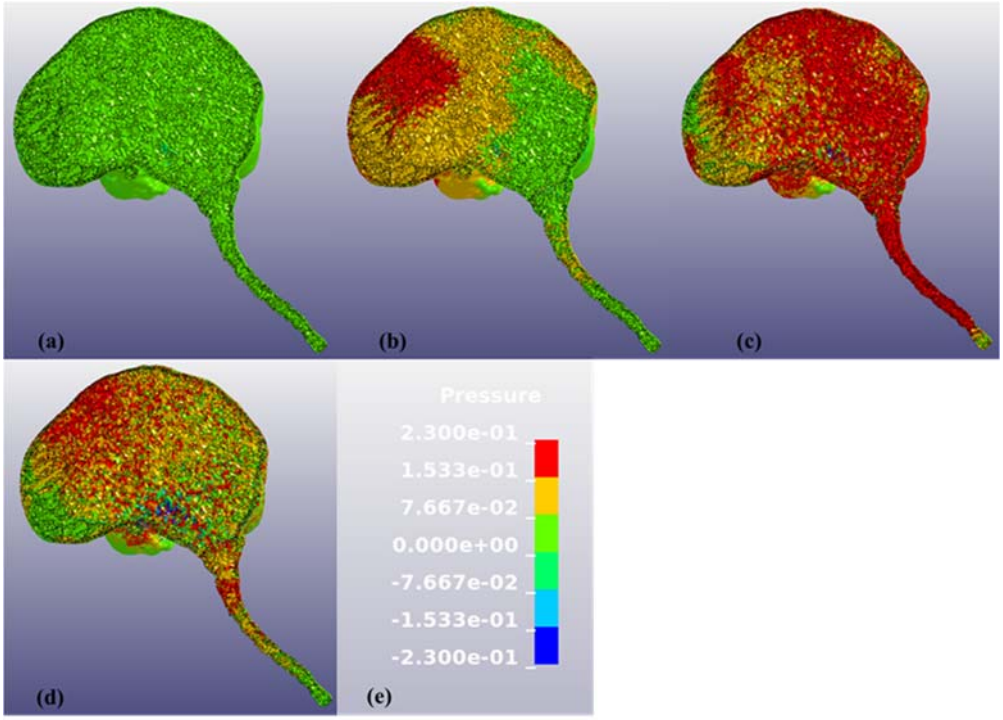

Figure 69. Brain sagittal cut snapshots of FEA pressure contours at (a) initial impact, (b) after first time step of initial impact, (c) at time step corresponding to peak pressure values, (d) at time step when models start recoiling, and (e) pressure contour scale (MPa)

3.13 PMHS-Frontal-71 fps-58°-Subject 3

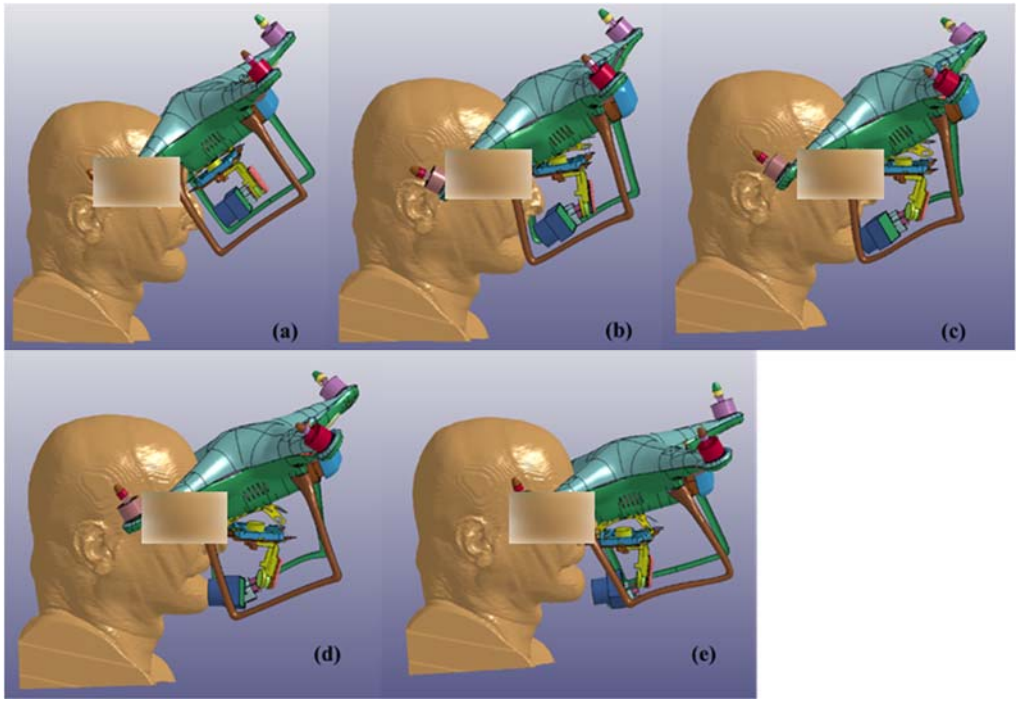

Figure 70. FE simulation snapshots of sUAS impact to human head and neck model at (a) initial contact, (b) after first time step, (c) after second time step, (d) after third time step, and (d) final time step before disassociation between models

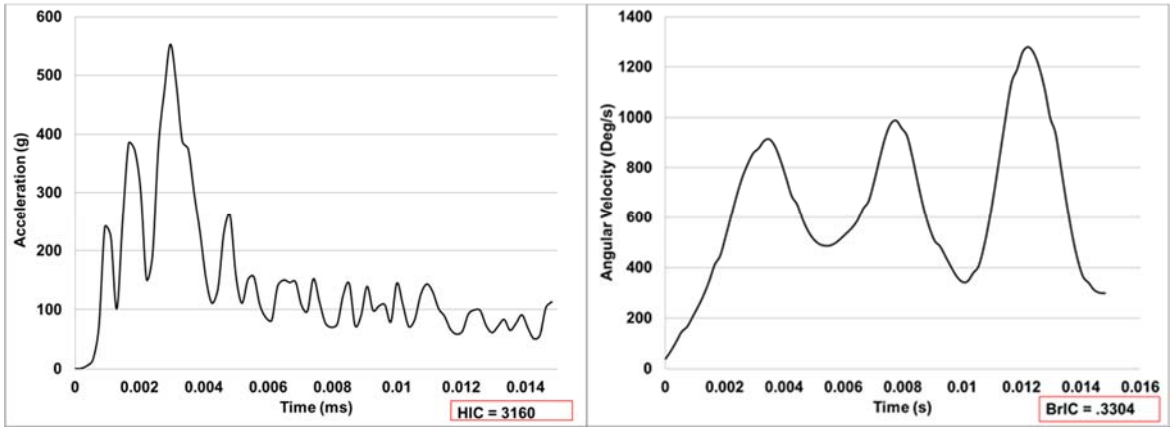

Figure 71. Resultant acceleration and angular velocity graphs for sUAS-human head and neck impact simulation with corresponding HIC and BrIC values

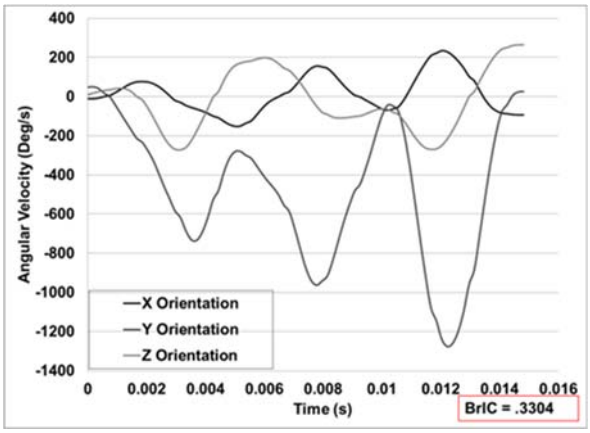

Figure 72. Angular velocity components for sUAS-human head and neck impact simulation with corresponding BrIC value

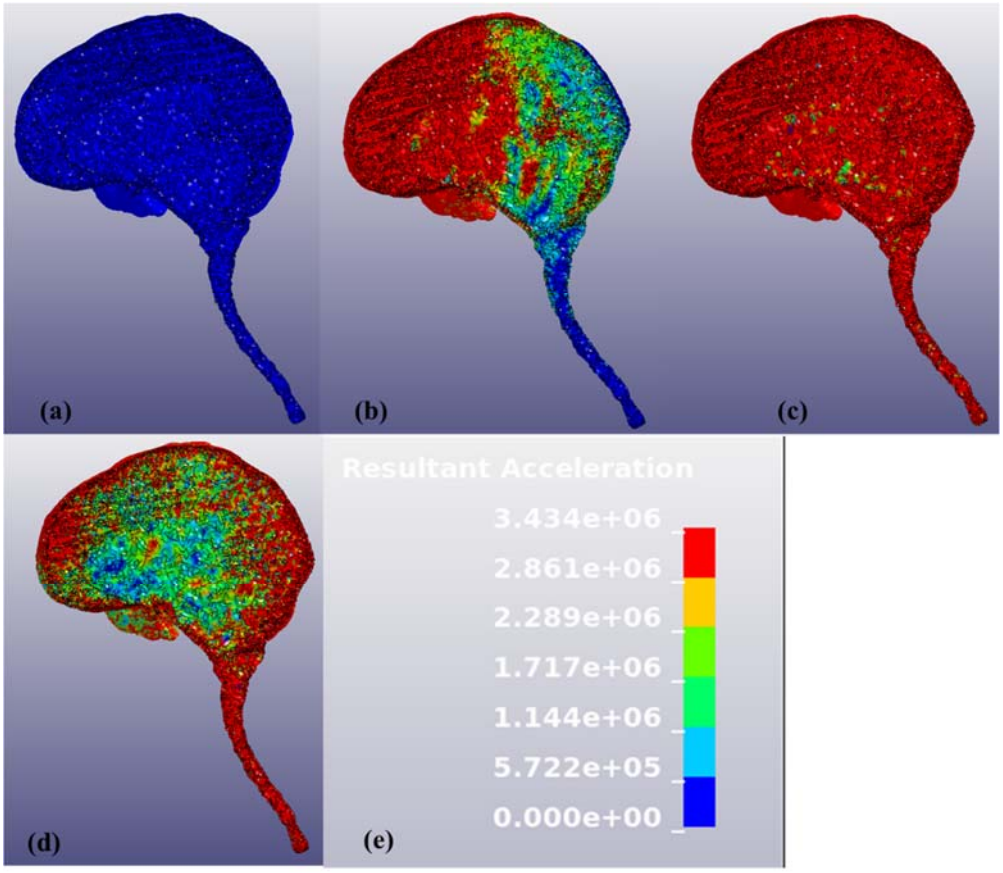

Figure 73. Brain sagittal cut snapshots of FEA acceleration contours at (a) initial impact, (b) after first time step of initial impact, (c) at time step corresponding to peak pressure values, (d) at time step when models start recoiling, and (e) acceleration contour scale (mm/s)

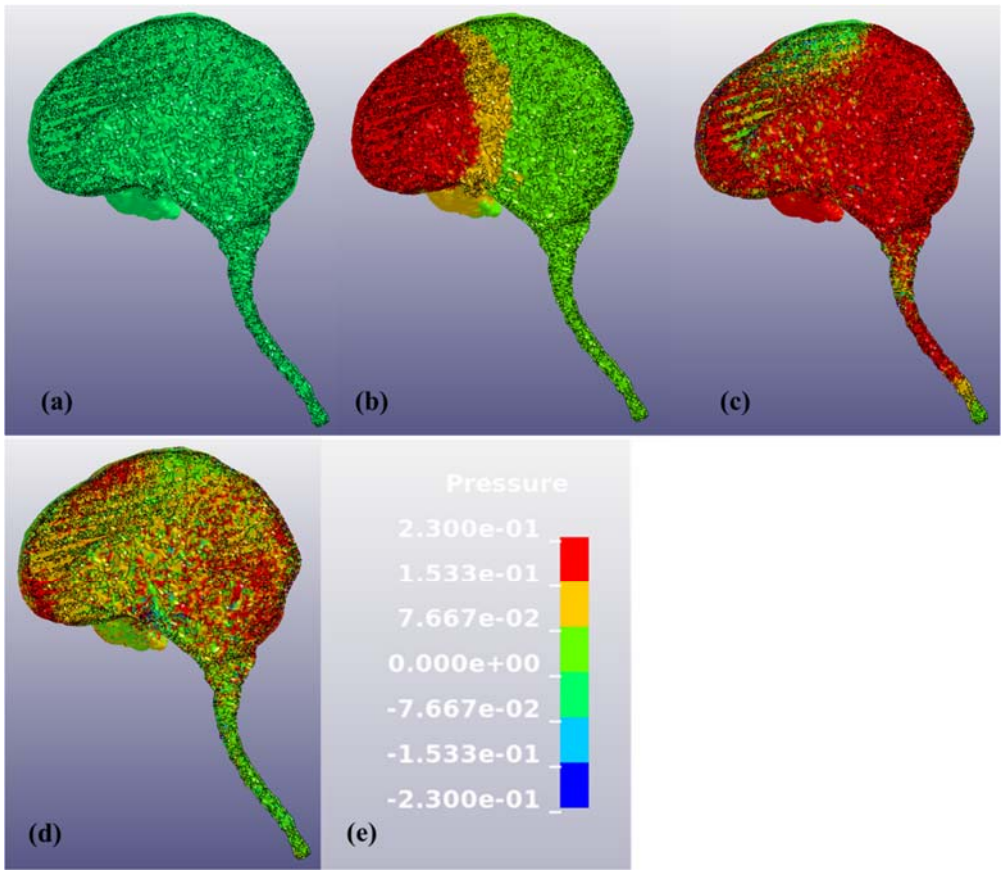

Figure 74. Brain sagittal cut snapshots of FEA pressure contours at (a) initial impact, (b) after first time step of initial impact, (c) at time step corresponding to peak pressure values, (d) at time step when models start recoiling, and (e) pressure contour scale (MPa)

3.14 PMHS-Top-65 fps-90°-Subject 3

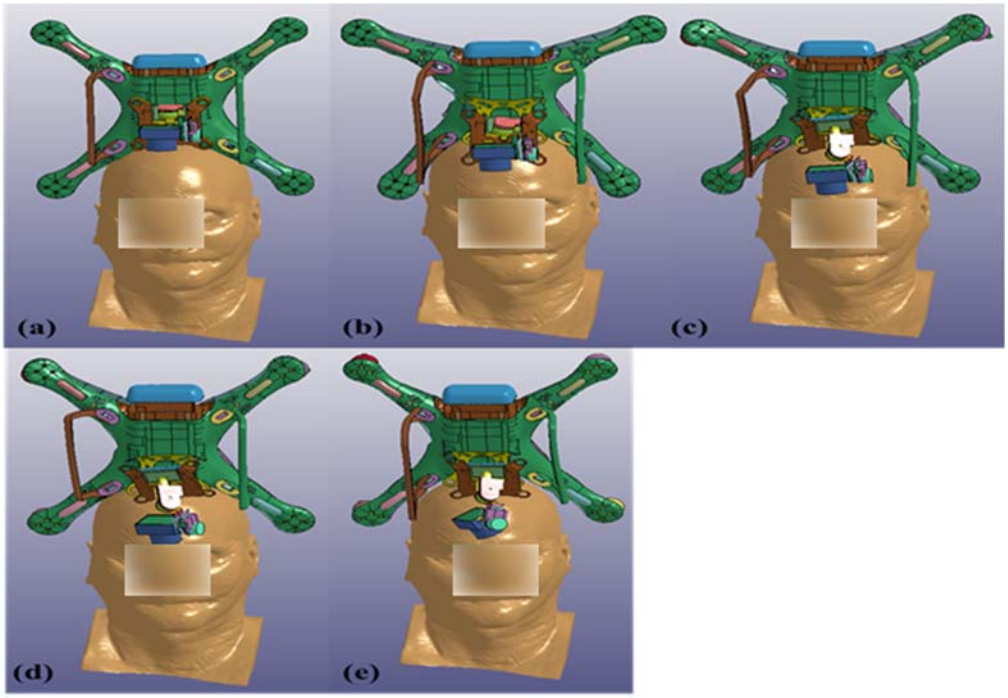

Figure 75. **:** FE simulation snapshots of sUAS impact to human head and neck model at (a) initial contact, (b) after first time step, (c) after second time step, (d) after third time step, and (d) final time step before disassociation between models

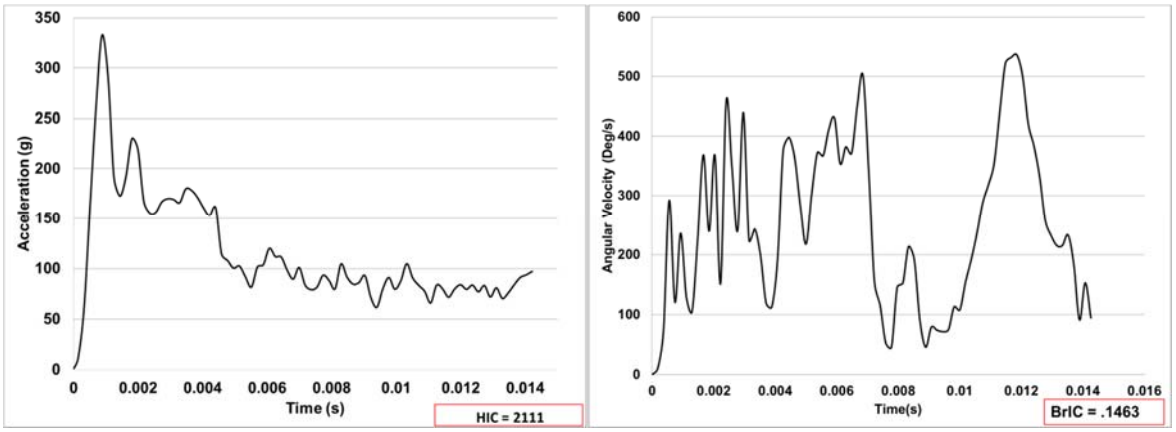

Figure 76. Resultant acceleration and angular velocity graphs for sUAS-human head and neck impact simulation with corresponding HIC and BrIC values

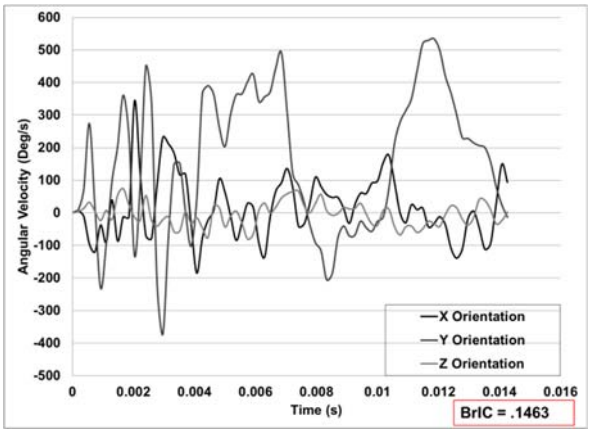

Figure 77. Angular velocity components for sUAS-human head and neck impact simulation with corresponding BrIC value

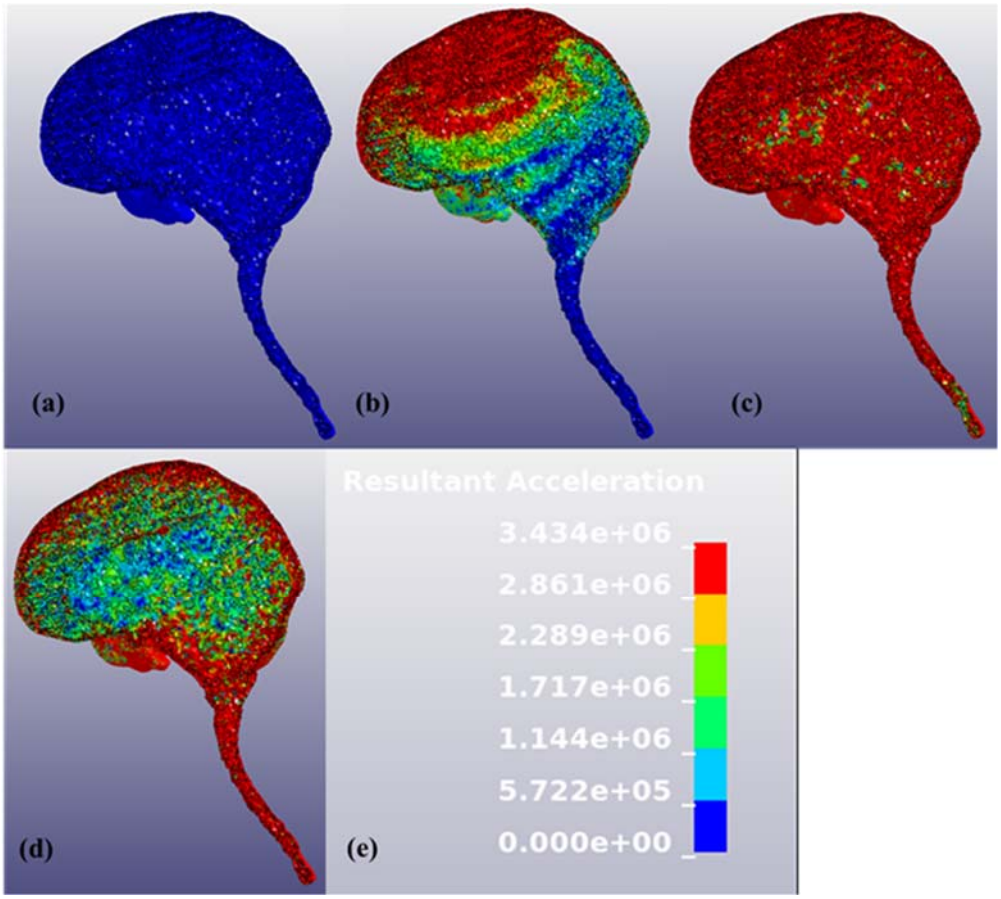

Figure 78. Brain sagittal cut snapshots of FEA acceleration contours at (a) initial impact, (b) after first time step of initial impact, (c) at time step corresponding to peak pressure values, (d) at time step when models start recoiling, and (e) acceleration contour scale (mm/s)

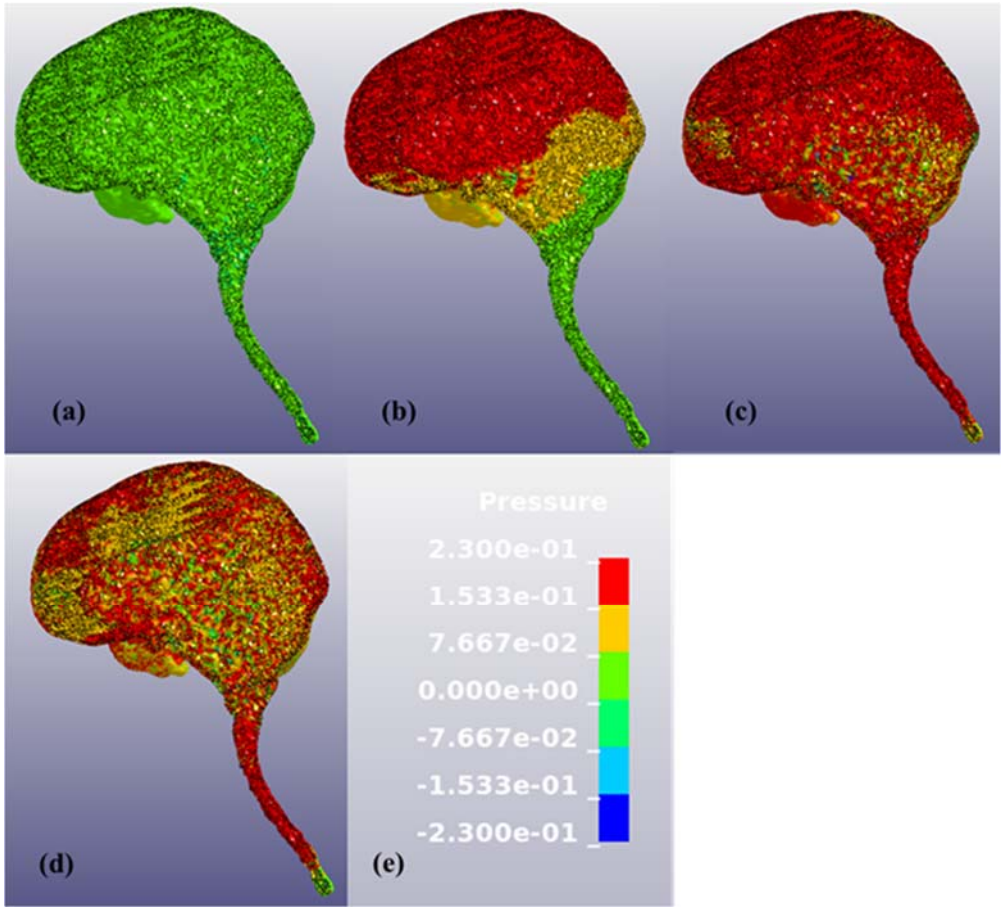

Figure 79. Brain sagittal cut snapshots of FEA pressure contours at (a) initial impact, (b) after first time step of initial impact, (c) at time step corresponding to peak pressure values, (d) at time step when models start recoiling, and (e) pressure contour scale (MPa)

3.15 PMHS-Top-71 fps-90°-Subject 3

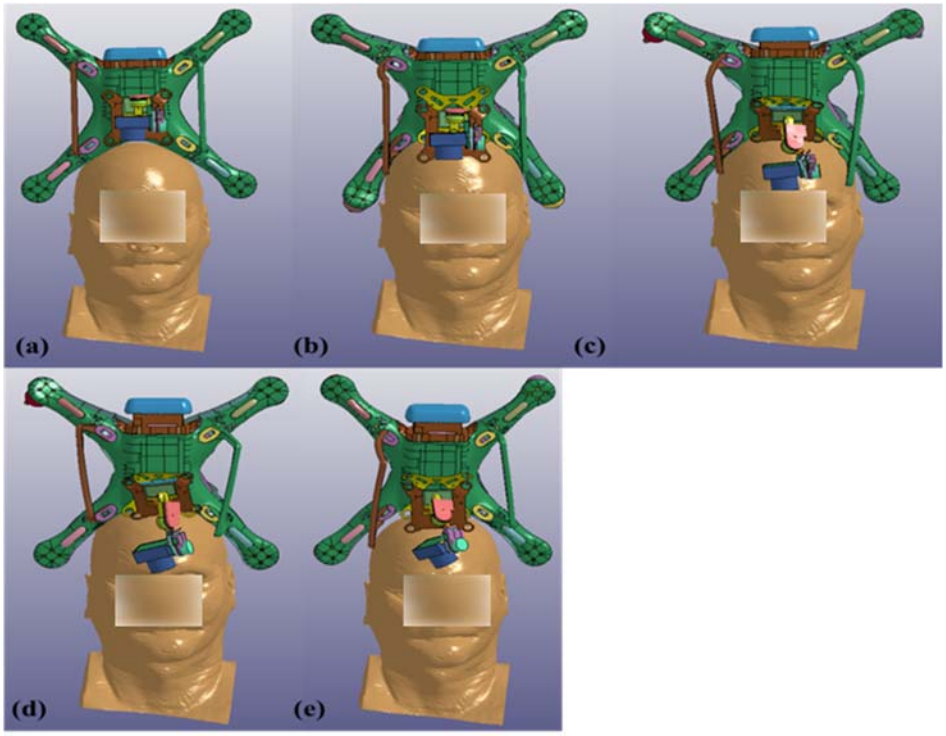

Figure 80. FE simulation snapshots of sUAS impact to human head and neck model at (a) initial contact, (b) after first time step, (c) after second time step, (d) after third time step, and (d) final time step before disassociation between models

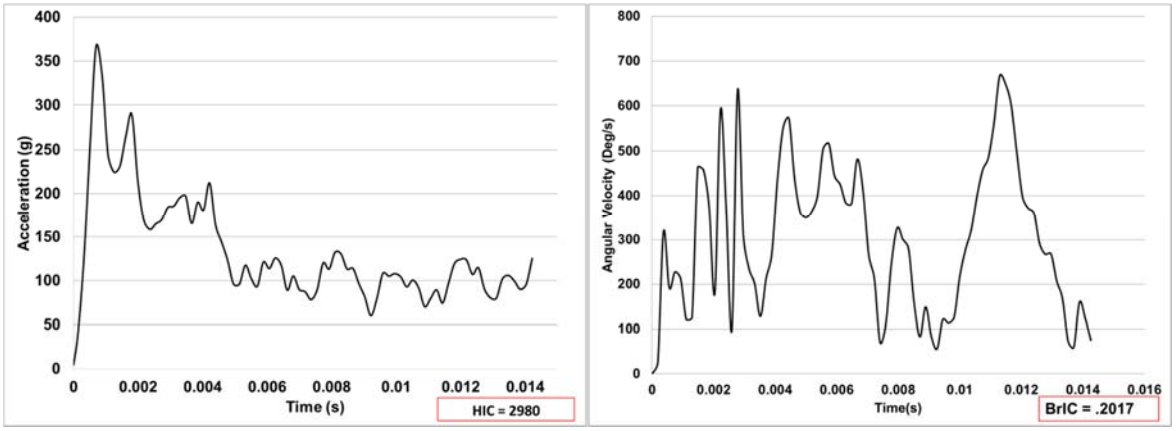

Figure 81. Resultant acceleration and angular velocity graphs for sUAS-human head and neck impact simulation with corresponding HIC and BrIC values

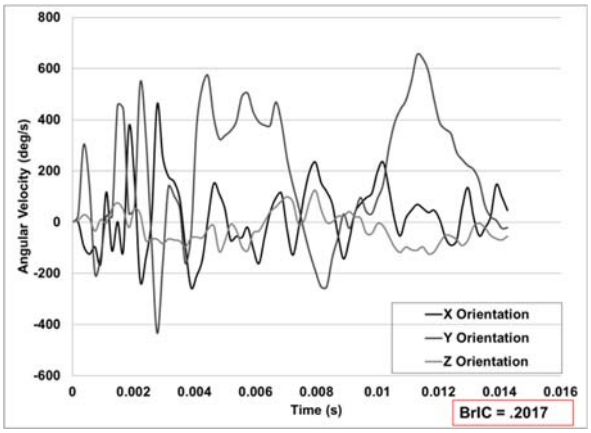

Figure 82. Angular velocity components for sUAS-human head and neck impact simulation with corresponding BrIC value

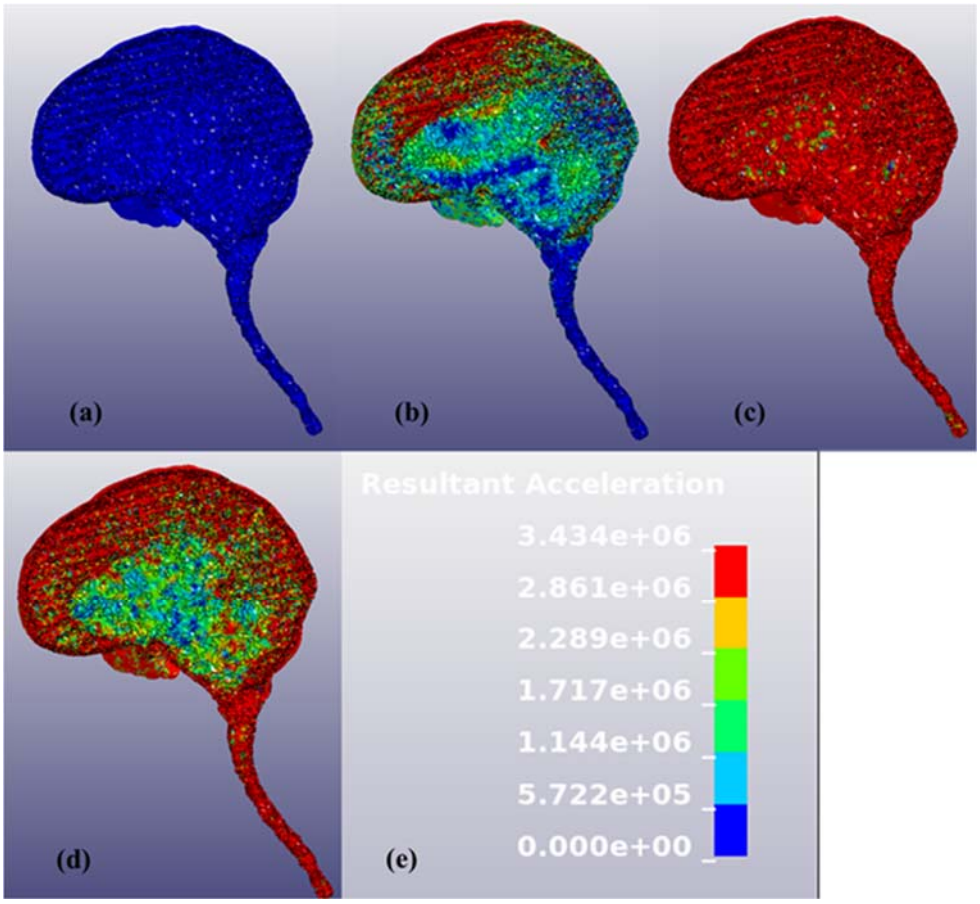

Figure 83. Brain sagittal cut snapshots of FEA acceleration contours at (a) initial impact, (b) after first time step of initial impact, (c) at time step corresponding to peak pressure values, (d) at time step when models start recoiling, and (e) acceleration contour scale (mm/s)

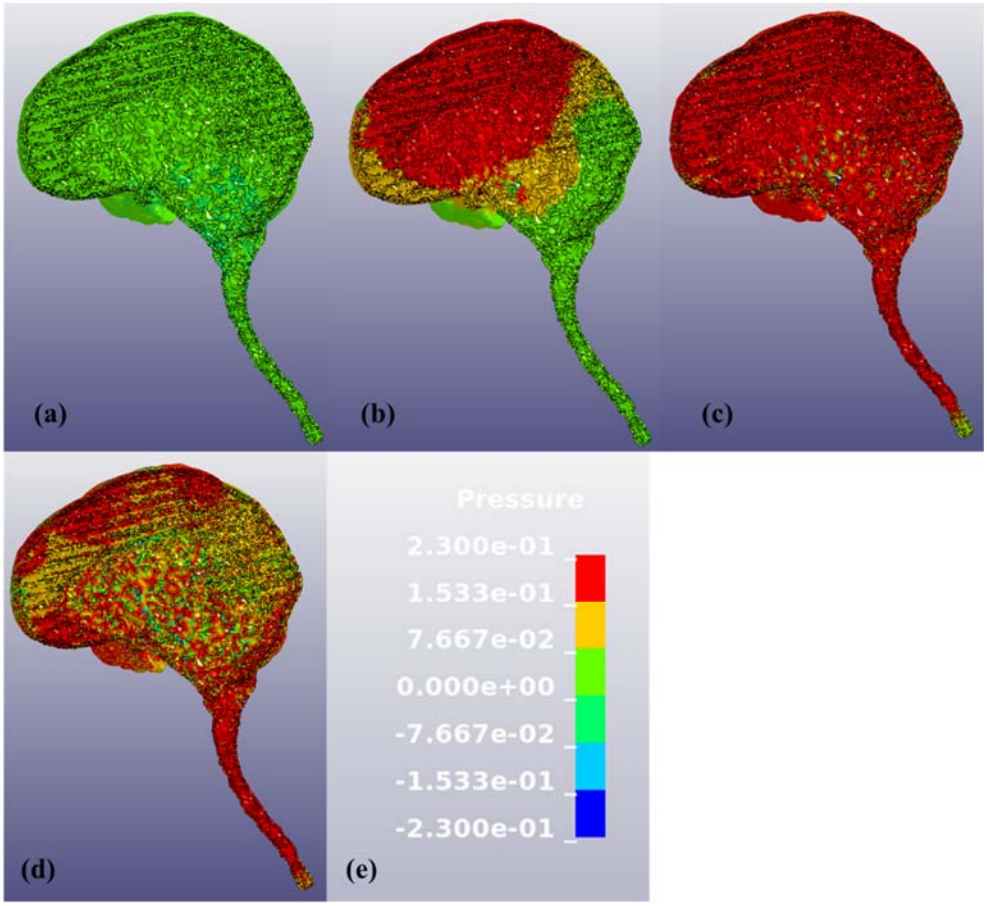

Figure 84. Brain sagittal cut snapshots of FEA pressure contours at (a) initial impact, (b) after first time step of initial impact, (c) at time step corresponding to peak pressure values, (d) at time step when models start recoiling, and (e) pressure contour scale (MPa)

4 DISCUSSIONS

An increase in sUAS velocity, resulting in an increased sUAS kinetic energy, leads to an increased percentage risk of brain injury upon the same orientation of impact. This is represented by the following charts which represent an overall correlation between an increase in sUAS velocity and, henceforth impact kinetic energy, and the overall amount of linear acceleration in g's, HIC value, and BrIC value sustained by the center of gravity of the brain for cases of the same orientation. Location of impact is another key factor in determining the severity of the impact, as well as the correlation to probability of risk of brain injury sustained. Examples of how velocity and orientation correlate with an increased rate of brain injury can be noted by the cases: the PMHS-Frontal-61fps-0°-Subject 1impact resulted in a 47% HIC-based AIS3 injury risk and a 18% risk for the BrIC-based AIS3 injury risk. For the PMHS-Frontal-71fps-0°-Subject 1 impact results in a 68% HIC-based AIS3 injury risk and a 32% for BrIC-based AIS3 injury risk. For another impact scenario for the same velocities and impact energies but different orientations; PMHS-Frontal-61fps-58°-Subject 1 impact resulted in a 38% HIC-based AIS3 injury risk and a 13% risk for the BrIC-based AIS3 injury risk. For the PMHS-Frontal-71fps-58°-Subject 2 impact results in a 79% HIC-based AIS3 injury risk and a 4% risk for the BrIC-based AIS3 injury risk. The following charts present a visual of the correlation between sUAS velocity and impact kinetic energy and angular acceleration, HIC, and BrIC.

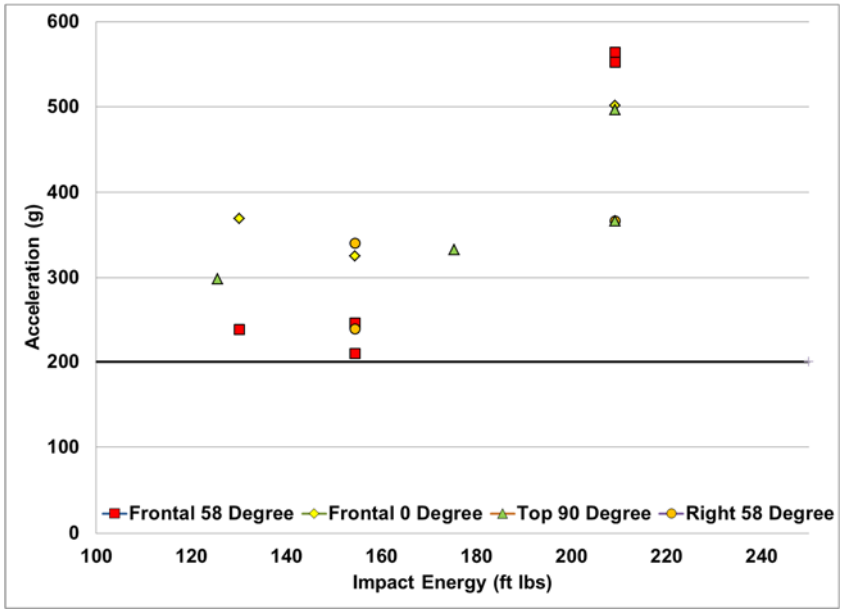

Figure 85. Acceleration vs. impact energy for simulated cases with 200 g threshold line

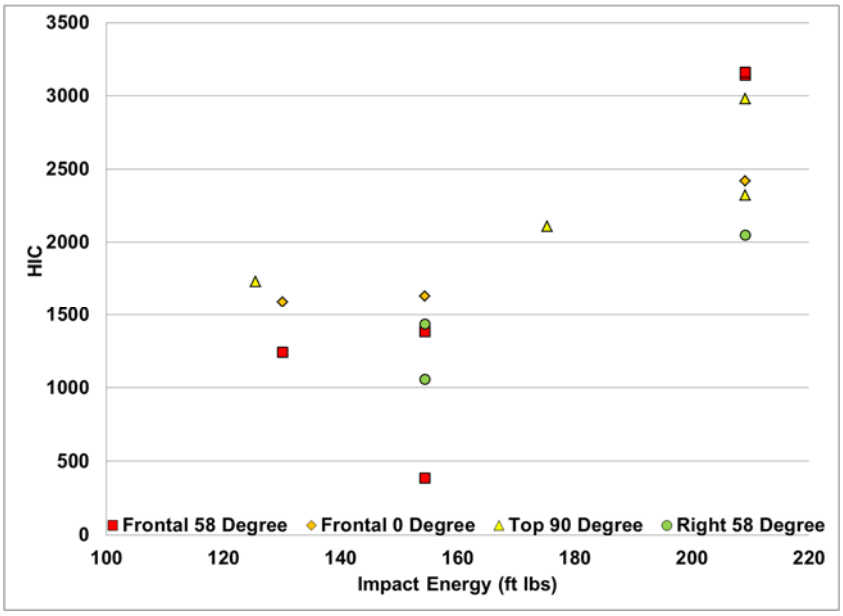

Figure 86. HIC vs. impact energy for simulated cases

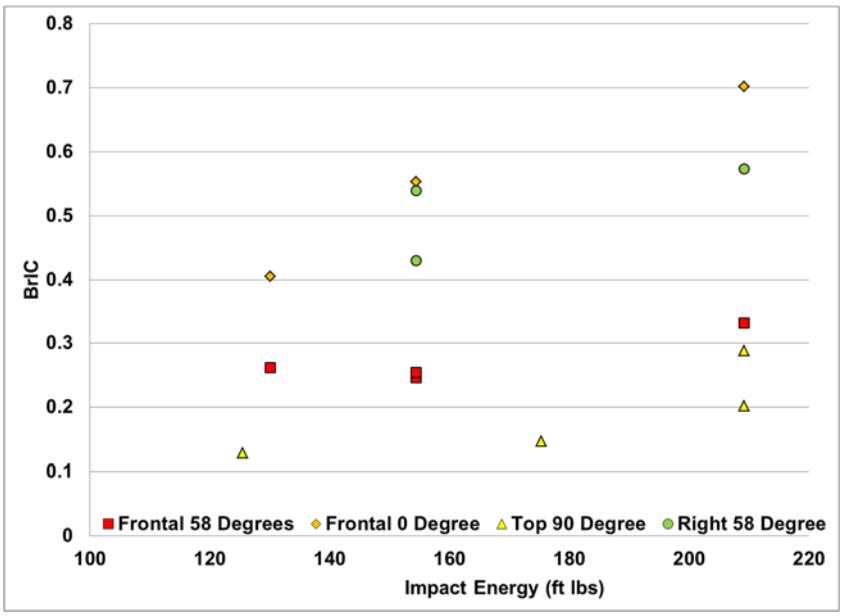

Figure 87. BrIC vs. impact energy for simulated cases

As seen from the presented data for most cases that do not result from a deviation from the worst case impact orientation; an increase in kinetic energy results in an overall higher risk of injury in terms of peak acceleration, HIC, and BrIC standards. Deviations from direct blunt force impact by the sUAS will be discussed in later conclusions. This overall trend can be utilized to better understand which drone will have the largest risk of causing the highest probability of injury risk of brain injury based on velocity and

kinetic energy, as well as the drones flying orientation as to which impact orientations they are most likely to conform to while performing tasks over human populations.

Based on the criteria (HIC and BrIC) used to quantify the amount of risk of injury that is to occur from the simulated impacts there are certain variations that must be addressed within the HIC and BrIC standards. The differing impact orientations have varying probability of injury risks predicted from the HIC value obtained, as well as differing probability of injury risk predicted from the correlated BrIC from the same impact. A high-injury risk predicted from HIC data does not always result in a high injury risk obtained from BrIC data, and in some cases an impact orientation will result in a very high risk of injury due to HIC indication, but produce very low percentage of risks for the BrIC derived injury risk. This can be predicted and explained from the criteria used to obtain each variable of HIC and BrIC, as HIC is solely linear acceleration based and BrIC is obtained from angular velocities that result from the impact. An example of a large variation from HIC to BrIC injury risks can be seen with the PMHS-Top-90° vertical impacts for all test subjects and all velocities. There were 4 impacts of this orientation, and the PMHS-Top-55fps-90°-Subject 2 impact resulted in an HIC injury risk of 50%, however the BrIC derived injury risk was only less than 2% for the same exact impact. The other 3 vertical top impacts included PMHS-Top-71fps-90°-Subject 2 with an HIC injury risk of 66% and a BrIC injury risk of 3%, PMHS-Top-65fps-90°-Subject 3 with an HIC injury risk of 66% and a BrIC injury risk of less than 2%, and PMHS-Top-71fps-90°-Subject 3 with an HIC injury risk of 77% and a BrIC injury risk of 2%. The below chart gives an overview of the simulated cases with their corresponding acceleration values, BrIC values, and HIC values; as well as the corresponding OSU values for the cases being modeled.

The injury risk curve for both HIC and BrIC derived injury criteria are shown below. The graphs correlate to a show the gradual variation in the increase through the lower end portion of the BrIC values which in turns increases drastically to result in a gradual plateau towards the higher end of both the BrIC and HIC AIS 3 or greater injury risk curves. The correlated data plotted against Risk of Injury vs. HIC and Risk of Injury vs. BrIC is shown below with both the simulated MSU impact data as well as the OSU sUAS impact experimentation data.

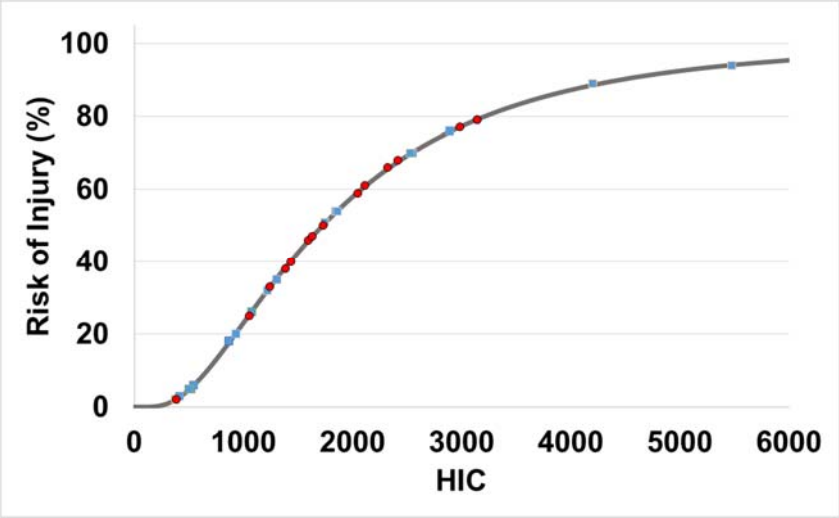

Figure 88. : AIS 3 or greater injury risk percentage vs. HIC values for simulation and experimental data

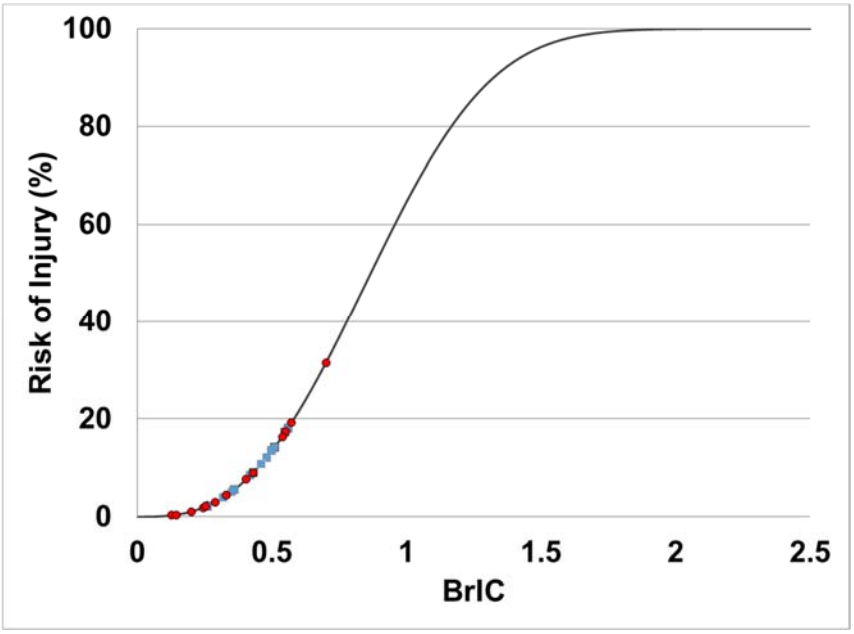

Figure 89. : AIS 3 or greater injury Risk percentage vs. BrIC values for simulation and experimental data

As seen from the data and graphs presented for both the MSU simulated cases as well as the OSU PMHS impacts tests the variation in the HIC and BrIC injury rates are certainly an aspect that must be addressed in terms of accepting the validity of both of these criteria but also looking to improve the quality of variable inclusion that can be taken into account to better quantify the likelihood and exact probability for damage to occur from these sUAS impacts.

The simulated sUAS impacts on the meshed PMHS model proved to be consistent with the PMHS experimental testing conducted by OSU in terms of peak acceleration, HIC, and BrIC values. The average difference between the peak acceleration values for the OSU experimental data and MSU simulated impacts was 14% and the overall form of the simulation acceleration graphs correlated well with the overall experimental data acceleration graphs. As seen in Figures 88 and 89 the human head and neck model correlated nicely with the percentage of injury risk predictions that were found from the OSU PMHS testing. Differences in the values obtained can be accredited to the human head and neck model simulating living tissue of a living human subject but utilizing the differences in geometry of a PMHS subject, therefore there will be slight differences in the overall material property mechanics of the human head and neck model and the PMHS subjects. These differences in mechanical properties can be extremely minute, however still produce slightly differing results in terms of the parameters that are generated while governing the impacts.

Minor differences in impacts orientation can result in drastic change in overall injury risk. If the sUAS angle shifts slightly upon impact with the PMHS or human head and neck model, the resultant acceleration and angular velocities produced can become drastically smaller in terms of overall peak. The intent of the study was to model the worst case orientation of the impacts, however the slight differing impacts that occurred during the experimental PMHS impacts provided an excellent foundation into the variation in injury risk that occurred when the impacts did not result in a center-of-gravity on center-of-gravity solid blunt force impact such as in the worst case orientations. These “off-center” impacts can be simulated with the human head and neck model to further understand the effects of differing orientation and offset impacts of the same velocity and impact kinetic energy. Figures 86 - 88 give a visual of the effects of the differing impact locations and how slight differences in these locations can initiate differences in peak acceleration, HIC, and BrIC that were obtained from the simulated impacts with the MSU human head and neck model.

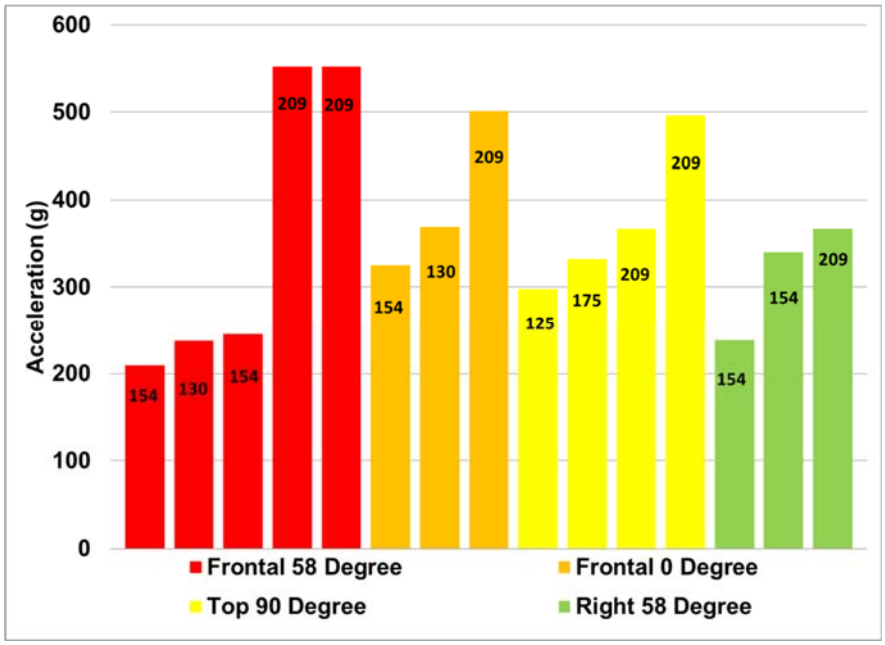

Figure 90. Peak acceleration histogram of each simulated case along with kinetic energy values (ft lbs) for different sUAS impact orientations and velocities

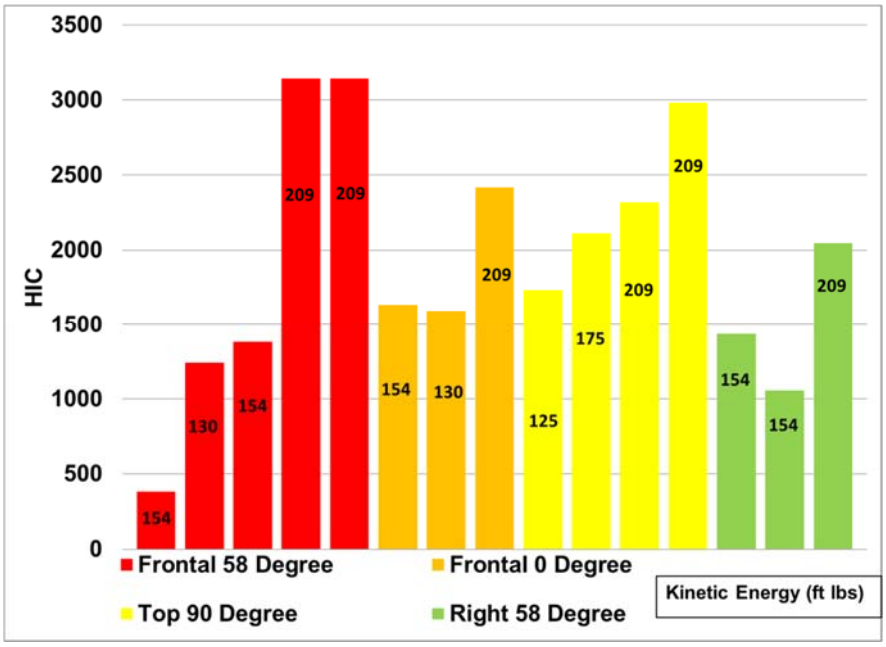

Figure 91. HIC value histogram for each simulated case along with the kinetic energy values (ft lbs) for different sUAS impact orientations and velocities

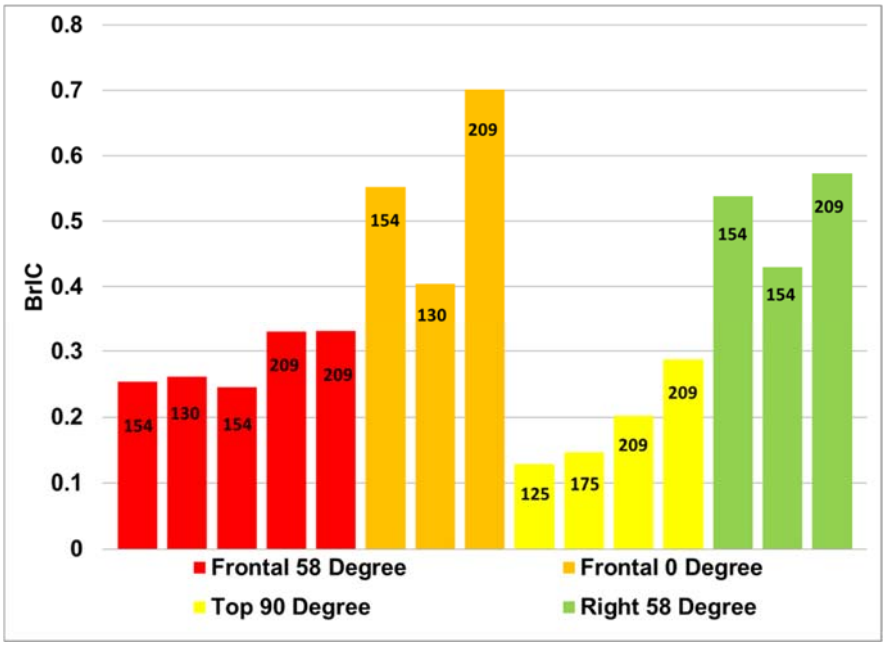

Figure 92. BrIC histogram for each simulated case along with the kinetic energy values (ft lbs) for different sUAS impact orientations and velocities

As seen in Figures 86 – 88, the various impacts of the same velocity, kinetic energy, and impact orientation can differ in the resultant peak accelerations, HIC values, and BrIC values obtained from the experiments and furthermore simulated impacts with the human head and neck model. An example of this is the PMHS-Frontal-61fps-58°-Subject 1, which resulted in a peak acceleration of 245.3 g's, a HIC value of 1384, and a BrIC value of .245, and PMHS-Frontal-61fps-58°-Subject 2, which resulted in a peak acceleration of 209.58 g's, a HIC value of 386, and a BrIC value of .2537. This drop in peak acceleration can be accredited to sUAS impacting off-center and sliding down the face of the PMHS subject and the human head and neck model rather than connecting with a solid and full on blunt force impact.

As seen from the pressure contour plots for each simulated case (Figures 14, 19, 24, 29, 34, 39, 44, 49, 54, 59, 64, 69, 74, 79 and 84), the overall pressure conjugation for each of the cases exceeds 230 KPa. This gives a certain percentage risk of brain injury and concussion from every single impact case simulated. The threshold being exceeded in all of the cases is not unpredicted. Considering the high velocities of the sUAS impacts, as well as the impacts being in the worst orientation fashion, the injury risk, potentially leading to severe concussion, is predicted. However, the AIS 3 brain injury risk curves, usingHIC and BrIC, vary in the prediction of concussion from case to case. Hence, further work is needed to determine the correct injury risk assessment methodologies for sUAS human head impacts that are consistent in predicting brain injury risk across varying sUAS velocities, impact locations and offset.

5 CONCLUSIONS AND RECOMMENDATIONS

5.1 Conclusion 1

As the kinetic energy of the sUAS increases the percentage risk of brain injury also increase. For the same sUAS, the kinetic energy of the sUAS is proportional to the square of the impact velocity. Hence, the peak

acceleration, HIC and BrIC (Figures 81 -83) also have increasing trend with increasing impact velocity. Most brain injuries, in the current study, were AIS 3+.

5.2 Recommendation 1

Future work would benefit from a robust design of experiments, along with uncertainty quantification, to evaluate injury metrics over the entire domain (range) of the input parameters (sUAS type, impact location, and impact angle). This would help develop mathematical surrogate models for the brain injury metrics. This could then be further used to better parameterize the injury risk from each individual impact orientation and orientations as a whole.

5.3 Conclusion 2

The AIS 3 percentage risk of brain injuries evaluated from HIC and BrIC. HIC is based linear acceleration, and BrIC is based on angular velocities of the head's CG. Hence, the worst case scenarios for brain injuries were different when assessed using HIC or BIC. Overall, the above mentioned brain injury metrics are conservative, and as such, due to the inconsistencies in evaluating brain injuries using HIC or BrIC, further investigation into brain injury metrics is warranted.

5.4 Recommendation 2

Future work would benefit from the development of brain injury metrics relevant to the characteristics of sUAS impacts on the human head, for the HIC and BrIC methods utilized, even though adequate in their own respect, seem to have contradictions within one another as to which will cause a risk of brain injury and which will not cause said risk.

5.5 Conclusion 3

MSU's FE simulations of the OSU PMHS tests produced FE simulation results that were comparable to experimental data. The average difference in peak accelerations for all simulated and experimental cases were 14%. The current modeling methodology for high biofidelic human head and neck model is suitable to capture the biomechanics of PMHS test head and neck injuries.

5.6 Recommendation 3

Future work would benefit from the use of PHMS specific human head and neck FE models so that FE results can be compared with PHMS experimental results without the need for data normalization by head mass or geometry. MSU's high-fidelity human head FE models can be in conjunction with NIAR's THUMS FE model to quantify AIS-based brain injury risks.

5.7 Conclusion 4

For certain PMHS tests and simulations, a small variation in the impact scenario produced significant changes in peak accelerations, HIC, and BrIC. Further, these variations are inconsistent, suggesting that they may additional variables that need to be taken into account.

5.8 Recommendation 4

Future work, along with mathematical surrogate modeling, on the sensitivity analysis of the all input variables would be essential to understanding the local and global sensitivities input parameters. Additionally, the sensitivity analysis would give the uncertainties of each input variable.

5.9 Conclusion 5

The risk of brain injury, as observed using pressure in the brain as a metric, indicates that most simulated impact cases show high level of risk for concussion. Here, the peak pressure values in the brain were observed to be greater than 230 KPa, which is the threshold for severe concussion.